ANALYSIS OF RANDOM MATRIX THEORY MODEL FOR
DOMINANT MODE REJECTION BEAMFORMER NOTCH DEPTH IN PHILSEA10

by

Sai Kasyap Kamaraju
A Thesis
Submitted to the
Graduate Faculty
of
George Mason University
In Partial fulfillment of
The Requirements for the Degree
of
Master of Science
Electrical Engineering

Committee:

_____	Dr. Kathleen E. Wage, Thesis Director
_____	Dr. Lloyd J.Griffiths, Committee Member
_____	Dr. Yariv Ephriam, Committee Member
_____	Dr. Monson Hayes, Chairman, Department of Electrical and Computer Engineering
_____	Dr. Kenneth S.Ball, Dean for Volgenau School of Engineering

Date: _____ Fall 2016
George Mason University
Fairfax, VA

Analysis of RMT Model for Dominant Mode Rejection Beamformer notch depth in PhilSea10

A thesis submitted in partial fulfillment of the requirements for the degree of
Master of Science at George Mason University

By

Sai Kasyap Kamaraju
Bachelor of Technology
Jawaharlal Nehru Technological University, 2013

Director: Dr. Kathleen E. Wage, Professor
Department of Electrical and Computer Engineering

Fall 2016
George Mason University
Fairfax, VA

Dedication

I dedicate this thesis to my loving parents Ratna Kumari and Rama Rao.

Acknowledgments

It gives me immense pleasure to express my heart-felt gratitude to all those who have been there all the while during my research period, lending their help in every possible way to come out of the course with flying colors.

With all sincerity and high regards, I express my deep sense of gratitude to my research supervisor, Professor Kathleen E. Wage for giving me an opportunity to work on this thesis and introducing me to the world of research with her meticulous guidance and valuable suggestions throughout this investigation.

I consider myself fortunate to work under the guidance of Dr. Kathleen E. Wage who taught me the ABCs of signal processing, array signal processing and helped me to come out from my mistakes while executing the thesis work and also given me the much needed boost and showed a very good direction to my career. Her teaching has broadened my knowledge in the area of array signal processing and has given me more confidence to explore new frontiers. I will ever remain grateful to her for her inspiring guidance and wise counsel. This thesis would not have seen the light of the day without her support and care.

I would also like to thank the members of my committee, Dr. Yariv Ephriam and Dr. Lloyd J.Griffiths for their time, insight and support.

A thank you goes to my fellow lab mates Mehdi farrokhrooz and Vaibhav chavali for their help in technicalities, feedback and valuable suggestions on my thesis.

Finally, I would like to thank my parents for their constant backing, love and support.

Abstract

ANALYSIS OF RMT MODEL FOR DOMINANT MODE REJECTION BEAMFORMER NOTCH DEPTH IN PHILSEA10

Sai Kasyap Kamaraju

George Mason University, 2016

Thesis Director: Dr. Kathleen E. Wage

In sonar array signal processing, one of the essential objectives is mitigating the effect of loud non-stationary interfering sources. The Dominant Mode Rejection adaptive beamformer is a beamformer that is often used to detect low powered signals in the presence of high power interferers. The DMR beamformer constructs its weights using a structured covariance estimate which is obtained by doing the principal component analysis of the sample covariance matrix (SCM). Notch depth is a parameter which quantifies how well a beamformer can attenuate an interferer. In prior work, Buck and Wage developed an analytical model that predicts average DMR notch depth as a function of interferer strength and the number of snapshots available to estimate the eigendecomposition of the SCM [IEEE Stat. Sig. Proc. Workshop, 2012]. The DMR notch depth model is based on results from random matrix theory on the accuracy of the eigenvectors of the SCM. This thesis assesses the validity of the notch depth model using data recorded with a vertical line array during the 2010 Philippine Sea Experiment. In the PhilSea10 analysis the DMR beamformer removes loud mechanical vibration noise (array strum) from the data set. Results show good agreement with theory when the experimental data satisfies the assumptions of the model.

Table of Contents

Chapter 1: Introduction

In passive sonar array processing, the primary goal is to alleviate the impact of non-stationary loud interfering sources. Conventional beamformer, the simplest spatial filter which is non adaptive in nature often permits loud sources to leak through the side lobes of its beampattern, also conceals the signal of interest. To succeed in this task, development was made initially by using Minimum Variance Distortionless(MVDR) beamformer also known as Capon beamformer[1], which can be regarded as the most basic adaptive beamformer. The MVDR beamformer is derived by minimizing output power subject to a unity gain constraint in the look direction, by assuming known signal characteristics.

In real world scenario, more often ensemble statistics (ECM) are not available, and beamformers must be implemented using sample statistics (SCM). As an estimate of the ensemble covariance, the SCM usually has some error with respect to the ensemble covariance matrix, and this error or mismatch can bring about considerable degradation in the performance of adaptive beamformers [2]. Performance depends on the number of data snapshots used to estimate the sample covariance matrix (SCM). Generally, larger the number of snapshots closer is the SCM to the ECM. One such algorithm proposed to address this issue is the DMR beamformer.

Dominant Mode Rejection beamformer (DMR) is a type of adaptive eigenvector beamformer derived by Abraham and Owsley [3] constructs its weights using a structured covariance estimate which is obtained by doing the principal component analysis of the sample covariance matrix. Eigendecomposition is used to separate the components in to the doaminant and noise subspaces.The dominant subspace is denoted by the eigenvectors associated with the largest eigenvalues of the sample covariance matrix while the all the eigenvalues for the noise subspace in the SCM are replaced by their mean value. The number of eigenvalues which are dominant, determines the subspace rank and also the number of plane wave interferers that approaches the array. When the background noise is spatially white, the rank of the Noise subspace is known, ensemble statistics are accessible, then DMR beamformer becomes equal to the optimum minimum variance distortionless response (MVDR) beamformer.

1.1 Prior work on DMR performance estimation

In prior work, Buck and Wage developed an analytical model that predicts average DMR notch depth as a function of interferer strength and the number of snapshots available to estimate the eigendecomposition of the SCM [4]. A single interferer model for a DMR beamformer is thoroughly analyzed as a function of number of snapshots [5]. For the estimation of covariance matrix from its data, it is worth to cite a recent work by Wage and Buck [5] wherein the determination of DMR performance tells how closely the eigenvectors of the sample covariance matches with the true interferer directions. This thesis is focused on understanding the performance of DMR algorithm supported by numerical results based

on a characteristic term called Notch Depth (ND). ND quantifies how well a beamformer can eliminate an interferer. A deeper notch implies that the beamformer filters out a lot of the interference, thus enhancing its output signal-to-interference-plus-noise (SINR) ratio.

In a Recent work for the application of Random Matrix theory, an analytical model was built to predict the DMR notch depth using RMT as a function of array size, number of snapshots, interferer location, and interference-to-noise ratio (INR) [4]. Random matrix theory (RMT) provides results on the convergence of the SCM to the ECM. In particular, the problem of estimating the SCM for robust sources in presence of background noise is one of the examples of the spiked covariance model in RMT. These spiked covariance models are used to analyze the behavior of SCMs for the case where a relatively low rank perturbation is additional to a Wishart matrix. RMT differs basically from the classic strategies that are used to analyze the asymptotic performance of adaptive beamformer(ABF). In classical approach, ABF results assumes that the array size is fixed, but the number of snapshots $L \to \infty$. Contrastingly to the RMT approach, ABF results assumes that both $N, L \to \infty$, but that they converge to a constant ratio c = N/L as they grow. This model of asymptotic analysis is congruent with ABF studies that have found performance well parameterized by the ratio of snapshots to sensors, or snapshots to interferers. Additionally, the asymptotic limiting expressions obtained in RMT have demonstrated to predict precisely the performance of even modest size arrays.

The model predictions have been verified using numerical simulations initially [4]. The other nearest related result is Richmonds analysis of MVDR beampatterns [6]. The experimental validation of DMR notch depth using RMT model of DMR beamformer notch depth was established by Wage and others[7] in discrete set of receptions where each reception was 155 seconds long. In addition, Wage and Buck [8] derived a theoretical equation of the SINR loss for the DMR ABF using the Random Matrix Theory (RMT). SINR loss governs the rate of convergence of DMR to the optimal MVDR beamformer.

In this thesis, the strum in 2010 Philippines Sea Experiment is used as test signal to validate the random matrix theory model for DMR beamformer notch depth.

1.2 Prior work on experimental validation of RMT notch depth predictions

Hydrophones that are hung at one end of a cable are likely to suffer a peculiar noise called Strum ,this form of self noise occurs in current of water, which is the result of cable vibration induced by the eddies or vortices shed by cable [9]. Cable strum in passive sonar arrays has always been a restricting factor for ocean acoustic source detection at low frequency.

Generally, cable fairing is used to reduce the strum by designing the structure streamline the flow around the cable. The cable fairing cannot eliminate strum fully but can reduce by distorting the strum signal.

In early 2000's, MVDR Beamspace adaptive beamforming was used to eliminate Hydrodynamic Towed Array Self-noise by Vincent and others [10]. This paper deals with elimination of flow noise using white noise gain constraint(WNGC) which is done by implementing a suitable balance between aggressive adaption for effective strum nulling and

conservative adaptation for robustness to mismatch-induced self-nulling.The WNGC implementation based on the scaled projection technique was first presented by Cox [11] in which cable strum was significantly reduced.

This was improved later by changing the Array Shape (AEL compensation) with sub-array beam-space ABF [12]. Recently , Experimental validation of RMT model on DMR notch depth in PhilSea10 (discrete set of receptions) was implemented by Wage and others [7] which was indeed used to eliminate the strum.

In Philippines Sea Experiment 2010, the fairing of the cable was not used, hence it could be used for analysis of strum over the time and eliminating it using DMR beamforming technique.

1.3 Goal

The goal of this thesis is to explore the validity of the DMR notch depth predictions using experimental data. This analysis uses continuous data from a vertical sub array deployed as a part of the 2010 Philippine Sea (PhilSea10) experiment. At low frequencies the PhilSea receptions include an interference signal attributed to mechanical vibration of the array cable. Analysis of the cable strum signal indicates that it lies within a subspace spanned by the first three eigenvectors of the covariance matrix. This is the type of low-rank interference that the DMR beamformer is designed to remove. Since the strum was not consistent in the continuous set of receptions, the strum which was constant is picked for the analysis. As the data was continuous i.e., as long as 55 Hr, this give a luxury to choose the number of snapshots of our choice unlike in the previous research where the snapshots were constraint to 310 as the reception length was 155 sec. The other notable difference is that the number of receptions were significantly more in the previous research but in this thesis, there is deficient or low number of receptions to deal with. This thesis outlays the conditions for meeting the RMT predictions for the validation of DMR notch depth and vice versa. Prior to the experimental validation, simulations were examined to test the multiple interferer environments as the RMT based analytical model was developed for a single interferer case. The objective of these simulations is to study the various parameters like interferer location, number of interferers, INR, Monte carlo trials etc., that effect the validation of DMR notch depth. Moreover, the rank estimation techniques like RMT, AIC, MDL and eigenvector based rank estimation by picking the maximum values of wave number have also been examined in the PhilSea10.

1.4 Organization

The remainder of the thesis is organized as follows. Chapter 2 presents background on narrowband beamforming, defines the DMR beamformer, and reviews previous work using RMT to characterize DMR performance. Simulation and analysis of the performance of the DMR beamformer Notch depth along with its validation model is described in Chapter 3. Chapter 4 describes the 2010 Philippines Sea Experiment, eigenvalues and eigenvectors of the strum, Rank estimation methods and selection of constant strum. Chapter 5 gives insight of experimental results for validation of DMR notch depth using RMT for discrete

and continuous receptions in PhilSea10. Chapter 6 concludes the thesis and discusses future work.

Chapter 2: Technical Background

This chapter provides the technical background for the thesis and reviews previous work on DMR performance analysis. Section 2.1 defines the narrowband planewave beamforming model used throughout the thesis and Section 2.2 reviews the definition of notch depth as a performance metric. Section 2.3 describes the DMR beamforming algorithm. Finally, Section 2.4 reviews key random matrix theory results that have been applied to analyze DMR.

2.1 Narrowband planewave beamforming model

Beamforming is way to deal with spatial signal processing of the signals in the space time field by exploiting their spatial attributes by a array of sensors[13].

Planewave beamforming assumes that the arriving signals are planewaves and number of planewaves are given by D. For a narrowband beamformer, the signal received 'p' by an array of N sensors can be written as a column vector

$$\mathbf{p(l)} = \sum_{i=1}^{D} \mathbf{b_i}(l)\mathbf{v_i} + \mathbf{n}. \tag{2.1}$$

b_i is the amplitude of the i^{th} signal, $\mathbf{v}_i$ is the planewave replica vector for the i^{th} signal, and $\mathbf{n}$ is a vector of complex noise samples. For N-sensor linear array oriented along the z-axis, the replica for the i^{th} signal is a complex exponential vector

$$\mathbf{v}_i = \mathbf{v}(\theta_i) = \begin{pmatrix} e^{j\frac{2\pi}{\lambda}cos(\theta_i)z_i} \\ \vdots \\ e^{j\frac{2\pi}{\lambda}cos(\theta_i)z_N} \end{pmatrix} \tag{2.2}$$

Where
$\mathbf{v_i}$ - replica vector of the plane wave for i^{th} source,
$\mathbf{b_i}$ - amplitude of the i^{th} source (zero mean proper complex magnitude).
$\mathbf{n}$ - spatially white noise at input,
λ - wavelength,
with $d = \lambda/2$ spacing between the array elements,
$\theta_\mathbf{i}$ - interferer angle measured from the positive z-axis at position i.
$\mathbf{z_n}$ is the location of the nth sensor.

Note that the replica vector is normalized such that $\mathbf{v}_i^{\mathrm{H}}\mathbf{v}_i = N$. This model assumes the signal amplitude $\mathbf{b_i}$ as a zero-mean complex circular random variable and that the complex circular random noise is zero mean and spatially white(Details are provided in the third chapter which deals with simulations).

The number of planewave interfering signals determine the rank of DMR beamformer. For example, consider a single plane wave signal, then with $\mathbf{v}_1$ replica vector, the whole matrix p can be found out. This makes rank of SCM and ECM formed by single interferer plane wave signal to be 1.

A general planewave beamforming system for an array of N sensors is shown below :

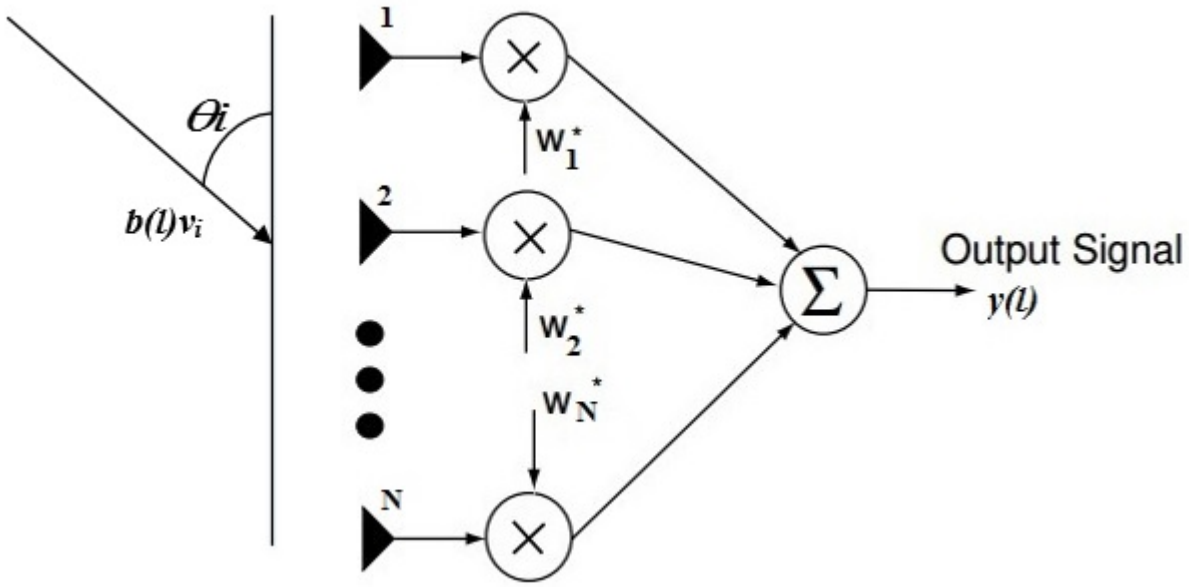

Figure 2.1: A general planewave beamforming system

The objective of beamforming to find out a methodology for received vector $\mathbf{p}$ such that a planewave signal from a desired direction m passes through undistorted while signals from other angles are attenuated.

The output of a linear beamformer is $\mathbf{W}^{\mathrm{H}}\mathbf{p}$, where $\mathbf{w}$ is the weight vector associated with the steering angle θ_m.

For ensemble case, we tend to assume all the statistics are fully known (practically not possible), assumptive that the planewave signals are independent, the Model and ECM for the received signal are (ignoring snapshots for ensemble case)

$$\mathbf{p} = \sum_{i=1}^{D} b_i \mathbf{v}_i + \mathbf{n} \tag{2.3}$$

$$\Sigma = \mathcal{E}\{\mathbf{p}\mathbf{p}^{\mathrm{H}}\} = \sum_{i=1}^{D} \sigma_i^2 \mathbf{v}_i \mathbf{v}_i^{\mathrm{H}} + \sigma_w^2 \mathbf{I}. \tag{2.4}$$

The power in the i^{th} source is σ_i^2, and the white noise power is σ_w^2.

One of the simplest non parametric method used is commonly referred to as conventional beamformer.

In conventional beamforming these weights are pre-defined and data independent. The weights can be uniform or outlined by a window function (rectwin). Although the conventional beamformer is somewhat constrained in its angular resolution, its vital advantages are implementation simplicity and robustness. The conventional beamformer is the spatial matched filter for the replica vector associated with the steering direction, i.e., the CBF weight vector is

$$\mathbf{w}_{\mathrm{CBF}} = \frac{1}{N}\mathbf{v}_m = \frac{1}{N}\mathbf{v}(\theta_m) \tag{2.5}$$

The 1/N normalization guarantees that the CBF has unity gain in the look direction.

2.2 Notch depth as performance metric

This section, highlights the ND as a standard metric that determine beamformer performance. Each of the metrics outlined below relies on the weight vector w, which indeed depends on the steering angle θ_m. To keep the things easy, the dependence on θ_m is not explicitly mentioned.

In addition to the adaptive weight vectors, the following metrics are also data dependent, therefore these can be modeled as random variables and quantified by their statistics (mean, variance, etc.) for simulations (shown in chapter 3).

The beampattern which can be considered as a frequency response of a spatial filter, is defined in terms of the angleθ or, equivalently, in terms of its cosine $u = \cos(\theta)$ given by

$$B(\theta) \triangleq \mathbf{w}^{\mathbf{H}}\mathbf{v}(\theta) = \mathbf{w}^{\mathrm{H}}\mathbf{v}(u). \tag{2.6}$$

It describes the beamformer's response to a unity amplitude planewave from angle θ.
Below figure 2.2 is a beampattern for a single interferer example at interferers location $u_i = 0.0252$.

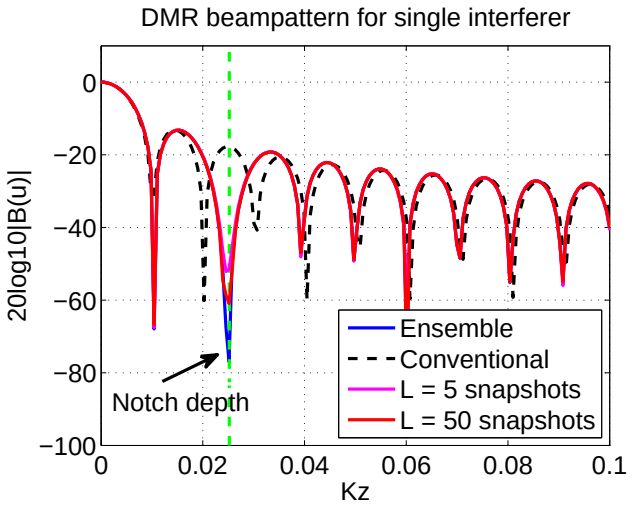

Figure 2.2: DMR beampattern for a single interferer with INR = 30 dB at location at 0.0252

As it is observed in the Figure 2.2, the loud interferer of INR 30 dB has been attenuated compared to the look direction. Notch depth here approximately is -78 dB for an ensemble case. Notch depth defines the proportion by which beamformer can eliminate the interferer.

The notch depth (ND) is defined as the absolute value squared of the beampattern in the direction of an interfering signal, e.g., for the i$^{\text{th}}$ interferer

$$ND \triangleq |B(\theta_i)|^2 = |\mathbf{w}^{\mathrm{H}}\mathbf{v}_i|^2 \tag{2.7}$$

ND depends on interference direction θ_i.

2.3 Dominant Mode Rejection Beamformer

The dominant mode rejection beamformer was initially presented by Abraham and Owsley in 1990 [3]. In figure 2.2, it can be observed that the CBF cannot eliminate the interferer unless it is situated at null, where as the DMR beamformer sucessfully eliminates the interferer even at peak side lobe. This proves the adaptive nature of dominant mode rejection beamformer. The DMR ABF beamformer starts with a general model for $\mathbf{p}$ that includes discrete planewave signals, colored noise, and spatially white noise with power σ_w^2 .

They assume that there are D strong planewave signals (interferers) that need to be attenuated to facilitate detection of a weaker desired planewave signal. With this assumption, they can partition the covariance matrix into a dominant interferer subspace and a noise subspace; the latter includes the weaker signals and the noise. DMR assumes that the large eigenvalues of Σ are all associated with interferers to be rejected and that the small eigenvalues are due to weak signals and noise. Sorting the eigenvalues in descending order

leads to the following expression for the eigendecomposition of the ECM:

$$\Sigma = \Xi\Gamma\Xi^{\mathrm{H}} = \underbrace{\sum_{n=1}^{D} \gamma_n \xi_n \xi_n^{\mathrm{H}}}_{\text{large eigenvalues}} + \underbrace{\sum_{n=D+1}^{N} \gamma_n \xi_n \xi_n^{\mathrm{H}}}_{\text{smalleigenvalues}} \tag{2.8}$$

The dominant mode rejection beamformer calculates its adaptive weights based on reduced rank structured covariance estimate, which is formed by eigen decomposition of ensemble covariance matrix (ECM). The DMR weight vector is the MVDR weight vector [1], with the ECM replaced by Σ_{DMR}

$$\mathbf{w}_{\mathrm{DMR}} = \left(\mathbf{v}_m^{\mathrm{H}} \Sigma_{\mathrm{DMR}}^{-1} \mathbf{v}_m\right)^{-1} \Sigma_{\mathrm{DMR}}^{-1} \mathbf{v}_m \tag{2.9}$$

where v_m is the replica associated with the steering angle θ_m.

When the ensemble covariance matrix (ECM) is not available, it can be supplanted by sample covariance matrix (SCM) which is computed from the number of accessible snapshots.

For infinite set of snapshots SCM converges to ECM. Higher the snapshots to average,implies that SCM converges closer to ECM. The rank here represents the number of interferers (D), drawing nearer the array.

For an experimental data, the rank is unknown. Hence rank estimation is to be done as the oceanographic data changes with both frequency and time. Various rank estimation techniques are described in chapter 4.
In this beamformer, large eigenvalues are assumed as interferers and small eigenvalues are averaged.

The SCM and its eigendecomposition are defined as

$$\mathbf{S} = \frac{1}{L} \sum_{l=1}^{L} \mathbf{p}_l \mathbf{p}_l^{\mathrm{H}} = \sum_{n=1}^{N} g_n \mathbf{e}_n \mathbf{e}_n^{\mathrm{H}} = \mathbf{E}\mathbf{G}\mathbf{E}^{\mathrm{H}} \tag{2.10}$$

where $\mathbf{p_l}$ is the l^{th} data snapshot, $e_n$and and g_n are the sample eigenvectors and eigenvalues, respectively. Using the SCM, the sample DMR covariance matrix is

$$\mathbf{S}_{\mathrm{DMR}} = \sum_{n=1}^{D} g_n \mathbf{e}_n \mathbf{e}_n^{\mathrm{H}} + \sum_{n=D+1}^{N} s_w^2 \mathbf{e}_n \mathbf{e}_n^{\mathrm{H}} \tag{2.11}$$

Where s_w^2 is the estimated noise power;

$$s_w^2 = \left(\frac{L}{L-1}\right)\left(\frac{1}{N-D}\right) \sum_{n=D+1}^{N} g_n \tag{2.12}$$

The structured covariance matrix which DMR uses is processed utilizing the SCM based on L number of snapshots.The DMR characteristics vary as the number of snapshots varies. The number of snapshots in turn vary the SCM, which in turn varies the eigenvectors and eigenvalues. For the point of Sample covariance matrix computation, a recent work by Wage and Buck [5] showed that the performance of DMR is principally dictated by how closely the eigenvectors of the sample covariance matrix coordinate with the interferer locations.

The $L/(L1)$ factor in (2.11) compensates for the inherent bias in sample variance calculations. This factor is negligible when L is large, but must be included to obtain unbiased results for snapshot-deficient cases. The advantage of using the estimated noise power when computing S_{DMR} is that it eliminates the small eigenvalues, which cause problems with inverting the SCM to compute the MVDR weight vector. Substituting S_{DMR} for Σ_{DMR} in (12) and using the matrix inversion lemma, the DMR weight vector can be written

$$\mathbf{w}_{\mathrm{DMR}} = \frac{\mathbf{v}_m - \sum_{i=1}^{D} \left(\frac{g_i - s_w^2}{g_i} \right) \mathbf{e}_i \mathbf{e}_i^{\mathrm{H}} \mathbf{v}_m}{\mathbf{v}_m^{\mathrm{H}} \mathbf{v}_m \left(1 - \sum_{i=1}^{D} \left(\frac{g_i - s_w^2}{g_i} \right) \cos^2(\mathbf{e}_i, \mathbf{v}_m) \right)} \tag{2.13}$$

$\cos^2(\mathbf{e}_i, \mathbf{v}_m)$ is the generalized cosine between vectors e_i and v_m, as defined in [11].

In Figure 2.2, It can be observed that the ND value of ensemble case was $-75dB$ approximately, while for snapshots L 4= 50 and 500 it was -51 and $-62dB$ respectively. So as we keep increasing the snapshot number at some value the ensemble notch depth and the sample mean notch depth would be almost equal. Hence at higher snapshots the notch depth is more deeper and also it is possible to determine the ensemble characteristics of DMR beamformer. The modified DMR algorithms exclude an eigenvector from the dominant subspace when its associated interferer moves too close to the desired look direction. Attenuating a loud signal that is inside the main lobe (ML) of the beamformer while maintaining the unity gain constraint is quite difficult. This problem is not unique to DMR; the performance of most ABFs degrades substantially in the presence of ML interference if the proper adjustments are not made.

2.4 Random Matrix Theory

Since the beginning of the 20th century, Random matrix theory (RMT) has been finding applications in various domains such as number theory, quantum mechanics, condensed matter physics, wireless communications, signal processing etc. One such application is being implemented in this thesis, is the validation of DMR beamformer notch depth using RMT as reported by Wage and Buck [4]. Recent study on RMT contains valuable insights about the behavior of the eigenvalues and eigenvectors of large random matrices. The RMT analysis of the spiked covariance case is asymptotic [14]: N,$L \to \infty$and the ratio NŁ $\to c$. Unlike traditional asymptotic analyses of ABFs (N fixed, $L \to \infty$), RMT provides useful predictions for snapshot-deficient cases ($c > 1$). The key result related to DMR is a prediction of the limiting value of the generalized cosine between the ensemble eigenvector and sample eigenvector.

RMT gives valuable forecasts for snapshot-deficient cases. Wage and Buck [5] identified a key result by relating the RMT analysis of spiked covariance model with DMR, an expectation of the limiting value of the generalized cosine between the ensemble eigenvector and the sample eigenvector.

$$cos^2(\mathbf{e_i}, \mathbf{v_i}) = \begin{cases} 0 & \text{if } N\frac{\sigma_i^2}{\sigma_w^2} \leq \sqrt{c} \\ \frac{1-c(\frac{\sigma_i^2}{N\sigma_w^2})^2}{1+c\frac{\sigma_i^2}{N\sigma_w^2}} & \text{if } N\frac{\sigma_i^2}{\sigma_w^2} \leq \sqrt{c} \end{cases} \tag{2.14}$$

This equation gives us an idea of phase transition phenomenon.

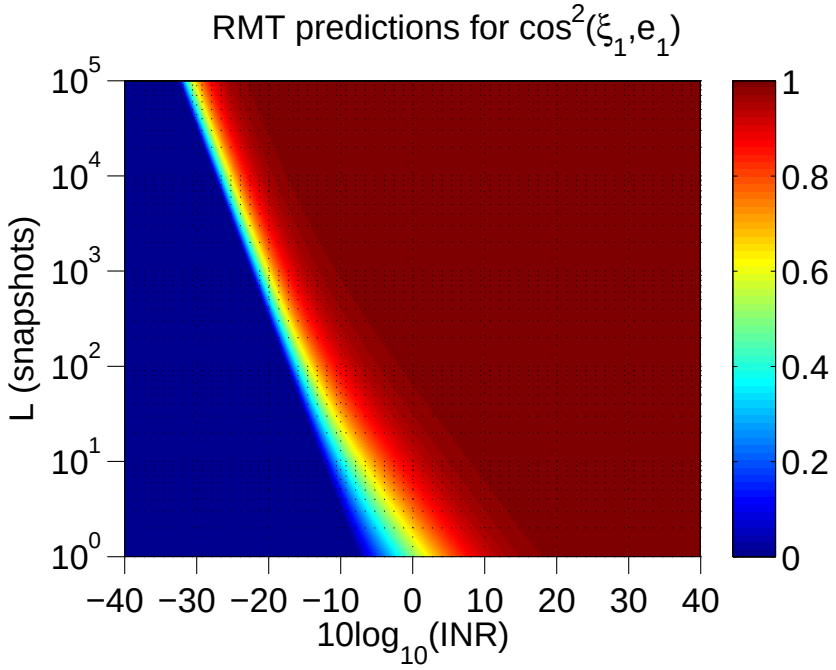

Figure 2.3: RMT predictions of the generalized cosine squared between the ensemble eigenvector and the sample eigenvector as a function of INR and snapshots. Results are shown for a 31-sensor array.

When INR is below the threshold, e_i is orthogonal to ξ_i. When INR is above this threshold, e_i is a biased estimate of ξ_i. The threshold is the square root of the ratio of sensors to snapshots. Fig. 2.3 shows how the prediction varies with INR and for a 31-sensor array.

The phase transition behavior of the sample eigenvectors explains several important aspects of DMR performance. First, it explains why DMR ND is equal to the CBF ND for low INR. For interferers below the threshold, the sample eigenvector is orthogonal to the true eigenvector, meaning that the beamformer knows nothing about the location of the interferer. For a 31-sensor array operating with a single snapshot, the threshold is exceeded by interferers with INRs of 8.5 dB and higher. As the array accumulates more snapshots, the threshold decreases, meaning that the array can look interferers with even lower INRs.

Fig. 2.3 illustrates the change in threshold as a function of snapshots.

Second, the phase transition described in [7] explains why the DMR ABF fails to achieve the ensemble ND in many cases. When the interferer exceeds the threshold, the sample eigenvectors are biased since for any value of c.

The bias disappears as c tends to 0, and the rate at which it disappears depends on the INR. ND decreases as L increases. Since the array size is fixed, an increase in L implies a decrease in C. Fig. 2.3 also shows that the number of snapshots required to achieve ensemble performance as a function of INR.
The relationship between sample eigenvector and true eigenvectors is established by a simple fluctuation model which was suggest by Paul, [15] where sample eigenvector is defined as weighted sum of the true eigenvectors [8].

2.4.1 RMT model prediction for ND vs L

Derivation of the model for ND (described in eqn 2.6) vs. L is as follows. Firstly, the replica vector steered towards look direction vm (considering broadside throughout the thesis) and replica vector vi for the interferer direction are projected on the directions containing the unit vectors,i.e ensemble interferer eigenvector ξ_1 and an orthogonal residual $\xi_\perp$ as

$$\mathbf{v}_m = \sqrt{N}\cos(\mathbf{v}_m, \mathbf{v}_1)\xi_1 + \sqrt{N}\sin(\mathbf{v}_m, \mathbf{v}_1)\xi_\perp \tag{2.15}$$

$$\xi_1 = \mathbf{v}_1/|\mathbf{v}_1| = \mathbf{v}_1/\sqrt{N}, \tag{2.16}$$

$$\xi_\perp = \left(\mathbf{v}_m - (\xi_1^{\mathrm{H}}\mathbf{v}_m)\xi_1\right) / \left|\mathbf{v}_m - (\xi_1^{\mathrm{H}}\mathbf{v}_m)\xi_1\right|. \tag{2.17}$$

These equations below were obtained from RMT results derived from spiked covariance model [14]. After matching these equations to single interferer case, it turns out to be

$$|\mathbf{e}_1^{\mathrm{H}}\xi_1|^2 \to \begin{cases} \frac{1-c/(N\sigma_1^2)^2}{1+c/(N\sigma_1^2)}, & \sigma_1^2 > \sqrt{c}/N, \\ 0, & \sigma_1^2 \le \sqrt{c}/N \end{cases} \tag{2.18}$$

$$|\mathbf{e}_1^{\mathrm{H}}\xi_\perp|^2 \to (1/N)\left(1 - |\mathbf{e}_1^{\mathrm{H}}\xi_1|^2\right) \tag{2.19}$$

substituting these equations in (2.15-2.16)

$$\mathrm{ND} \approx \mathrm{ND}_{cbf} \frac{|A_1(c)A_2(c)|^2}{|A_3(c)|^2}, \tag{2.20}$$

$$\mathrm{ND}_{cbf} = \cos^2(\mathbf{v}_m, \mathbf{v}_1), \tag{2.21}$$

$$A_1(c) = \left(1 - e^{j\phi} \tan(\mathbf{v}_m, \mathbf{v}_1)\sigma_1\sqrt{c}\right), \tag{2.22}$$

$$A_2(c) = \left(1 - e^{-j\phi} \cot(\mathbf{v}_m, \mathbf{v}_1)\sigma_1^{-1}\sqrt{c}\right), \tag{2.23}$$

$$A_3(c) = 1 + N\sigma_1^2 \sin^2(\mathbf{v}_m, \mathbf{v}_1) + c \tag{2.24}$$

where $e^{j\phi}$ is the phase of $\xi_1^{\mathrm{H}}\mathbf{e}_1\mathbf{e}_1^{\mathrm{H}}\xi_\perp$. Assumptions of this model are $N \gg 1, N\sigma_1^2 \gg 1, (N\sigma_1^2)^2 \gg c$, and the interferer lies outside the main lobe of the CBF for the given look direction.

This outcome can be understood in a similar way like the Bode plot which is straight forward sketch of linear piece approximation of ND vs. L on a logarithmic plot.The boundaries for the various linear regions are found by finding c (dependent on L) values.The transition points of c values are analogous to breakpoint frequencies for a frequency response bode plot. This analysis predicts that the numerator has breakpoints $\sqrt{c} = cot(\mathbf{v}_m, \mathbf{v}_1)\sigma_1^{-1}$ and $\sqrt{c} = \tan(\mathbf{v}_m, \mathbf{v}_1)\sigma_1$ and the denominator has a second-order breakpoint (relative to $\sqrt{c}$ at $1 + N\sigma_1^2 \sin(\mathbf{v}_m, \mathbf{v}_1)$. For c above this breakpoint, the model holds ND constant at $\mathrm{ND}_{\mathrm{cbf}}$. It is easier to represent the breakpoints in terms of snapshots :

$$L_1 = 1/(\sigma_1^2 \sin^2(\mathbf{v}_m, \mathbf{v}_1)), \tag{2.25}$$

$$L_2 = N \cot^2(\mathbf{v}_m, \mathbf{v}_1)/\sigma_1^2, \tag{2.26}$$

$$L_3 = N\sigma_1^2 \tan^2(\mathbf{v}_m, \mathbf{v}_1) \tag{2.27}$$

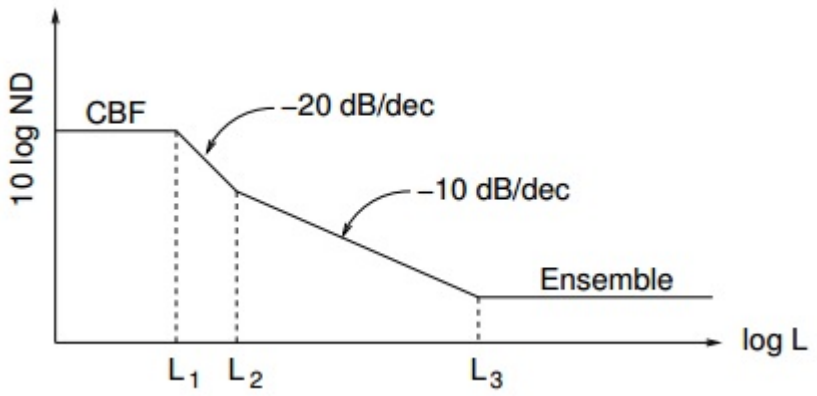

Figure 2.4: Model for beampattern notch depth in dB vs. log snapshots for a given INR and array size N [4].

Figure 2.4 summarizes this model graphically in terms of the breakpoints in (2.24 to 2.26). Below L_1 snapshots, the DMR ABF is same as the CBF at attenuating a loud interferer. The model also predicts the number of snapshots L_3 required to achieve the ensemble notch depth $\mathrm{ND}_{\mathrm{ens}}$ [4].

2.4.2 RMT model for ND vs. INR :

The model can also be derived by treating INR σ_1^2 as the independent variable. Following the same process as above and assuming that $N\sigma_1^2 \gg \sin^2(\mathbf{v}_m, \mathbf{v}_1)$ and $c \ll 1$ results with ND_{ens} given in (2.27).

$$\mathrm{ND} \approx \mathrm{ND}_{ens}\mathrm{ND}_{res}, \tag{2.28}$$

$$\mathrm{ND}_{res} = |\sigma_1(\tan(\mathbf{v}_m, \mathbf{v}_1)\sqrt{c}) - (1+c)|^2, \tag{2.29}$$

The notch depth can track the ensemble value, starting at $\mathrm{ND}_{\mathrm{cbf}}$ then rolling off with a *slope* $= -2$ at the break point, $INR_1 = 1/N \sin^2(\mathbf{v}_m, \mathbf{v}_1)$. However, above the critical value $INR_2 = (1+c)^2/c \tan^2(\mathbf{v}_m, \mathbf{v}_1)$, the notch depth has slope equal to -1. Fig. 2.5 summarizes this model for ND vs INR.

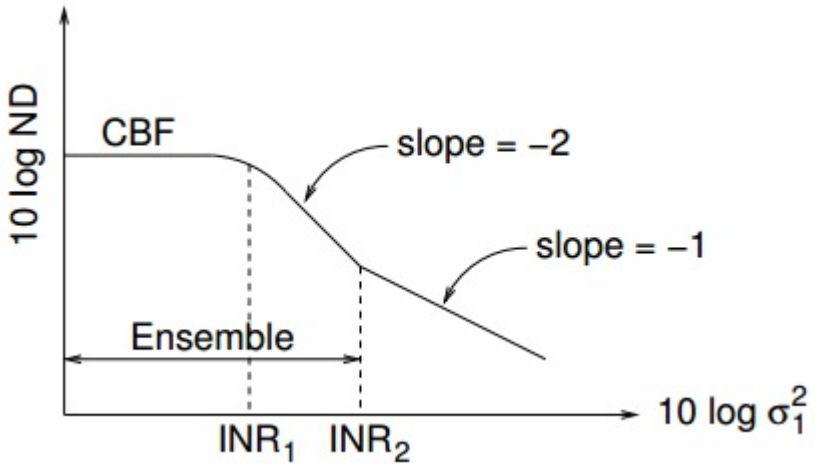

Figure 2.5: Model for beampattern notch depth in dB vs. INR in dB for a given array size N and number of snapshots L for the snapshot sufficient and rich cases, $c \ll 1$ [4].

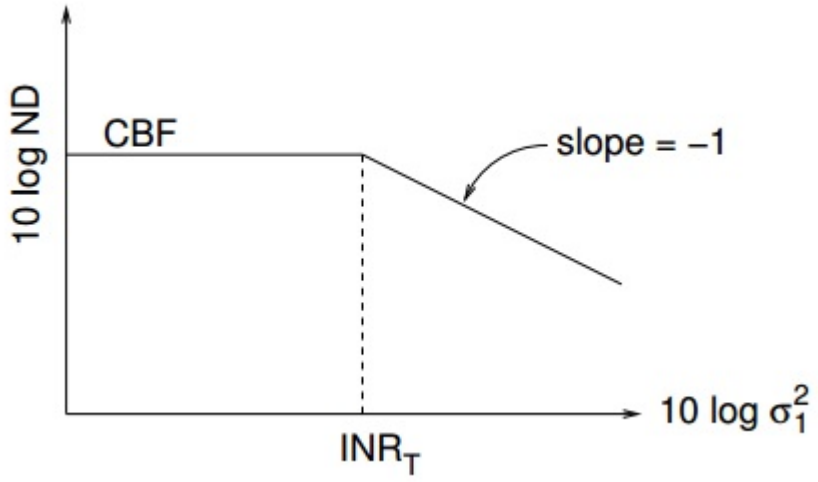

Figure 2.6: Model for beampattern notch depth in dB vs. INR in dB for a given array size N and number of snapshots L for the snapshot sufficient and rich cases, $c \gg 1$ [4].

For $c \gg 1$, the phase transition threshold $\sqrt{c}/N$ for the SCM eigenstructure in (2.9) may exceed both INR_1 and INR_2. Under these conditions, the notch depth remains fixed at ND_{cbf} until the INR exceeds the phase transition threshold $INR_T = \sqrt{c}/N$, and then rolls off with a slope of -1. The ensuing model is shown in Figure 2.6.

Chapter 3: Simulations

This chapter investigates the performance of DMR beamformer for a single interferer and multiple interferer cases using simulated data. The study of this thesis is based on the fact that interferers lies outside the main lobe because when interferers are inside the main lobe, the beamformer's performance goes awry. This chapter of the thesis analyses the cases where location of interferer is at peak side lobe of CBF for a single interferer case and the effect of interferer's location for a multiple interferer case.
Sec. 3.1 outlines the simulation parameters used for simulations in Chap. 3. Section 3.2 presents the distribution of DMR beamformer notch depth for single and multiple interferer cases. Section 3.3 and section 3.4 presents the RMT model predictions for ND vs. L and ND vs. INR and measured simulated notch depth of DMR Beamformer for a single and multiple interferer cases. Finally, Section 3.5 presents the effect of interferer locations on comparing the predictions of INR, ND vs. L to its simulated values.

3.1 Simulation Parameters

The parameters which are used for simulation are number of sensors N = 31, the replica vector in the look direction is steered towards broadside (0 degrees). The sample beampatterns are plotted along a Kz as axis, where the Kz value changes from -0.1571 to 0.1571 with an increment of 0.06. These Kz values are selected from the spatial spectrum of the experimental data used in chapter 4. The white noise power σ_w^2 is considered to be 1 and wave length λ as 1. The distance between two consecutive sensors is half that of the wavelength i.e 0.5. Both the interferer (plane wave signal p) and the noise(n) are modeled as complex circular Gaussian random variables.

3.1.1 Single interferer case

For a single interferer case, the location of u_i is assumed to be at 0.0252. The Sample beampattern is shown in fig 2.3 in chapter 2 for a single interferer case.

3.1.2 Multiple interferer case

The multiple interferer cases chosen are 7 for comparison of ND vs. INR predictions and simulated values while it is 3 and 14 for ND vs. L consideration. This is because that for ND vs. INR we need to have sufficient number of interferers as each one represents a INR value.
In the multiple interferer environment, the location of interferers are considered to be at peak side lobes as the DMR is an adaptive beamformer, it has the ability to notch the interferer irrespective of the location unlike the conventional one. The locations of interferers,u_i are

approximately orthogonal to each other.
In other case, the locations of interferers are considered to be non orthogonal. In the section 3.4 , a three interferer case is taken as example to illustrate the effect of interferer's.

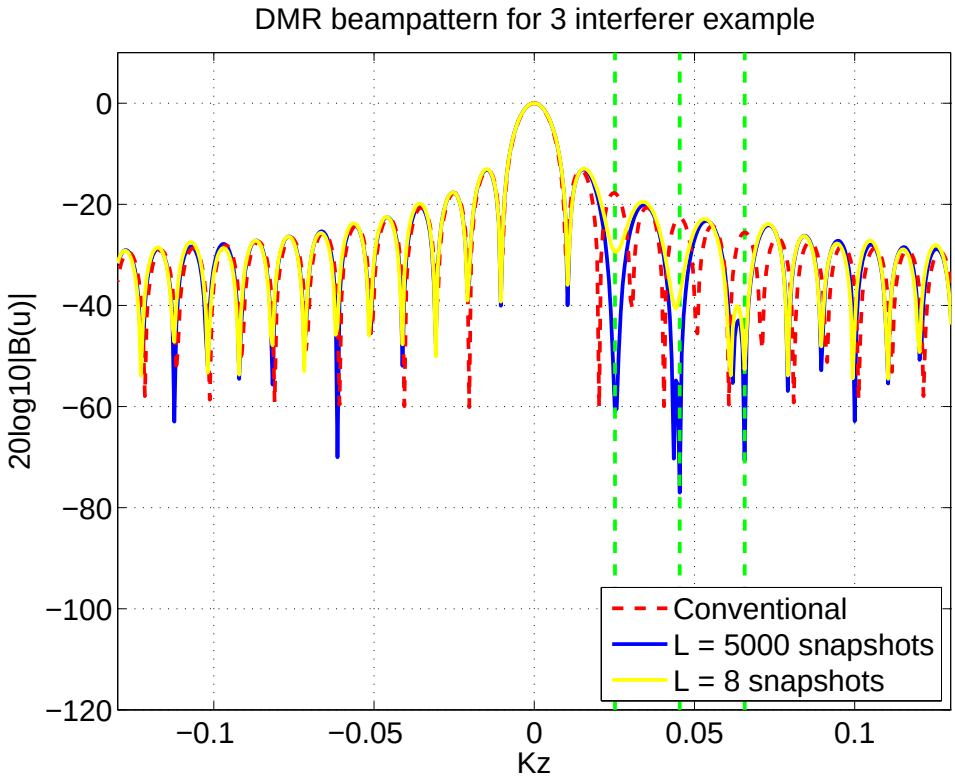

Figure 3.1: DMR beampattern for a 3 interferer case with their locations at 0.0252,0.04541 and 0.0657. The INRs assocaited with them are 10, 20 and 30 respectively.

The above beampattern for a 3 interferer case illustrates that higher the number of snapshots more effective is their notch. In Figure 3.1, the 5000 snaphots has a deeper notch when compared to 8 snapshot DMR beamformer which clearly explains the scenario.

3.2 DMR ND Distribution

This section describes the distribution of DMR notch depth for simulated data. It is known that ND is a scaled beta-prime random variable whose pdf is defined as shown below [8]:

$$f_{ND} \sim \beta' = \frac{N \cdot \mathrm{INR} \cdot L}{(1 + N \cdot \mathrm{INR} \cdot \mathrm{ND})^{(L+1)}}. \tag{3.1}$$

The histogram in Fig 3.2 shows that the beta-prime distribution fits the simulated ND data well for any snapshot number in the case of single interferer.

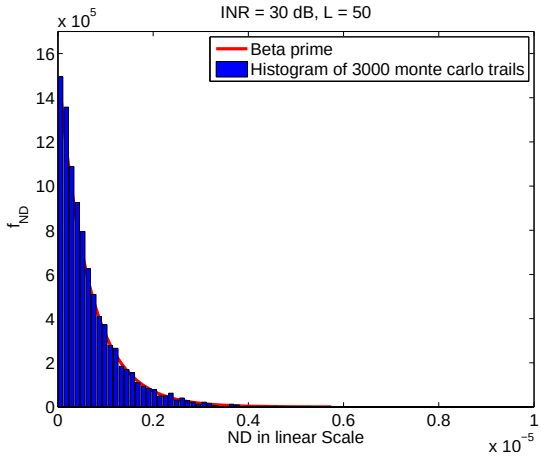

Figure 3.2: Beta-prime distribution overlaid on the notch depth histogram for the single interferer case. The INR is 30 dB and the DMR ABF was computed using L = 50 snapshots

The mean and standard deviation of ND for a single interferer is given by:

$$\mathcal{E}(\text{ND}) = \frac{1}{N \cdot \text{INR} \cdot (L-1)} \tag{3.2}$$

$$std(\text{ND}) = \frac{1}{N \cdot \text{INR} \cdot (L-1)} \cdot \frac{\sqrt{L}}{\sqrt{L-2}}. \tag{3.3}$$

So, it turns that the mean and standard deviation of the above distribution to be $6.5833e{-}07$ and $6.7190e-07$ after substituting $N = 31, INR = 10^3, L = 50$ in the equations 3.2 and 3.3 which is same as the Monte Carlo simulations mean and standard deviation. The mean of the beta distribution for the single interferer case is $L/(L+1)$, which closely tracks the mean of the Monte Carlo simulations. The beta distribution parameters $a = L$ and $b = 1$ are used for matching the histogram of 3000 monte carlo trails of DMR notch depth.

3.2.1 Multiple interferer DMR ND distribution

The figure 3.3 shows the distribution of 3 interferer case with their INRs are 30, 25 and 20 dB respectively. The subplot is plotted for L = 50 snapshots for each interferer respectively.The locations of the interferers u_i are chosen as 0.0252,0.04541 and 0.0657 (Considering the peak side lobes as shown in figure 3.1).

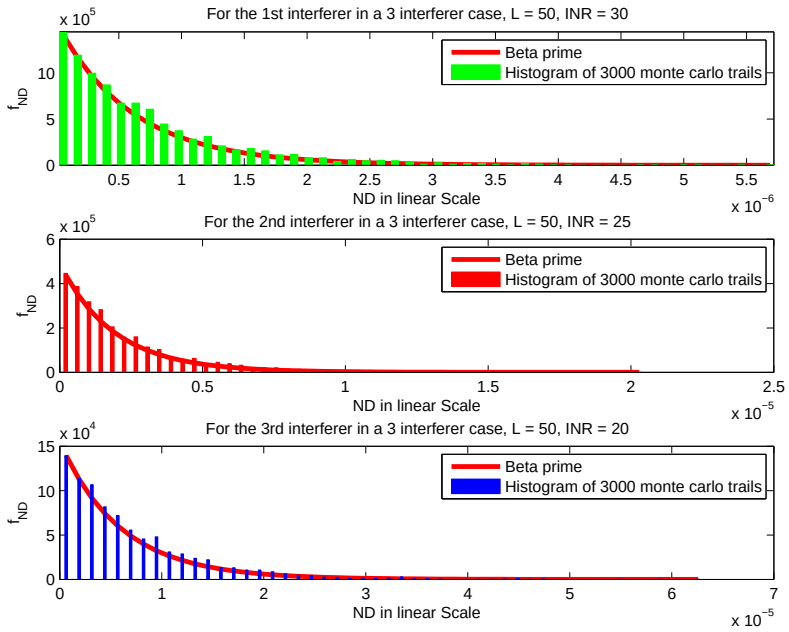

Figure 3.3: Beta-prime distribution overlaid on the notch depth histogram for multiple interferer case of INRs 30, 25 and 20 dB. The DMR ABF was computed using L = 50 snapshots with interferer locations orthogonal to one and other.

The pdf formula of ND which was used conjecturally for beta prime estimation by KS test (5 % significance) confirms that a beta distribution for parameters a = L-D+1 and b = D is

$$f_{ND} \sim \beta' = \frac{N \cdot \mathrm{INR} \cdot L}{(1 + N \cdot \mathrm{INR} \cdot \mathrm{ND})^{(L+D+1)}}. \tag{3.4}$$

where D = 3, L = 50 in the figure 3.3 are used to find the beta prime estimate.
The figure in the subplot illustrates that the 30 dB INR (which is green in color is for a first interefer) has the higher amplitude than the 25 dB INR (red in color, the second interferer) which has higher amplitude than the 20 dB (which is blue in color, the third interferer).
In figure 3.4, for L =500 snapshots with INR being same and the interferer locations u_i are chosen as 0.0252, 0.04541, 0.1062(changing an interferer location).

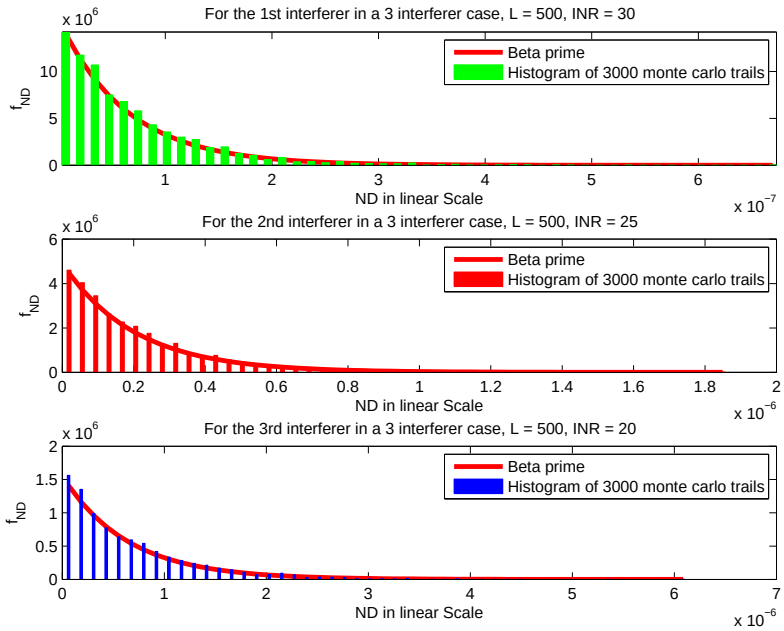

Figure 3.4: Beta-prime distribution overlaid on the notch depth histogram for multiple interferer case of INRs 30, 25 and 20 dB. The DMR ABF was computed using L = 500 snapshots with interferer locations orthogonal to one and other.

It was observed that, the ND distribution for each of the INR for multiple intereferers is still beta prime which was again confirmed by KS test(5 % significance).
Hence, It can be concluded that ND distribution for multiple interferer case also follows beta prime distribution like the single interferer case [8].

3.3 Validation of DMR ND vs. L using RMT Model

This section compares the RMT models prediction for ND as a function of snapshots L with the average notch depth observed in simulations. The results are illustrated on a log-log scale (10 log ND vs. log snapshots) as shown in figure 3.5, 3.6 and 3.7.

Single Interferer case

For a single interferer case, the rank of the DMR ABF is 1 i.e., it considers a single plane wave model. The dashed lines indicate the model predictions and each discrete symbol represents the mean of 3000 Monte Carlo trials.
The subset of snapshots considered are 3, 15, 31, 62, 155, 310, 620 and 1153 respectively. The different colors and symbols indicate varying sensor level of INRs between 0 and 40 dB. The interferer location was at $u_i = 0.04541$; which is near peak side lobe of the CBF for the array size, N = 31. In figure 3.4 , it is observed that for all five INRs, the model accurately predicts the mean notch depth seen in the 3000 Monte Carlo simulations. All of these scenarios have L2 $<$ 3 snapshots, so they lie -10 dB/decade region by the first data

point at L = 3 snapshots (refer chapter 2.36 to 2.38 equations). These RMT predictions can be extended to the ensemble statistics of DMR [4].

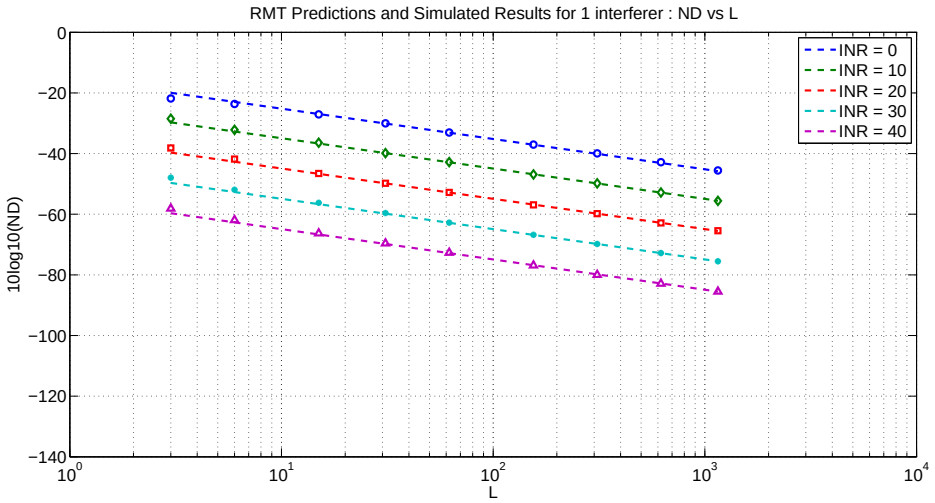

Figure 3.5: Comparison of model predictions (dashed lines) and Monte Carlo simulations (discrete symbols) for mean beampattern notch depth in dB vs. log snapshots for a single interferer case.

Multiple Interferer case

This subsection deals with the multiple interferer case i.e., when the rank of the DMR, D is greater than 1. The below Figure 3.6 and 3.7, is a result of 14 interferer case with INRs ranging from -16 dB to 36 dB with an increment of 4 dB for each interferer. The subset of snapshots considered are 15, 19, 31, 62, 155, 310, 620, 1153, 2500 and 5000 respectively. The different colors and symbols indicate varying sensor level INRs between -16 and 40 dB in figure 3.5, 3.6 and 3.7. The dashed lines is the predicated values of the RMT model while the solid lines with discrete symbols are the averaged values of ND for 3000 Monte Carlo trails in figures 3.6, 3.7 and 3.8.

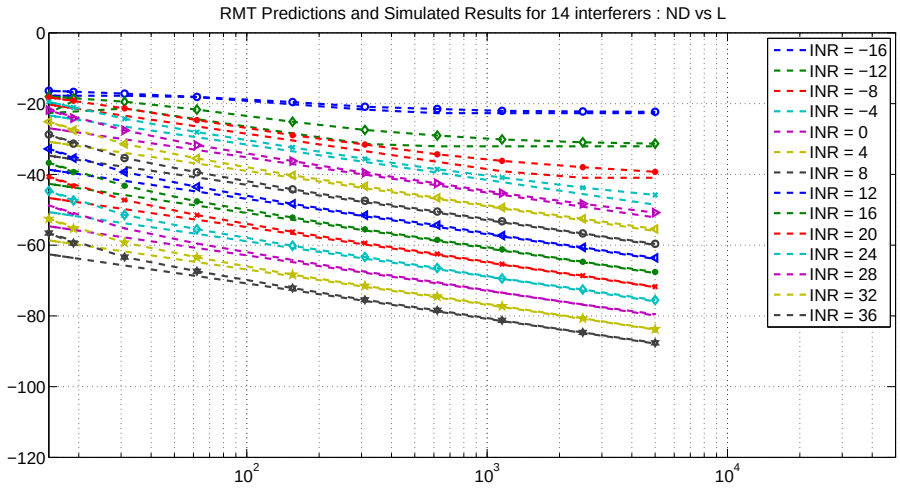

Figure 3.6: Comparison of model predictions (dashed lines) and Monte Carlo simulations (solid lines with discrete symbols) for mean beampattern notch depth in dB vs. log snapshots for a 14 interferer case.

The above figure is plotted by considering the interferer locations orthogonal to one and other. The interferer locations u_i are $0.0252, 0.04541, 0.0657, 0.0859, 0.1062, 0.1264, 0.1466, -0.1466, -0.126$ 0.0252 respectively. The generalized cosine between the replica vectors of the interferer locations are less than 0.003 considering the peak side lobe of the CBF. For higher INR, it is observed that more number of snapshots were required to agree with the RMT model predictions. For 36 dB, say around 31 snapshots were required to meet the predictions.
For lower INRs, the average ND values seem to deviate from the RMT model predictions. This scenario is observed in the INRs ranging from 0 to -14 dB.

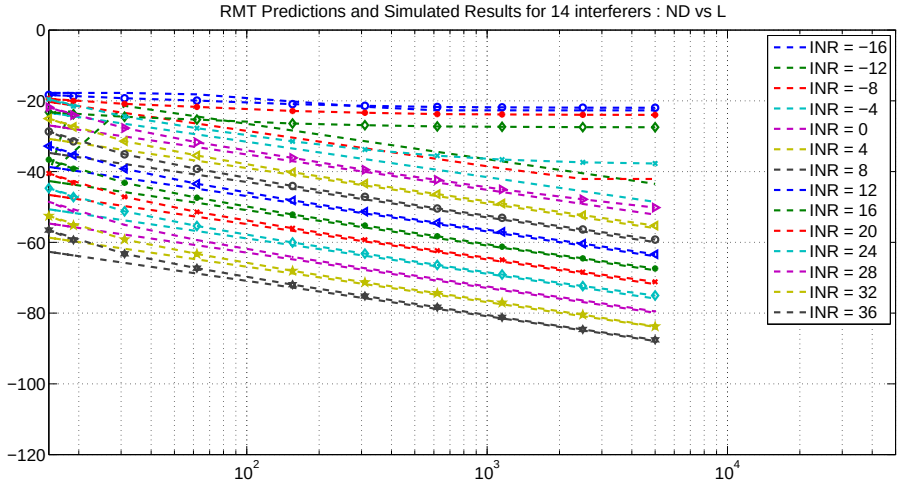

Figure 3.7: Comparison of model predictions (dashed lines) and Monte Carlo simulations (discrete symbol lines) for mean beampattern notch depth in dB vs. log snapshots for a 14 interferer case when the interferer locations are not orthogonal.

The above figure 3.7 is plotted for interferer locations 0.0252,0.03068 0.03191, 0.04172,0.04786, 0.06627, 0.08283, 0.1019, 0.1074, 0.01774, 0.02884, -0.04111, -0.05216 and -0.06872 respectively. These interferer locations are taken randomly and the generalized cosine squared between the interferer locations range from 0.3 to 0.92. For lower INRs, a lot more deviation is observed w.r.t figure 3.6. It also illustrates that more number of snapshots i.e., 62 are required to meet the model predictions than the previous 31.

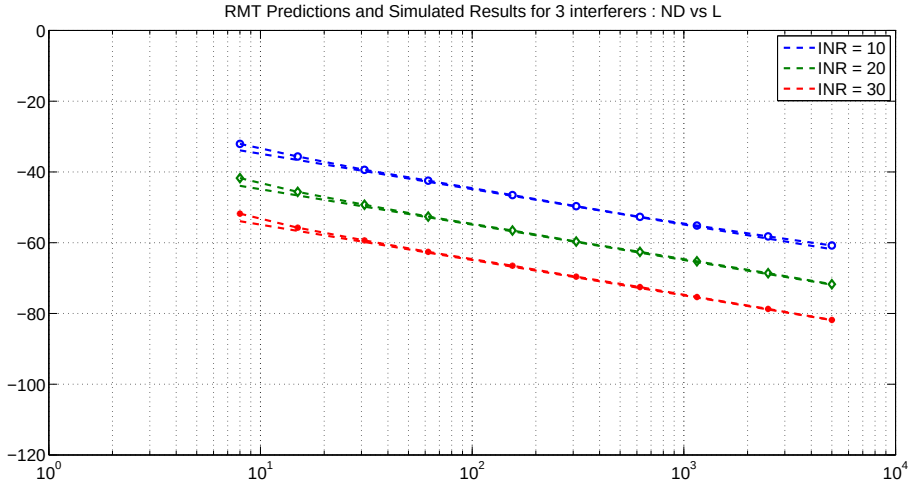

Figure 3.8: Comparison of model predictions (dashed lines) and Monte Carlo simulations (discrete symbol lines) for mean beampattern notch depth in dB vs. log snapshots for a 3 interferer case.

The above figure 3.7 illustrates the ND vs.L plot for 3 interferer case for INRs 10, 20 and 30 dB at locations which are approximately orthogonal. For the multiple interferer cases, it is observed that the "D+1" snapshots are not sufficient to agree the RMT model predictions, even though these snapshots might be enough to attenuate a loud interferer. The minimum of number of snapshots that are required to validate the model from rank 3 to 14 is 31. The Lower INR values i.e $\leq$ 0 dB lie in the region $<$ L1 (refer equations 2.36 to 2.38) while the higher INR values lie in the region $<$L2.

3.4 Validation of ND vs. INR model using RMT

This section compares the model predictions for ND as a function of INR for different snapshots as L varies from 4 to 5000 which implies ratios of sensors to snapshots as c varies from 10^1 (snapshot deficient) to 10^{-3} (snapshot rich).

Single Interferer case

This subsection deals with a single interferer case of DMR i.e., the rank of DMR ABF is one. The dashed lines indicate the model predictions and the discrete symbols are the results from the same Monte Carlo simulations used for Figure 3.4. The model predicts the

performance of the snapshot sufficient cases c < 1 i.e., L$>$ 31 snapshots, up to the critical breakpoint at $INR_2 = (1+c)^2/c\tan^2(\mathbf{v}_m, \mathbf{v}_1)$, and then decreasing with a slope of -1 beyond that INR. For the snapshot deficient case (c = 7.75), the notch depth follows the form predicted in Fig.3.8, remaining flat at the CBF value (-17.77 dB) until INR_{T}. The greatest discrepancy between the model and simulations occurs for the case c = 7.75 i.e., L = 4 snapshots in, which does not agree in the regions after -10 dB.

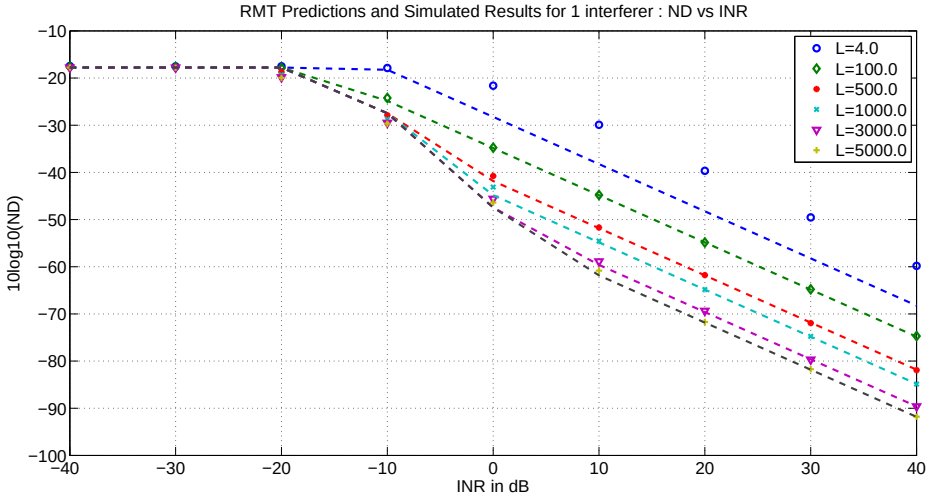

Figure 3.9: Comparison of model predictions (dashed lines) and Monte Carlo simulations (discrete symbols) for mean beampattern notch depth vs. INR as the sensor to snapshot ratio varies from snapshot deficient (L = 9) to snapshot extravagant (L = 5000) for a 1 interferer case.

In the other cases of L,the simulated mean ND values match the predictions of ND vs .INR model. The transition period occurs for $c \leq 1$ as shown in figure 2.4, but in this case considering as the increment of 10 dB INR for each averaged ND value overshadows the transition state [4].

Multiple Interferer case

This subsection deals with the multiple interferer case i.e., when the number of plane wave signals are more than 1 as indicated in equation 2.1. The below Figure 3.9 and 3.10, is a result of 7 interferer case with INRs ranging from -20 dB to 36 dB with an increment of 4 dB for each interferer. The subset of snapshots considered are 9, 100, 500, 1000, 3000 and 5000 respectively. The different colors and symbols indicate varying snapshots between 9 and 5000 in figure 3.9 and 3.10. The dashed lines is the predicated values of the RMT model while the solid lines with discrete symbols are the averaged values of ND for 3000 Monte Carlo trails in figures 3.9 and 3.10.

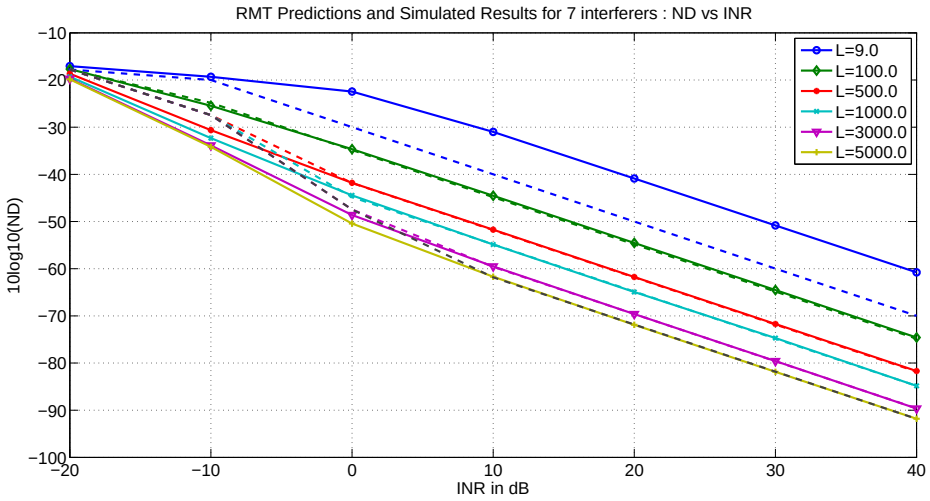

Figure 3.10: Comparison of model predictions (dashed lines) and Monte Carlo simulations (discrete symbols) for mean beampattern notch depth vs. INR as the sensor to snapshot ratio varies from snapshot deficient (L = 9) to snapshot extravagant (L = 5000) for a 7 interferer case.

The above figure is plotted by considering the interferer locations orthogonal to one and other. The interferer locations u_i are 0.0252, 0.04541, 0.0657, 0.0859, 0.1062, 0.1264 and -0.1264 respectively. The generalized cosine between the replica vectors of the interferer locations are less than 0.003 considering the peak side lobe of the CBF. This can be treated as approximately orthogonal to one and other.
For higher number of snapshots, the mean ND values agree with the RMT model predictions of ND vs. INR. For lower number of snapshots, the average ND values seem to deviate from the RMT model predictions. The largest discrepancy is observed in the transition region of INR_1 and INR_2 as shown in figure 2.4 .

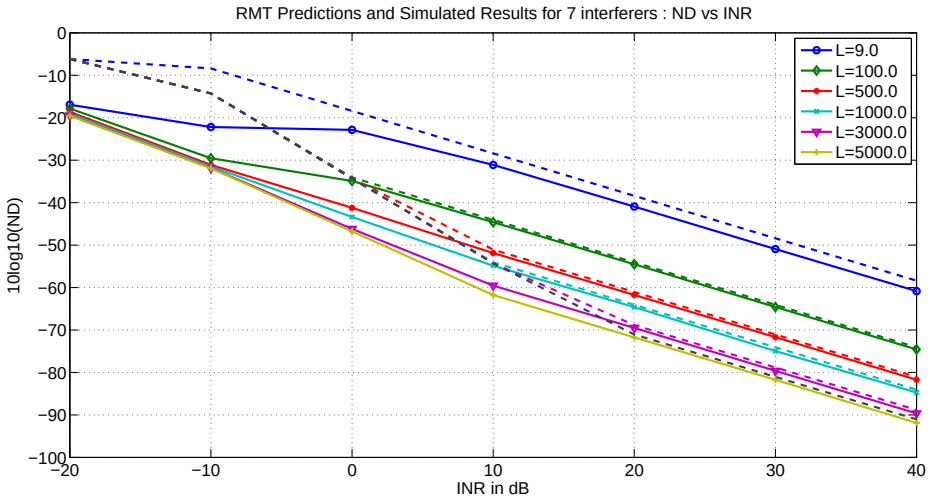

Figure 3.11: Comparison of model predictions (dashed lines) and Monte Carlo simulations (discrete symbols with solid lines) for mean beampattern notch depth vs. INR as the sensor to snapshot ratio varies from snapshot deficient (L = 9) to snapshot extravagant (L = 5000) for a 7 interferer case when their interferer locations are not orhtogonal.

The above figure 3.11 is plotted for interferer locations 0.0252, 0.03068, 0.03191, 0.04172, 0.04786, 0.06627 and 0.08283 respectively. These interferer locations are taken randomly and the generalized cosine squared between the interferer locations range from 0.3 to 0.92. It is observed that when the interferer locations are not orthogonal to each other, for all low INR values $< 10dB$, the mean ND values does not agree with the model predictions. There is also a deviation in the transition region similar to the figure 3.10. The major difference is the shift of the CBF region where the predicted values of the model are shifted by more than 10 dB when the interferer locations are not orthogonal to each other. This shows that the interferer's have a major effect in the ND vs. INR model for a multiple interferer case.

3.5 Effect of Interferer location

This section deals with the effect of interferer locations on the ND, INR, ND vs. L model plots. For this simulation a 2 interferer example is considered where the interferer locations are at 0.03559,0.05584 initially. Now these interferer locations are interchanged with varying distances with a increment of 0.0014 as shown in the below beampattern figures 3.12, 3.13 and 3.14. The INRs are chosen to be 20 and 10 dB.

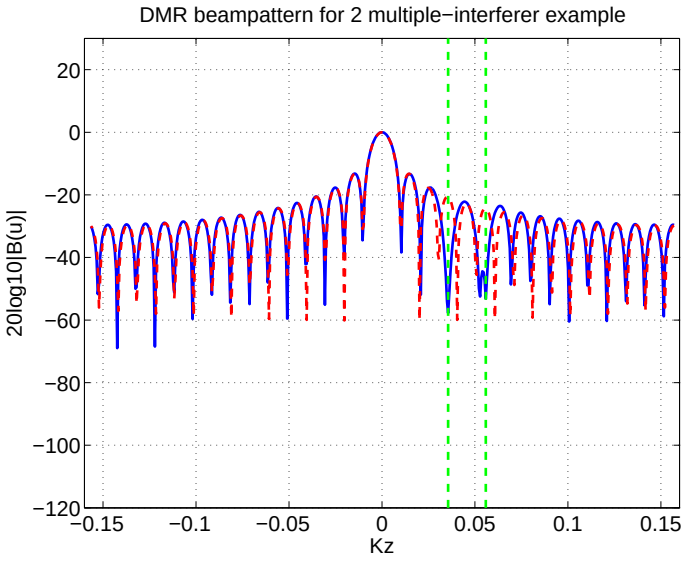

Figure 3.12: Beampattern for 2 interferer example at interferer locations 0.0356,0.0558

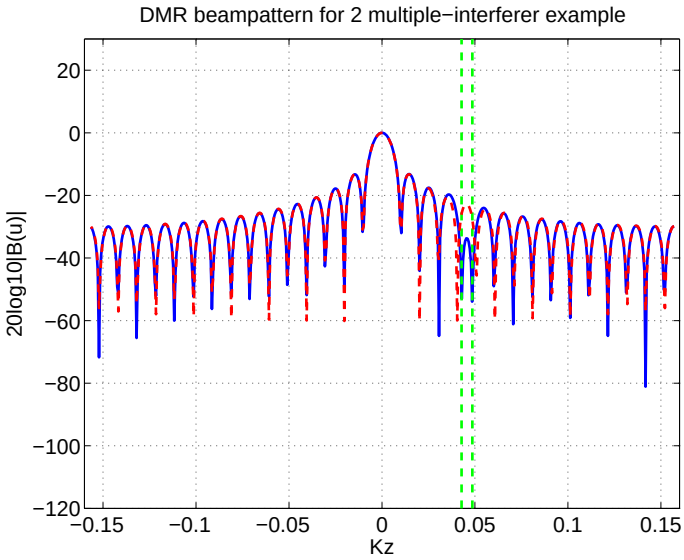

Figure 3.13: Beampattern for 2 interferer example at interferer locations 0.0443,0.0472

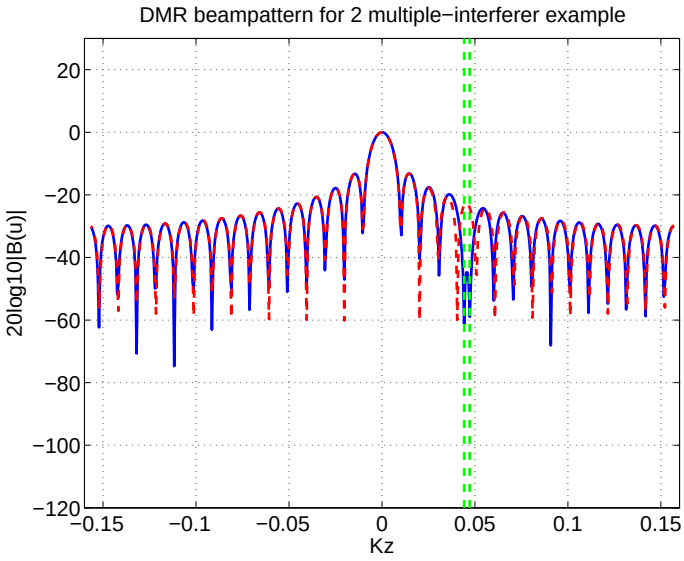

Figure 3.14: Beampattern for 2 interferer example at interferer locations 0.0455,0.0459

3.5.1 Change of ND dependent on Ui

This subsection illustrates how the ND changes with respect to the interferer locations.The below figure 3.15 explains the scenario. The ND barely changes with respect to $cos^2(v_i, v_m)$ where the v_m is the replica vector of the look direction and the v_i is the replica vector at the interferer location. The blue and green colored lines with discrete symbols represent the measured ND values for INRs 20 and 10 dB.

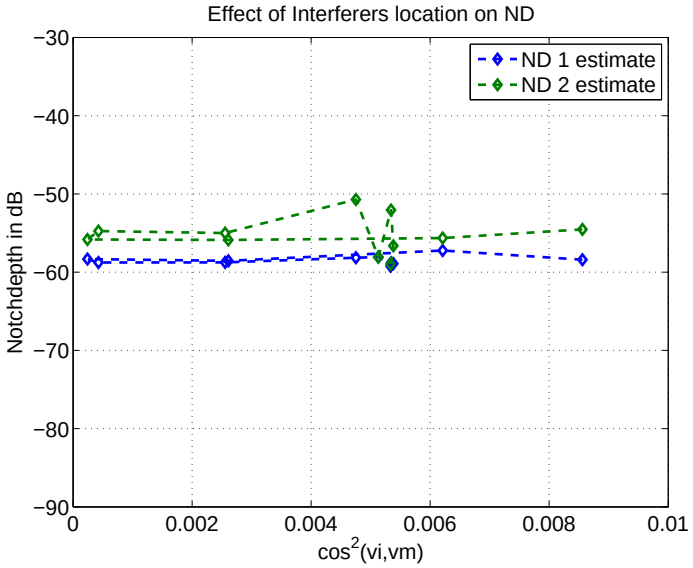

Figure 3.15: Effect of u_i on ND

When the notch depth estimates of interferer locations 1 and 2 are same at the time when

the location of interferers are exactly same i.e., the rank of the DMR becomes 1. This is shown in the above figure at $cos^2(v_i, v_m) = 0.005$. The ND does not change significantly which is evident from the fact that the distribution of ND does not change w.r.t the u_i. It is well known fact that, the interferer at null would have a deeper notch than the interferer at a peak side lobe [5]. But the effect of it is minor on the validation of the RMT model plots unless the rank of interferer changes(in this case from 2 to 1).

3.5.2 Deviation of INR based on the location of Interferers

This subsection deals the change in INR with respect to the interferer locations.The below figure 3.16 explains this scenario. As we know, the INR is estimated from the data using the equation 2.23.

$$INR = (\frac{\gamma_1}{N\sigma_1^2} - \frac{1}{N})$$

The INR is dependent on the most dominant eigenvalue. It is observed that the INR_2 drastically changes with the $cos^2(v_i, v_m)$ where the v_m is the replica vector of the look direction and the v_i is the replica vector at the interferer location. The blue and green colored lines with discrete symbols represent the measured INR values for interferer 1 and 2.

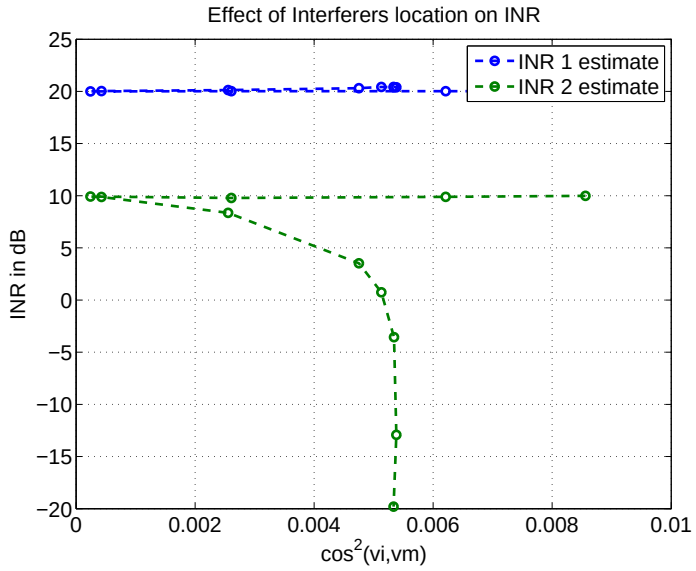

Figure 3.16: Effect of u_i on INR

INR calculation for Experimental data :

The INR is the defined as ratio of σ_1^2/σ_w^2. The most dominant eigenvalue is given by

$$\gamma_1 = N\sigma_1^2 + \sigma_w^2 \tag{3.5}$$

$$\sigma_1^2 = \frac{\gamma_1 - \sigma_w^2}{N} \tag{3.6}$$

$$INR = \frac{\sigma_1^2}{\sigma_w^2} \tag{3.7}$$

$$INR = (\frac{\gamma_1}{N\sigma_1^2} - \frac{1}{N}) \tag{3.8}$$

In this thesis, N = 31. The above discussion describes how to calculate the exact values from the dataset.

The INR_2 estimate is decreasing drastically and INR_1 estimate slightly increases at $cos^2(v_i, v_m)$ =0.005 i.e when the interferers are getting close and are equal.
The INR_2 decreases up to -20 dB and INR_1 increases to 20.5 dB which is due to the fact that when the inteferers get closer to each other, there is transfer of energy taking place from lower INR to the higher INR. The value of INR changes due to the dependency of its estimation on γ_1, the most dominant eigenvalue of the DMR Beamformer. As the distance between the interferer changes, the γ_1 varies hence the estimated INR values change.

3.5.3 Change of ND vs.L dependent on Ui

This subsection investigates the comparison of mean ND values to its predictions of the ND vs. L. The L snapshot values used for these simulation are 7, 15, 31, 62, 155, 310, 620 and 1153 respectively. Below figure 3.17 is a the initial plot of ND vs. L and its model predictions with interferer locations to similar to those as shown in figure 3.12.

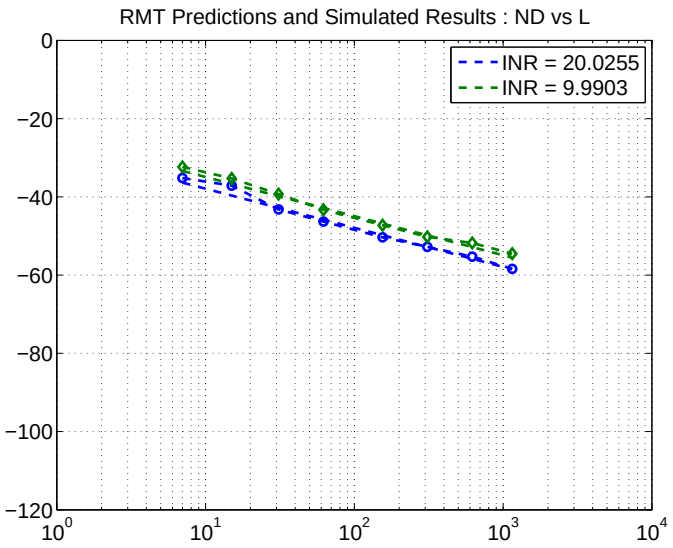

Figure 3.17: Comparison of model predictions (dashed lines) and Monte Carlo simulations (discrete symbols with dashed lines) for mean beampattern notch depth in dB vs. log snapshots for a 2 interferer case at $u_i = 0.0356, 0.0558$.

In the figure 3.18, is a initial plot of ND vs. L and its model predictions with interferer locations are shown in figure 3.13. Here we could observe that the INR of the second interferer is changing when the interferers are getting slightly closer.

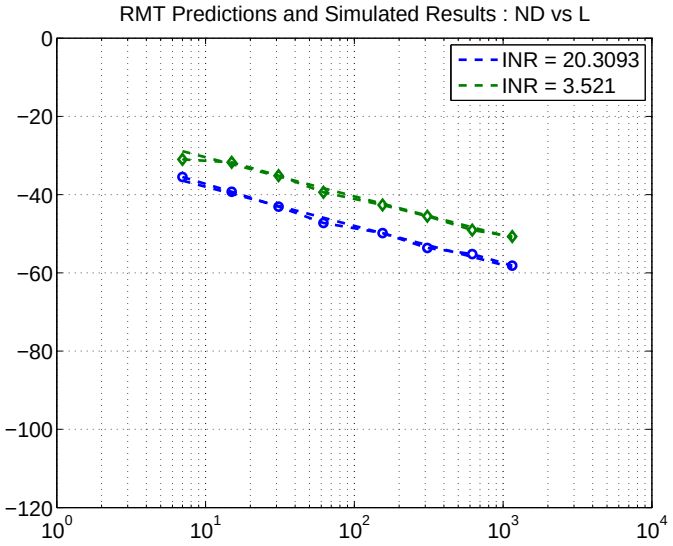

Figure 3.18: Comparison of model predictions (dashed lines) and Monte Carlo simulations (discrete symbols with dashed lines) for mean beampattern notch depth in dB vs. log snapshots for a 2 interferer case at $u_i = 0.0443, 0.0472$.

In the figure 3.19, is a initial plot of ND vs. L and its model predictions with interferer locations are similar to those as shown in figure 3.14. Here we could observe that the INR of the second interferer is significantly changing when the interferers are getting closer.

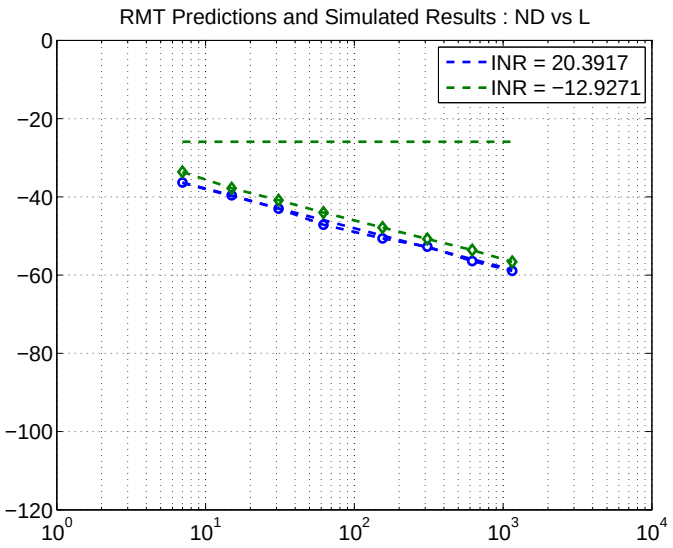

Figure 3.19: Comparison of model predictions (dashed lines) and Monte Carlo simulations (discrete symbols with dashed lines) for mean beampattern notch depth in dB vs. log snapshots for a 2 interferer case at $u_i = 0.0455, 0.0459$.

So in this the rank of the DMR also diminshes to 1 from 2 as the interferers get closer to each other.
The comparison of mean ND values and its predicted values of ND vs. L change significantly is evident from the fact that the INR changes as u_i or the distance between the two inteferers varies.

3.6 Summary

Generally D+1 snapshots are enough for DMR to function as an adaptive beamformer, but to validate the model we require more than D+1 snapshots. When the INRs are same for all interferers, the eigenvalues would also be same for all the interferers hence the INRs are considered different for each interferer. The effect of u_i is more dominant on the INR, this makes the RMT model of ND vs. INR predictions go awry when the interferer locations are non orthogonal to each other.
The RMT model predictions were developed for a single interferer case. Hence for multiple interferer cases, the model does not satisfy for low INRs and snapshot deficient cases in the ND vs. L model.

Chapter 4: The Experiment

This chapter beigns with the details relating to the experiment PhilSea10. From there on, spatial spectrum estimation,eigenvalues and eigenvectors of the strum in the PhilSea10 have been dealt with. The selection of constant strum is explained penultimately. Lastly, various rank estimation techniques are discussed.

4.1 Philippines Sea Experiment 2010 2011

This experiment is a part of a series intended to study the methods developed in long range, deep water broadband acoustic propagation in the central and eastern North Pacific applied to research deep water acoustic propagation and ambient noise in the much more oceanographically and geologically complex northern Philippine Sea [16]. The series began with the 2009 NPAL Pilot Study/Engineering Test (PhilSea09), and continued with the 20102011 NPAL Philippine Sea Experiment (PhilSea10) and the Ocean Bottom Seismometer Augmentation of 20102011 NPAL Philippine Sea Experiment (OBSAPS).[16]
In this experiment, a full water-column-spanning distributed vertical line array (DVLA) which consists of five 1000-m sub arrays was placed surrounded by an array of six broadband acoustic transceivers (T1 to T6) to record the transmissions from the six sources and to study acoustic propagation and scattering during intermittent one year period starting from April 2010 to March-April 2011 [16]. Geographical location of every station and the DVLA are shown below in Figure 4.1.
Each acoustic transceiver has the ability to also record the transmissions from the other transceivers, forming a six component ocean acoustic tomography array with an ambit of roughly 330 km. Following deployment of the moorings, acoustic sources suspended from sea transmitted to the DVLA amid May 2010 and again during July 2010.

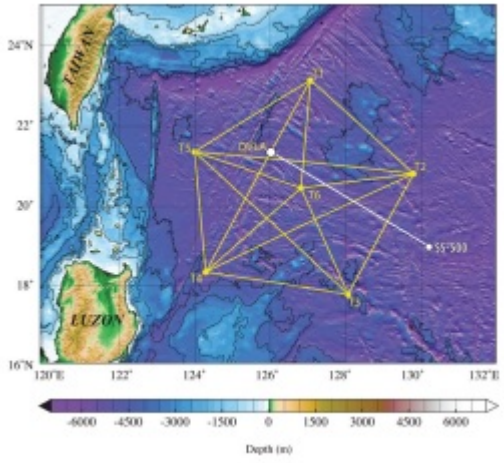

Figure 4.1: Geometry of PhilSea10 Experiment. Broadband acoustic transceivers were moored at T1 to T6. A DVLA receiver was moored at DVLA.

An array of four hydrophones spaced 9.0 m apart was placed on top of each source to record the transmissions from the other sources. In spite of the fact that source at T6 failed prematurely, the transceiver continued to record the transmissions from the other sources for the remainder of the experiment.

There ought to be 30 path combinations for acoustic propagation paths as ascertained, however, as a result of there was a clock drawback at T6, the signal that originated from that station couldn't be processed. As a result, the study only utilized 25 path combinations, which originated from the transceivers, T1 to T5.

Table 4.1: Moored acoustic source characteristics, depth and transmission times during PhilSea10. Average power levels are rms. Transmission times are in minutes after the hour.

	LFM Bandwidth(Hz)	Average power level (dB re 1μPa at 1 m)	Transmission Time (min)	Source Depth (m)
DVLA				
T1	$200-300$	184.4	0	1068.7
T2	$140-205$	183.8	9	1070.1
T3	$225-325$	181.9	18	1062.4
T4	$225-325$	182.7	27	1064.6
T5	$205-305$	184	36	1061.7
T6	$200-300$	185.8	45	1066.0
SS-500				998

4.1.1 Equipment Configuration

The DVLA recorded transmitted signals from all transceivers. The common transmitted power levels differed from 181.9 to 185.8 dB re 1μ Pa at 1 m rms. The sources transmitted

at each three hours on odd-numbered year days for the complete experiment. The transmissions started from a near north position and moved in a clockwise direction. Transmission started from T1, followed by T2, through T6. The transceivers transmitted a 135-s linear frequency modulated (LFM) with bandwidth 100 Hz. Central frequencies that transmitted at every station were 250 Hz but for T2 the central frequency was $104 - 205$ Hz. Sources T1 through T5 transmitted throughout the year. Source T6 failed untimely, with the last transmission occurring on year day 305 of 2010 (1 November 2010). To avoid interference the transmission from each station was separated by nine minutes every hour as shown in table 4.1 [16]. This nine-minute separation was chosen to give buffer time for the longest travel time calculated to be required for the longest distance between stations (637.818 km). Assuming sound speed in the ocean is 1500 m s^{-1} it takes seven minutes and five seconds for acoustic signal to travel from T2 to T4, and vice versa.

4.1.2 Distributed Vertical Line Array (DVLA)

The 5000 m long DVLA was anchored at the bottom and held vertical by a subsurface buoy. The DVLA consisted of five 1000−m subarrays, with a combined total of 150 receiving elements, called hydrophone modules with D-STAR controllers at the top of each sub array. The number of hydrophone modules varied from subarray to subarray as shown in the table 4.2. The hydrophone modules spanning the sound-channel axis, which is at $1000 - 1100$ m depth throughout the year at the DVLA location, were spaced 20 m apart to resolve the low-order modes for transmissions from the moored sources and the near-axial ship-suspended sources .The hydrophone modules were lot of wide spaced over the remainder of the water column to characterize the acoustic time fronts and ambient noise field.
In addition, the DVLA recorded continuously at times when the ship-suspended sources were scheduled to be transmitting, except for intervals once per hour to allow the long baseline navigation system to measure the mooring motion, as represented in the following text. Near the sound channel axis (SOFAR channel) the spacing is 20 m, and near the

Table 4.2: Nominal hydrophone module depths and spacing in the PhilSea10 DVLA.

Subarray	Depths (m)	Spacing (m)	Number of modules
1	$180 - 540$	40	10
	$580 - 1180$	20	31
2	$1200 - 2120$	40	47
	$2160 - 220$	40	2
3	$2280 - 3240$	60	17
4	$3360 - 4320$	60	17
5	$4383 - 5381$	40	26

critical depth the spacing is 40 m [17]. Figure 4.2 shows the depths of the 150 hydrophones on the PhilSea10 VLA. The depths of the 60 elements used during the month-long Pilot Study conducted in 2009 are also shown.

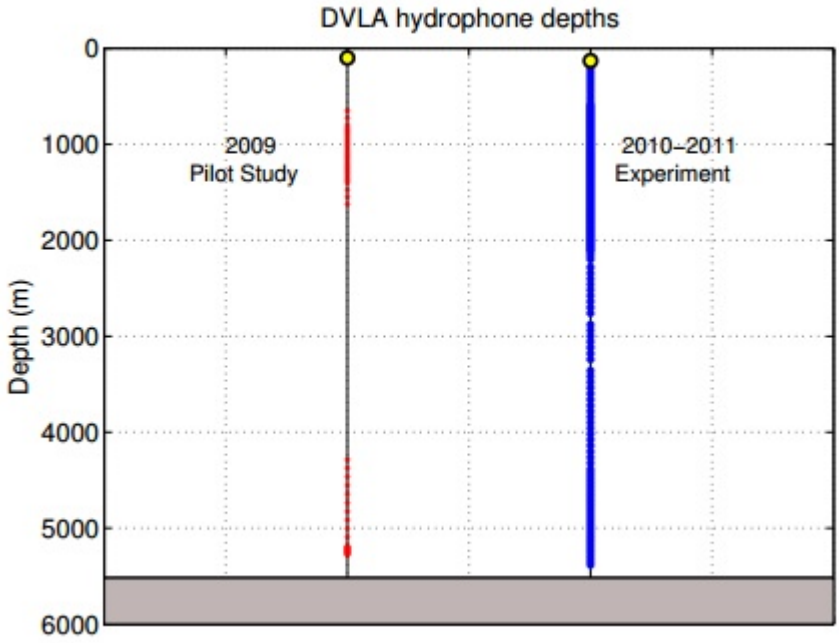

Figure 4.2: Depths of the hydrophones for the PhilSea09 and PhilSea10 experiments. The PhilSea09 array has 60 elements in two subarrays, one spanning the sound channel axis and the other spanning the critical depth. The PhilSea10 array has 150 elements spanning the entire water column.
This study focuses on data measured with a subset of 31 equally-spaced elements located near the top of the DVLA (spanning the depths 580 m to 1178 m).

4.1.3 Sources suspended from the ship SS–500

In the PhilSea10, the sources such as MP−200 Multiport, HX-554 and J15 − 3 were suspended from the ship SS−500, located 509.784 km to the east southeast of the DVLA as shown in figure 4.1. The MP−200 Multiport is a composite drive signal was built by summing two 1023-digits, phase-coded, periodic m-sequences with different carrier frequencies (200 and 300 Hz) but identical periods (20.4600 s), The periods were kept the same by using four cycles per digit for the 200-Hz signal and six cycles per digit for the 300-Hz signal. The rms source level was approximately 191 dB re 1l Pa at 1 m. The first transmission event throughout the cruise consisted of 55 h of transmissions in the longer receptions. The data set considered in this thesis consists this ship suspended source.
The HX−554 source is suspended at two different depths at 150 m and 998 m respectively. In its first event, it transimitted as a 1023−digit, phase coded, periodic m-sequence with a carrier frequency of 61.38 Hz and two cycles per digit. The rms source level was approximately 185 dB re 1μ Pa at 1 m. The last transmission occasion amid the cruise lasted for 54 h. During the final event, the HX−554 source transmitted a 2047−digit, phase-coded, periodic m-sequence with a carrier frequency of 81.88 Hz and two cycles per digit. The rms source level was approximately 186 dB re 1μ Pa at 1 m. The HX−554 ship suspended source is used in 55 h and 10 h receptions as shown in table 4.3.
The J15−3 source transmitted a mix of CW (Continuous Wave) and LFM signals at fixed

locations approximately one-half and one convergence zone from the DVLA and amid a number of tows. The J15−3 ship suspended source is used in 12 h, 36 h and 60 h receptions as shown in table 4.3.

4.1.4 DVLA Reception Schedule

The DVLA records all of the transmissions from the moored sources. Also, it records continuously at the times that the ship-suspended sources are transmitting. The DVLA sample rate for all acoustic receptions will be 976.5625 Hz.

T1 – T6 Receptions

During the Tomography schedule, the DVLA records for 155 s beginning ten seconds preceding to the nominal arrival times of the start of the LFM sweeps in order to provide approximately10-s buffer periods before and after the expected arrival times. The recording of transmissions from all the six transceivers (T1 – T6) can be classified as Discrete set of receptions. The timings of the moored transceivers are already mentioned in the table 4.1.The Topographies T2, T3, T4, T5, T6 were started on 130, 135,145,190,191 and 193 days during the Phil Sea 10 Experiment while T1 was started 8 h after spin up[18].

Continuous Receptions

The DVLA records continuously, except for intervals once per hour to take into account NAV tasks (no transmissions or disk writes) to measure the mooring motion (Section 4), at times when the ship suspended sources (HX–554, Multiport, J15–3) are scheduled to be transmitting. No separate moored source receptions occur during these periods i.e., no tomographies. The Hydrophone Modules are powered up throughout each continuous reception period. The HM clock is set once for each continuous reception, after allowing the HM oscillator to warm up for 400s [19]. There are total seven sets of continuous receptions

Table 4.3: The data set belonging to continuous receptions in PhilSea10.

Continuous deployment schedule	Start time (year day hour)	Hours of continuous receptions	Ship Suspended Source
1	128^{th} day 16^{th} Hour	55	HX-554
2	135^{th} day 00 Hour	10	HX 554
3	143^{rd} day 16^{th} Hour	55	Multiport
4	190^{th} day 00 Hour	12	J15–3
5	191^{st} day 00 Hour	12	J15–3
6	192^{nd} day 00 Hour	36	J15–3
7	198^{th} day 00 Hour	60	J15–3

/ longer receptions. The start dates and number of hours for the longer receptions are

deployed and are as shown in the table on the preceding page. There are 2 sets of 55 h and 12 h receptions and one set of 10, 36 and 60 h respectively.

The file recordings of continuous receptions have time stamps of 07 min for the first 45 min recording and 50 min 15 sec for every other recording for each set of receptions.

4.1.5 Calibration of Hydrophones and recordings during the PhilSea Experiment

Calibration of measurements made with NPAL recording is required keeping in mind the end goal to present results in terms of absolute acoustic pressure levels. These account for the responses of the hydrophone, the pre-amplifier (preamp), and the amplifiers, filter, and analog-to-digital converter (ADC) in the recording framework.
Calibration depends on the depth. But the values in the them do not change the spectral levels much, they are nearly equal.
The calibration measurements are done in the similar manner which was implemented by Wage in [20].

4.2 Observing of spectrogram of Hydrophone

Using the spectrogram function in MATLAB, we produce the spectrogram for a single hydrophone, which is the 5th hydrophone in this case. The spectrogram was produced using 3 sec snapshots, 50% overlapping, 3000 points FFT, and hanning window. The spectrogram computes the short-time Fourier transform and returns the spectrogram of the input signal vector. It plots the power density function of the segments of the input vector using surf function. The input for the spectrogram function is derived from the data from the 5th hydrophone, using a window of 1200 samples i.e. 1 h data on 197^{th} day 10^{th} hour 50 min 15 sec in the PhilSea10 data , 1500 over lapping segment, 3000 points FFT, and sampling frequency of 976.565 kHz. Fig below shows the spectrogram of the 5^{th} sensor in the array of 31 sensors.
We can notice in this picture that the intensity of the picked signals at the 5th phone is at the highest levels between 0-60 Hz and its start fading after that. There are few noises occurring at 140, 250, 330, 420 Hz respectively for the first half an hour (1800 sec) and eventually vanish in the other half an hour of data. This thesis is concentrated upon the 0-60 Hz where the spectrogram is pretty much constant over the time and has high intensity levels, this is due to the presence of the strum. The blue values represent the area where there are no signals to be picked because they are outside the range of the hydrophones linear array.

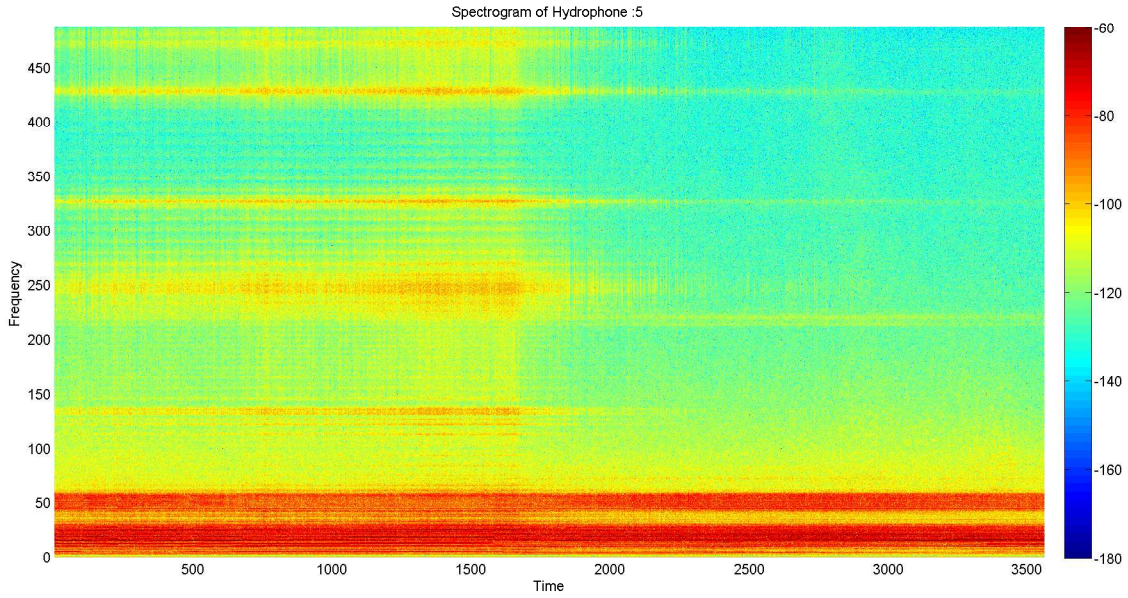

Figure 4.3: Spectrogram for 5th Hydrophone on the 197$^{\text{th}}$ day 10$^{\text{th}}$ Hour 50 min 15 sec in the Phil Sea10.

From the figure 4.3, it could be observed that the spectogram are just used for detecting the signal presence at particular time and frequency, but cannot be used for studying the characteristics of the signal such as its type, length, strength. So, for better understanding the characteristics of signals at each time over a range of frequencies, the spatial spectrum is used for identification as shown in the next section.

4.3 K-Omega Spectrum used for revealing the signals

The K omega spectra can be used for detection of various signals, sources and noise. The block diagram shown below explains how a frequency wave number spectrum is computed by the fast Fourier transform. It is a representation of power as function of frequency and angle.

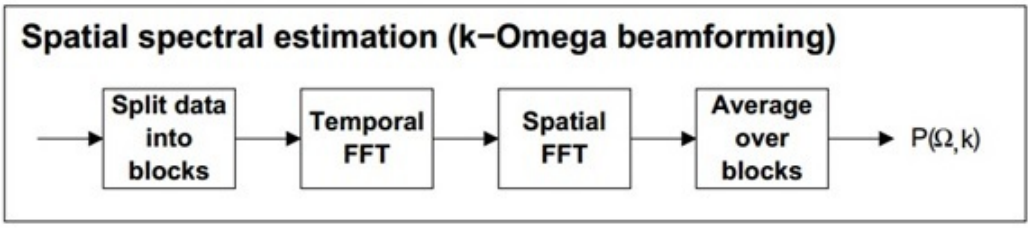

Figure 4.4: Block diagram of K- omega beamformer

The above figure shows the block diagram of Spatial spectrum estimation where 2D FFT is taken along time and spatial domains. The $P(\omega, k)$ denotes the representation as power as function of frequency and wave number.

4.3.1 Interpretation of frequency wave number spectrum

The K -Omega Spectrum is interpreted as non-propagating region (where non propagating waves such as cable strum vibrations effect the region) , Visible region (un aliased signals can be observed) and aliased region (beyond the nyquist sampling rate).

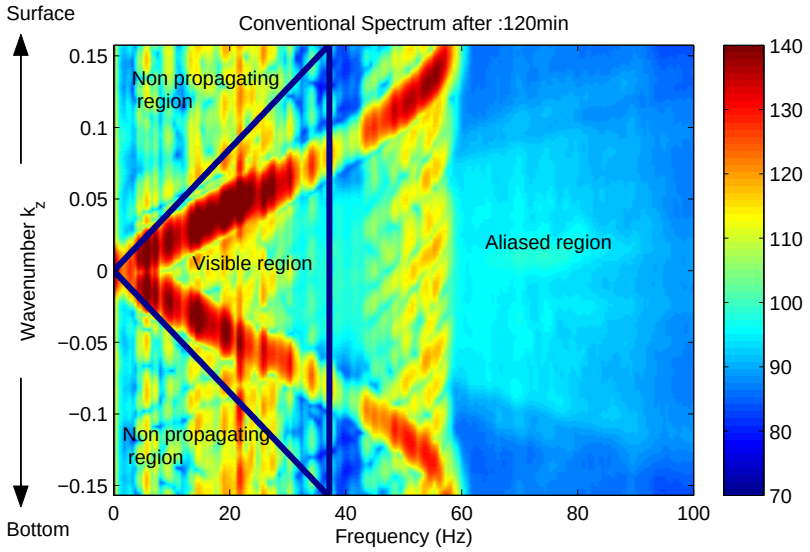

Figure 4.5: Interpreting frequency wave number spectrum at 120 min

The above diagram as labeled show where the various regions are observed in a K omega spectrum.

Here, the Nyquist sampling frequency is c/2d where c is velocity of sound and d is the distance between consecutive array elements in a linear array. In this thesis, the velocity of sound is taken as 1480 m/s (though the subarray is in SOFAR channel) and d = 20 m. So the maximum frequency for which the signal will unaliased is $\frac{1480}{2*20} = 37Hz$.

The visible region represents the area which is inside the triangle formed by blue lines, where as the aliased region occurs after the triangle. While the non propagating region is the oustide area of triangle which is less than 37 Hz. After 37 Hz, the signal becomes aliased. Hence, in this thesis signals beyond 37 Hz are not illustrated even though relevant results occur at those frequencies.

4.4 K-omega Spectra of Continuous set of receptions

As discussed earlier, this thesis highlights on the strum in the continuous set of data in PhilSea10. The strum is revealed by plotting K-omega spectrum (Conventional wave number frequency spectrum). The K omega Spectra in data set starts on 148^{th} day (55 Hrs long) with three different time durations.

The parameters used for plotting the 20 min K-omega Spectra are: 2 sec time block, hanning window

The above figures show the spectrum at a band below 100 Hz, which is lower than the

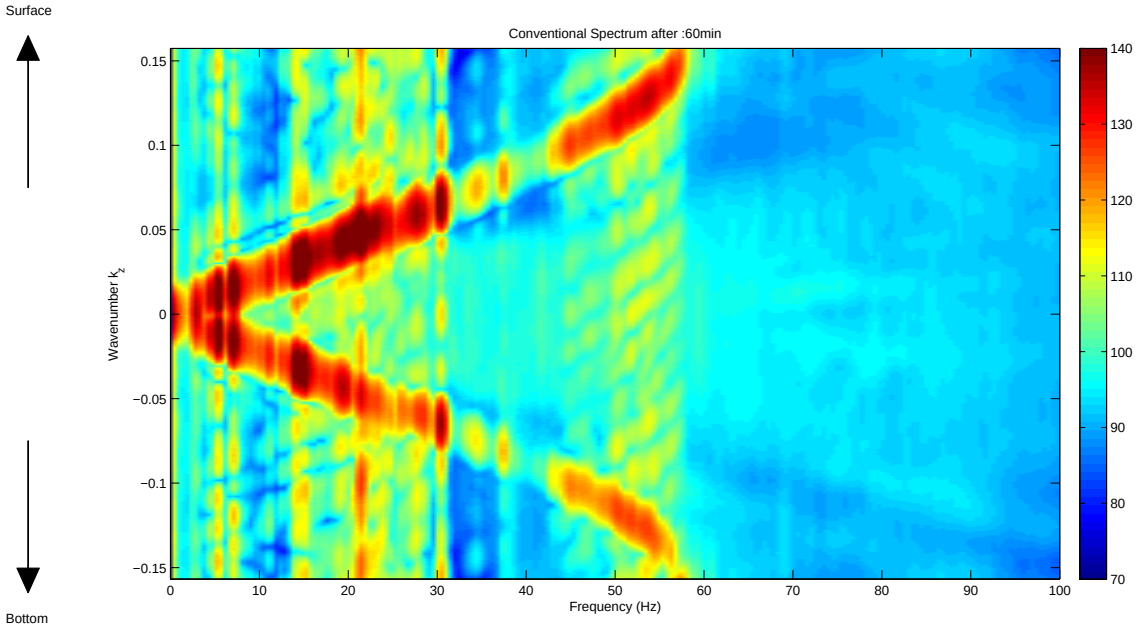

Figure 4.6: Relatively High strum content at 60 min in the data set

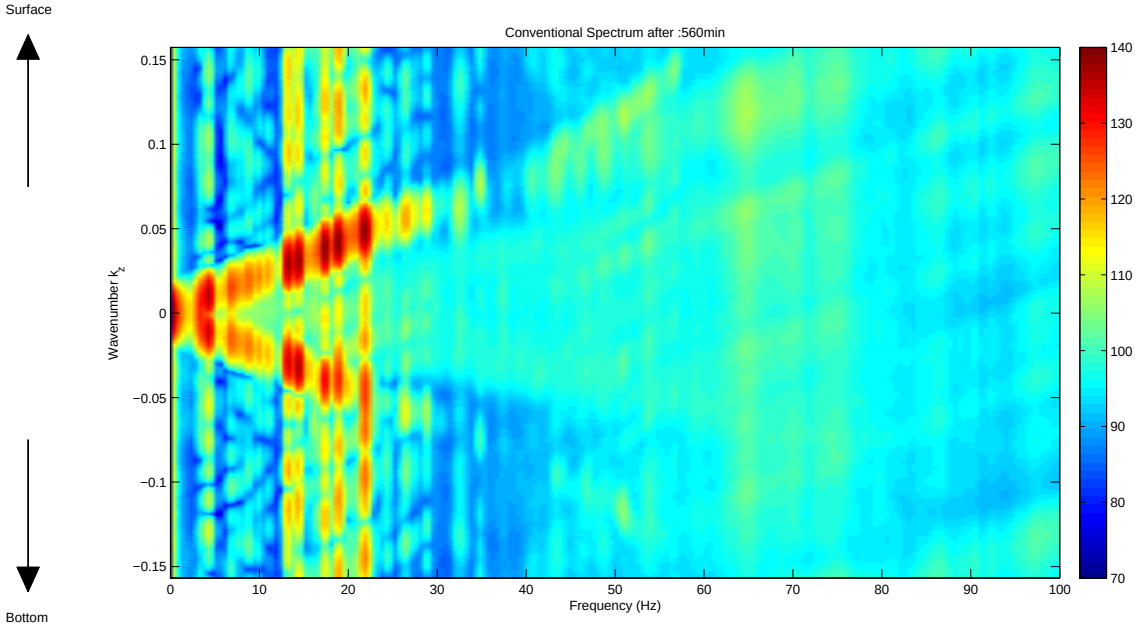

Figure 4.7: With Mediocre strum content at 560 min in the data set

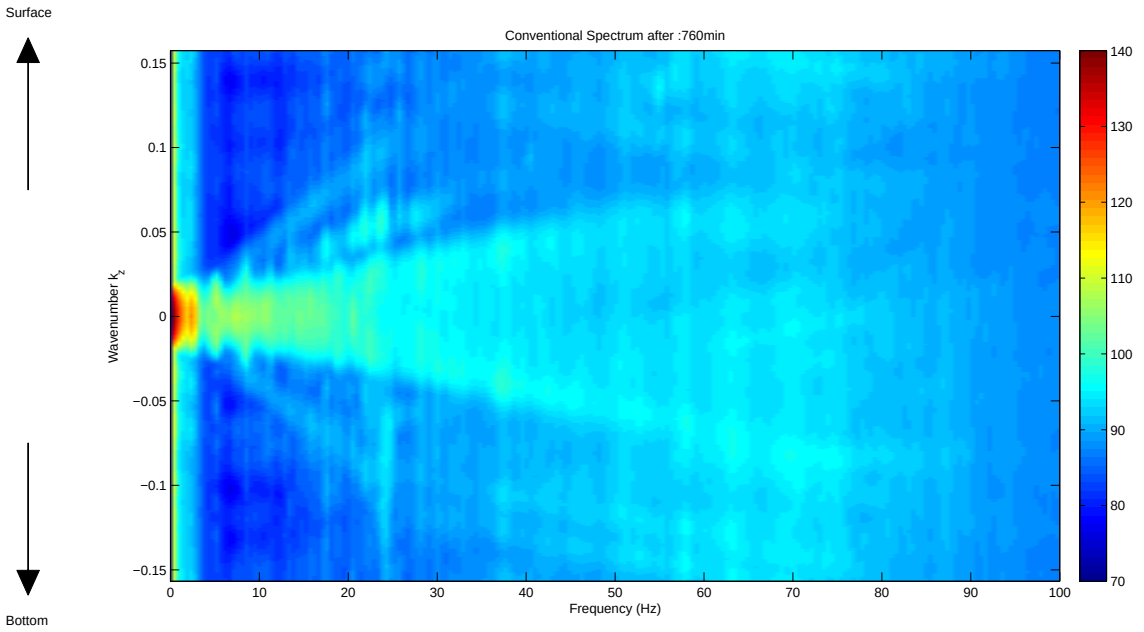

Figure 4.8: With No / less strum content at 760 min in the data set.

frequency of the sources deployed in the experiment. In this band much of the noise is concentrated in a cone of angles around broadside, which is typical for vertical arrays located near the sound channel axis [21].
In addition to the spatially-spread noise around broadside, Fig. 4.6 and 4.7 indicates the presence of two strong arrivals, one up-going and one down-going, for frequencies less than 60 Hz. These arrivals appear in most of the receptions and are attributed to mechanical vibrations of the array, i.e., cable strum. The strum is observed in between the frequencies of 0 and 60 Hz [7]. All the seven sets of continuous, K-omega spectra of strum are observed and the data set starting on 123rd day is not considered for this study. The K-omega spectra in the entire duration of 55hr on 123^{rd} day has no strum or less strum unlike other datasets which is similar to those as shown in figure 4.8.
In the K-omega Spectra at time 60 min (Figure 4.6) and 560 min (Figure 4.7), there seems to be presence of constant sources due to which the vertical lines occur over the frequency wave number spectrum in between 0 to 60 Hz. In figure 4.6, the strum disappears for a part of frequency ranging 30 to 43 Hz, and reappears after that.
So, from the observations of the K-omega Spectra at different time stamps, we conclude that the strum varies with both time and frequency.

4.5 Eigenvalues associated with the strum

Since, DMR is dependent on its eigenvalues, which help in tracking the DMR solution (Ensemble), it is important to observe the change of eigenvalues of the strum over the period of time and frequency.

Consider the dataset starting on the day of 143 lasting for 55 Hrs for Number of hydrophone elements 31 and snapshots, L = 1153 ,

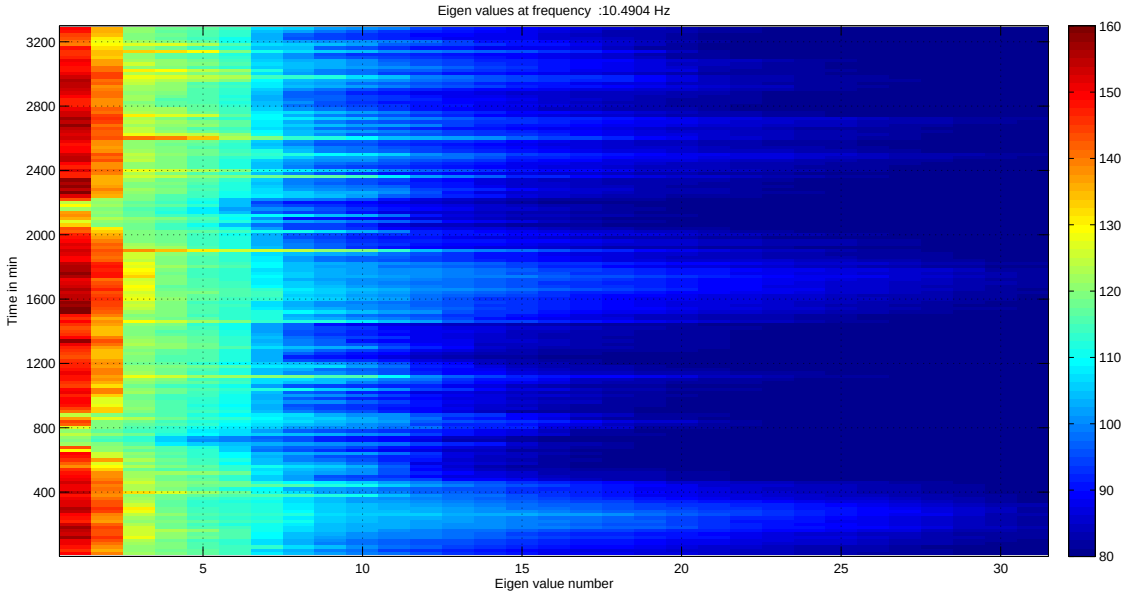

Figure 4.9: Eigenvalue spectra at 10 Hz

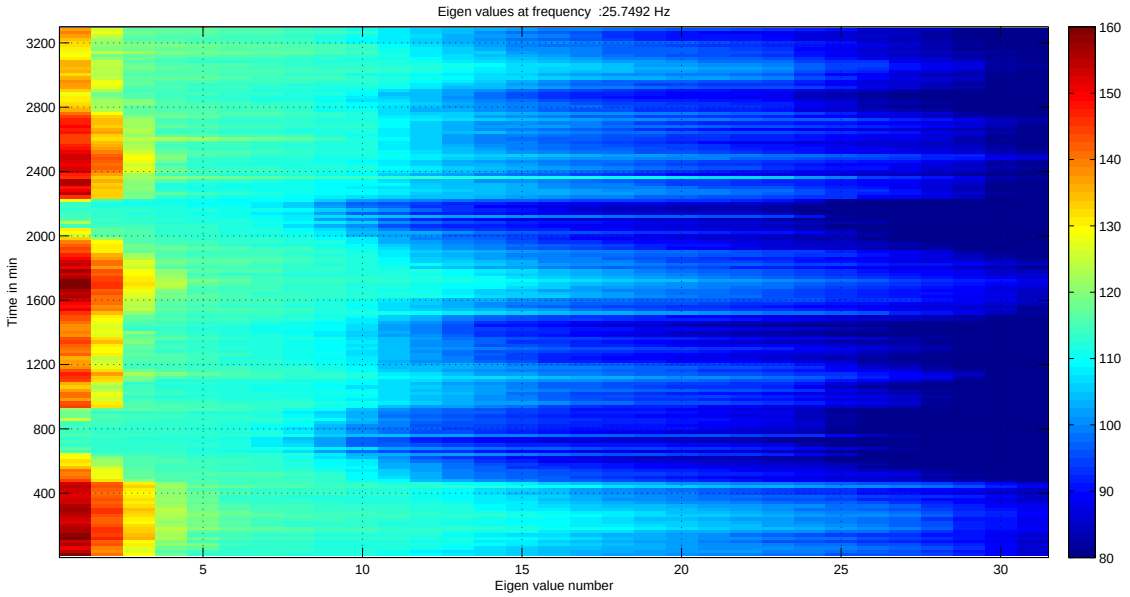

Figure 4.10: Eigenvalue spectra at 25 Hz

The above figures are plotted for whole 55 hrs of the data set (time) in Y-axis as function of a single frequency (10 Hz and 25 Hz in the figures 4.9 and 4.10 respectively) with

X- axis being the Eigen value number in dB scale. The first 2 Eigen values were dominant (as much as 30 dB above other eigenvalues).
From these Eigen value spectra, it is observed that the strum has quasi periodicity i.e., recurrence at irregular intervals of time. Moreover, the strum fades in and out in all frequencies over the period of time at same intervals, this can be linked to tidal variations. The fading in out is due to the fact that array revolves on the surface with one end fixed at the bottom (anchor).

4.6 Eigenvectors associated with the strum

The DMR beamformer depends more on eigenvectors rather than Eigen values, as these are centered at around optimal solution.
The output of a uniformly-weighted CBF with respect to the inputs of first five eigenvectors for the data set starting on 148^{th} day (55Hrs long) at 60 min and 560 min are shown below:

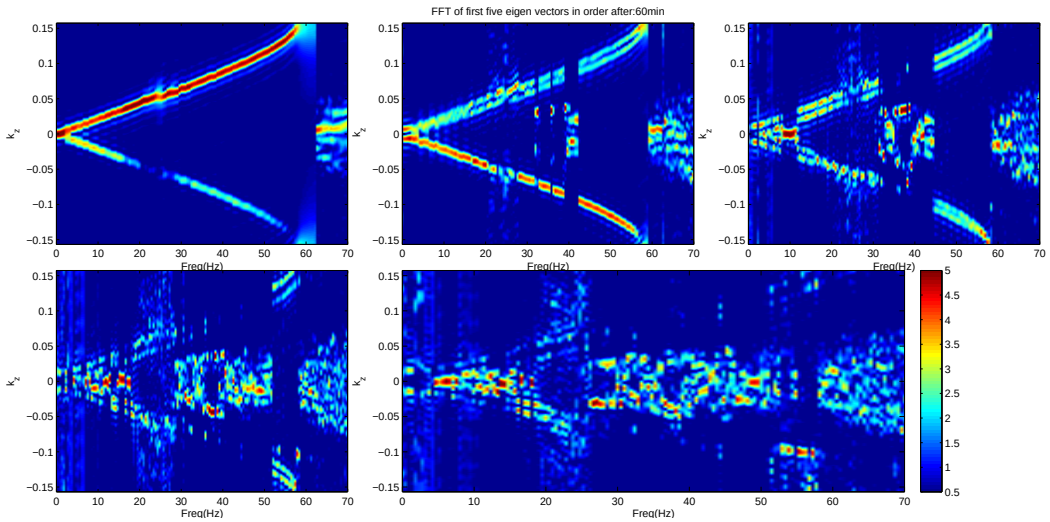

Figure 4.11: FFT of First five eigenvectors at 60 min

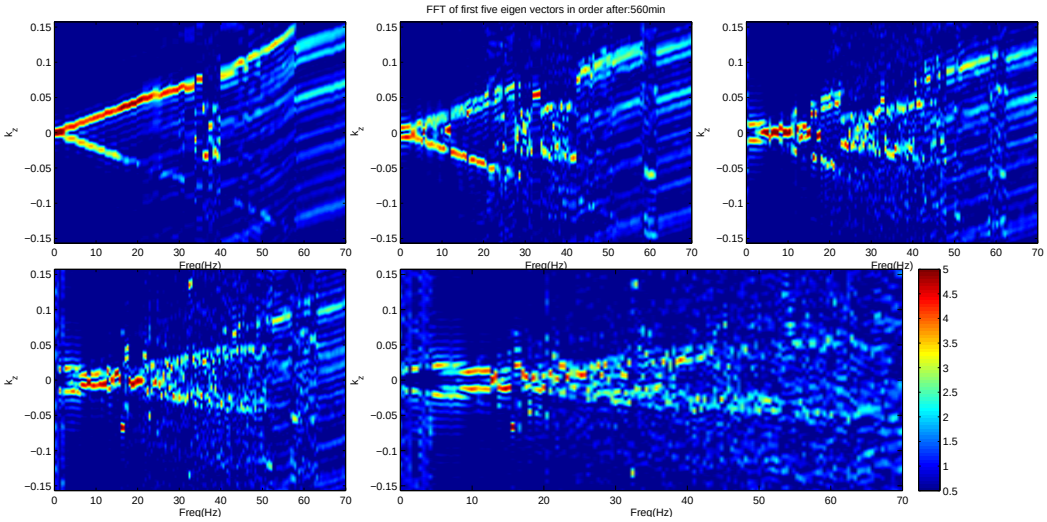

Figure 4.12: FFT of First five eigenvectors at 560 min

Figure 4.11 shows that the strum lies in a subspace defined by the first three eigenvectors of the SCM, which are associated with the three largest eigenvalues, while figure 4.12 shows that the strum lies in a subspace defined by the first two eigenvectors of the SCM, which are associated with the two largest eigenvalues. Below 60 Hz, the peak of the beam formed output for the first eigenvector usually occurs at an angle associated with the strum. In figure 4.7, for this reception, 40 Hz is an exception; at this frequency the dominant eigenvector is associated with the broadside noise instead of the strum. Above 60 Hz, the strum is significantly reduced, and the first eigenvector is always associated with a component of the broadside noise. The second sample eigenvector exhibits similar behavior as that of first; the peak in its CBF output typically occurs at the negative (downward going) of the wave number associated with the first eigenvector, while other eigenvectors contain the traces of both upward and downward arrivals with broad band noise being predominant in them. Thus, the strum can be replicated with the addition of its dominant eigenvectors at that particular frequency.

4.7 Selection of the constant Strum from the data

The continuous receptions files possess nearly constant strum with reference to the initial time (say 20 min here). The selection of constant strum data improves the experimental validation of DMR Beamformer notch depth using random matrix theory because for a nearly constant strum it is most likely to have same INR (interference to noise ratio) values. The procedure to pick up these reception files is as follows:

- The eigenvectors of the strum are found out using the eigen decomposition and are loaded for selection of constant strum files.
- Now, the first Eigen vector (for maximum number of snapshot found) is projected on the subspace S spanned by Eigen vectors, 1,2 and 3 (Depending on the highest rank

observed in the dataset). The subspace is an orthogonal basis formed by first three eigenvectors at the initial time, t (Say 20 min here).

- The projection of vector on to another vector is shown below: Consider two complex vectors a,b.Any of these vectors (say a) can be decomposed in to two parts. One part which is collinear to vector b is called as vector projection of a on to b and the other part, orthogonal to vector b is called as rejection vector of a on to b. Mathematically, the vector projection of a on to b can be shown as follows:

$$proj_b a = \frac{< a, b >}{< b, b >} b$$

where

$$< a, b >= b^H a$$

.

- The projection of first eigenvector onto S is the sum of the projections of first eigenvector onto the individual basis vectors (eigenvectors 1,2 and 3), a fact that depends critically on the basis vectors being orthogonal (all eigenvectors are orthonormal to each other).
- After finding the projection vector for the first eigenvector over a period of time on to subspace spanned by first three eigenvectors at t = 20 min(say), the squared norm of this projected vector is found out.
- The squared norm of vector a on to b is found as follows:

$$w_p(a, b) = ||proj_b a||^2 = \frac{| < a, b > |^2}{||b||^2}$$

- Lastly, Values of the squared norm having a threshold value > 0.9 for each frequency are picked over period of time and are classified as Constant Strum.

Selection of constant strum is required to group the files which have same INR for ND versus.L plots. Below figures are the plots of squared norm values over the data set beginning on 148^{th} day (55 Hrs) at frequencies 10 and 21.45 Hz.

As we observe, the squared norm values over time are not same across frequencies. Hence, it is necessary to pick constant strum files for each frequency too.

4.8 Selection of Wave number Kz values associated with the strum

To classify the signal as strum, the Kz values associated with it are to be picked up. The 2 possible ways of detecting the Kz values associated with the strum are described below.

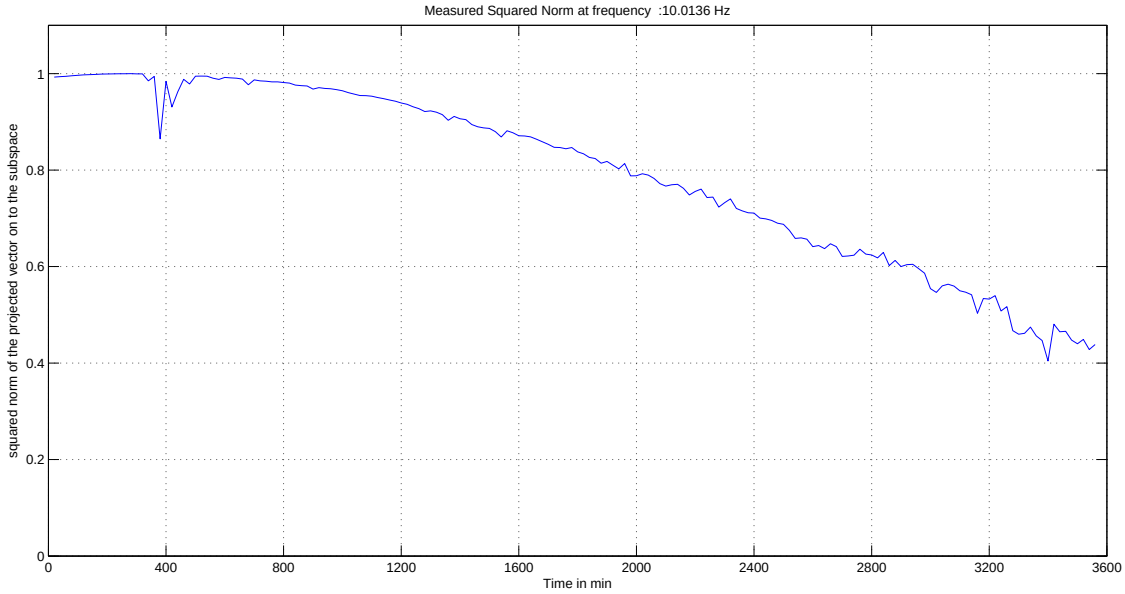

Figure 4.13: Measured squared norm against time at frequency 10 Hz

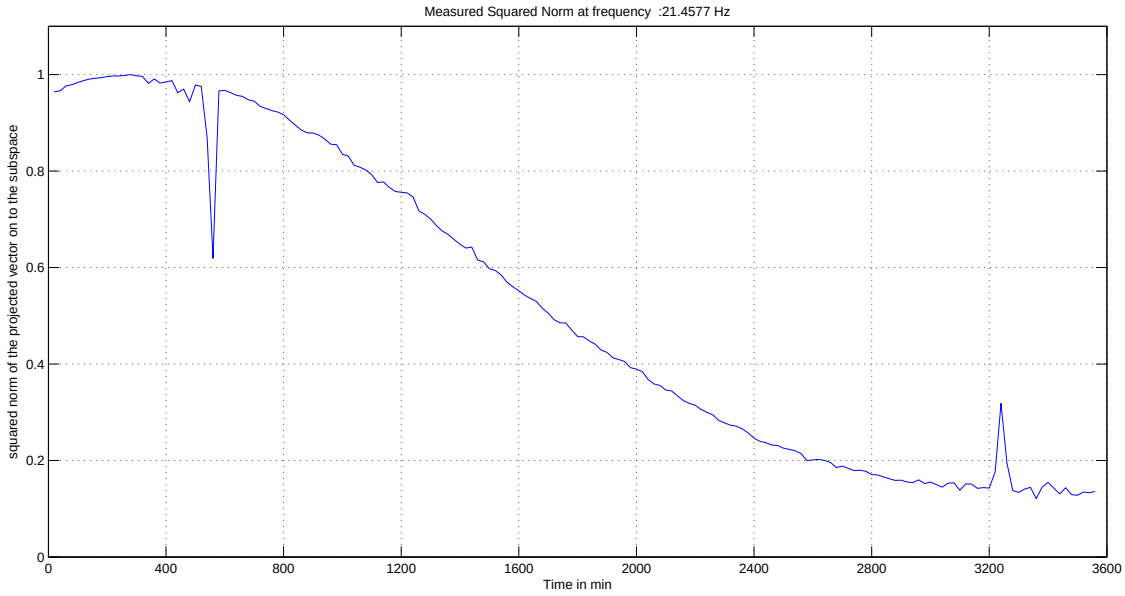

Figure 4.14: Measured squared norm against time at frequency 21.45 Hz

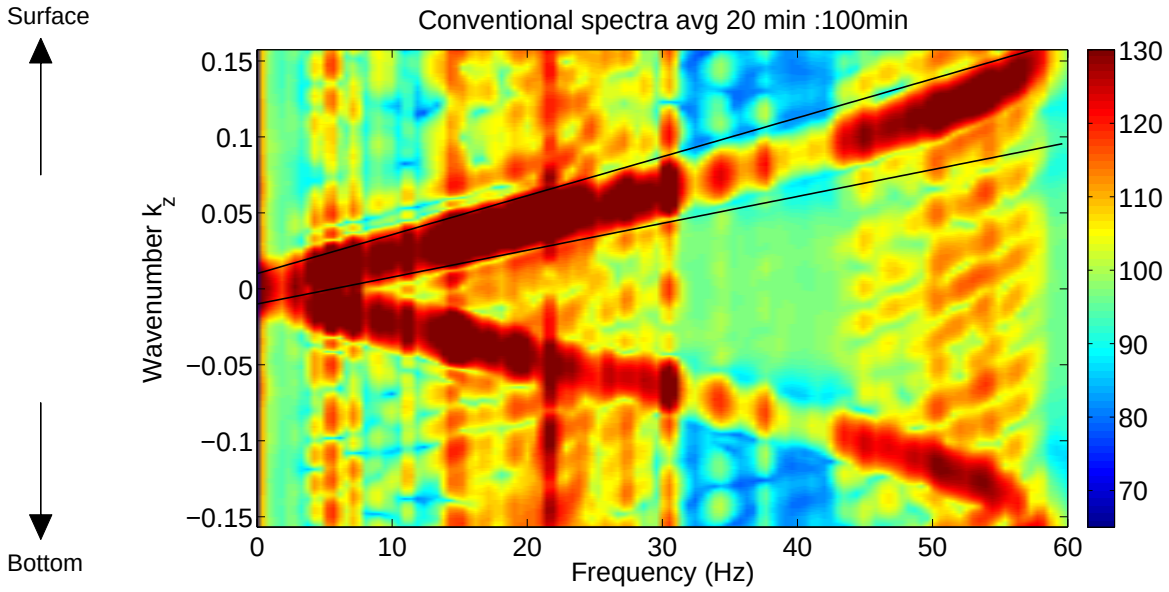

Figure 4.15: Kz values in between the slope values

One way is to find out the slope of the upward and downward arrivals, and if the Kz values lie in between them then it can be classified as strum which has been described in the following figure. The other way, which is more precise and which is used in this thesis to pick the peak Kz values is explained below.

- The Fast Fourier transform of eigenvectors along the length in space domain is processed.
- The zero crossing points in the spatial FFT points are found by $\pm 2\pi$/N*D of the maximum values picked (Here N is Number of spatial FFT points, d spacing between elements).
- The maximum value Kz lies in between the zero crossing spatial FFT bins.
- Fourier transform here is achieved by multiplying the replica vector, V (Spanned across the zero crossing points) with the eigenvector.
- The points at which the product of the replica vector V and Eigen vector are maximum , are the points which have maximum Kz value in between the zero crossings.

The peak /kz/ (say eveckz) values are stored for all the time duration files for each temporal frequency.

4.8.1 Snapshot Problem

Consider the hydrophone array data X as an M x N matrix where M is the amount of time (that we want to divide the data into) and N being the number of hydrophones (31 in this

case). In order to get sufficient time samples, we chop the time series received at each sensor into L blocks, and windows are applied to each block, where each block here is referred to as a snapshot. Then, the Short Time Fourier Transform / FFT is applied to each time block to obtain the frequency components, and the frequency samples of interest (at f) will be picked out to form the L temporal samples for each sensor. In this thesis, hanning window is selected with 50 percent overlapping and block length of 2 sec, for frequencies ranging from 0 Hz to 60 Hz (Where strum is predominantly present).
Short-Time Fourier Transform:
Suppose x(t) is the time domain signal, then the Short-Time Fourier Transform is defined as:

$$X(t,\omega) = \int_{t}^{t+T} g(\tau - t)x(\tau)e^{-j\omega\tau}\ d\tau$$

Where g(t) is a short time window function.
The Problem:
The maximum number of blocks/snapshots L that are obtained after chopping the given time series (say 20 min) in to blocks of length say 2sec (2048 to be accurate) are calculated. In general, there is a requirement of higher number of Monte Carlo trails and snapshots. The Monte Carlo trials (in the case of constant strum) are the number of files we get after dividing the continuous set in to reception length that we wish to consider.
For example, consider a 10 hour continuous data set, and then it turns out to be (for 2 sec block length) that the number of snaphots available depends on the length of reception chosen as shown in table 4.4.

Table 4.4: Number of Monte Carlo trails and snapshots available for a reception length.

Continuous reception length chosen	Number of Monte Carlo Trials	Number of Snapshots available
1 Hour	10	3601
30 min	20	1733
20 min	30	1153
10 min	60	599

As observed in the table shown above, If there is requirement of higher number of Monte Carlo trails in the data set, then lower number of snapshots are obtained and vice versa. Hence, there is a trade of between the Monte Carlo Trails and snapshots depending on the split of continuous receptions.
The Ideal requirement would be to get both higher numbers of snapshots as well as Monte Carlo trails. Hence, number of Monte Carlo trails and snapshots need to be balanced to get accurate results.

4.8.2 Estimation of Subspace Rank

As the exact values of d for each frequency and time in the Philippines sea data set are not known ,the rank is tried to be estimated by using the Eigen values at first and then

with Eigen vectors and compare them and choose the method which ever gives the best estimation.
In these estimation techniques, a set of values of d ranging from 0 to 3 is considered after the observation of their respective K omega spectrum of their FFT of Eigen vectors. The spatial Spectrum of the FFT of Eigen vectors helps us to determine the maximum value of d that can be used.
The maximum value of d for each data set is determined as shown below by their FFT of Eigen vectors which are computed by taking 20 minutes of each continuous reception:

1. For the first data set, which is considered to have low or no strum in it and it start day is 123.

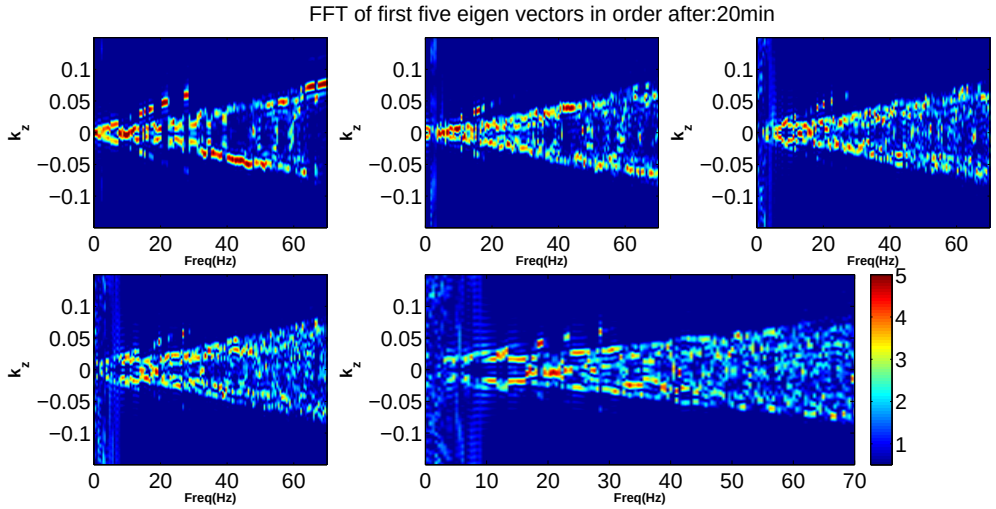

Figure 4.16: FFT of First five eigenvectors in the first data set

   As the data set does not have strum after 15 Hz, this data set is more or less significant to consider for validation. But, by observing the FFT of Eigen vectors we can assume d equals to 2.

2. Second data set whose start date is 130th day have 10 h long receptions. This data set has more or less constant strum data which can be used for computation.

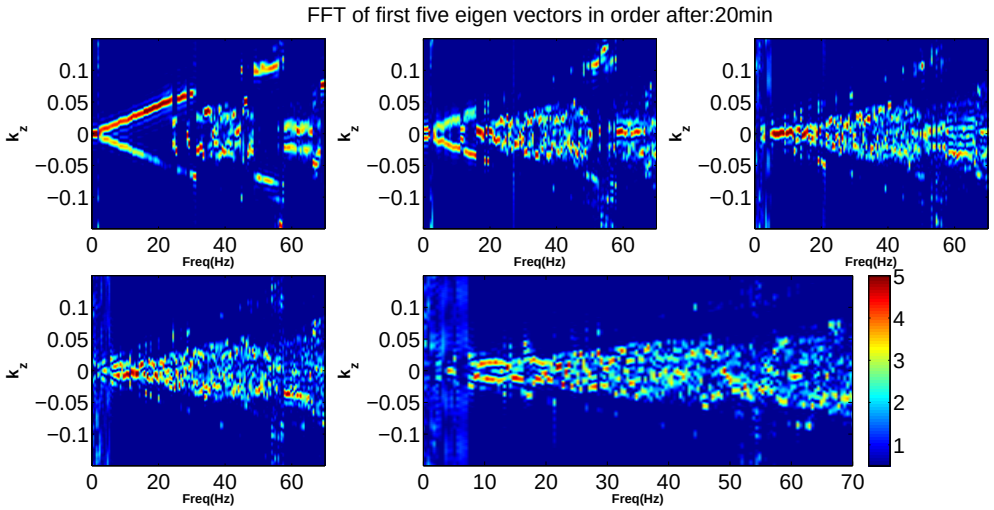

Figure 4.17: FFT of First five eigenvectors in the second data set

FFT of first five Eigen Vectors are as shown above. By observation, we can say that for this data set, at max d= 2 , there are two Eigen vectors that can be used to replicate the strum.

3. The third data set starting on 143rd day and is 55 h long is a mediocre one. The FFT of their Eigen vectors are as shown below :

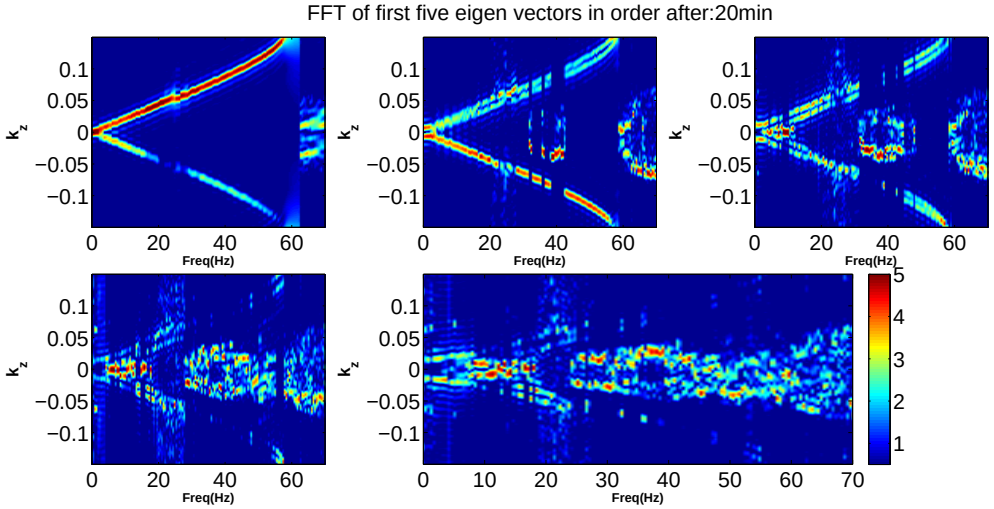

Figure 4.18: FFT of First five eigenvectors in the third data set

FFT of first five eigenvectors are as shown above. By observation, we can say that for this data set, at max d= 3, as there are three eigenvectors that can be used to replicate the strum.

4. For the fourth Data set, which starts on 190th day and lasts for 12 h has few hours of constant strum in it. Their FFT of First five eigenvectors are as shown below:

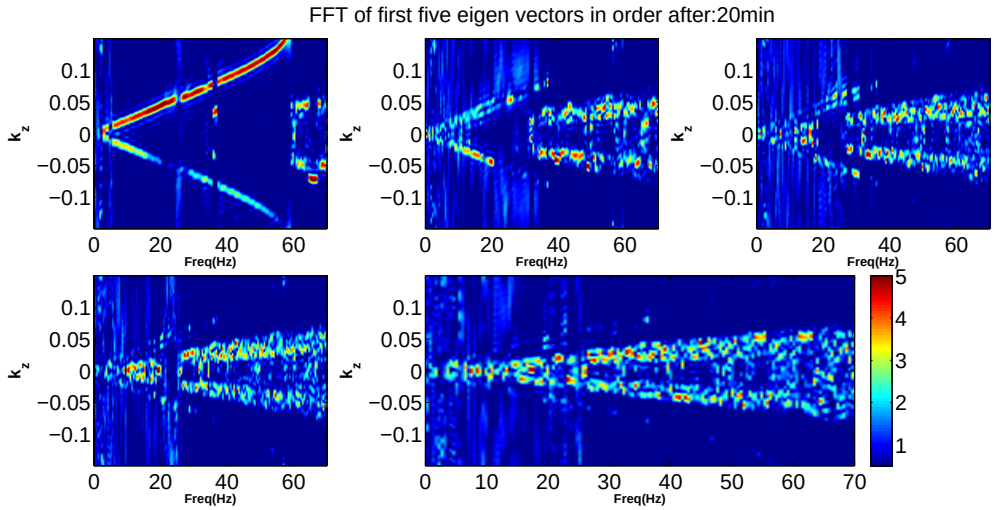

Figure 4.19: FFT of First five eigenvectors in the fourth data set

By observation, we can say that for this data set, at max d= 2, there are only two eigenvectors that can be used to replicate the strum.

5. For the fifth Data set, which starts on 191st day and lasts for 12 h has few hours of constant strum in it. Their FFT of First five Eigen vectors are as shown below:

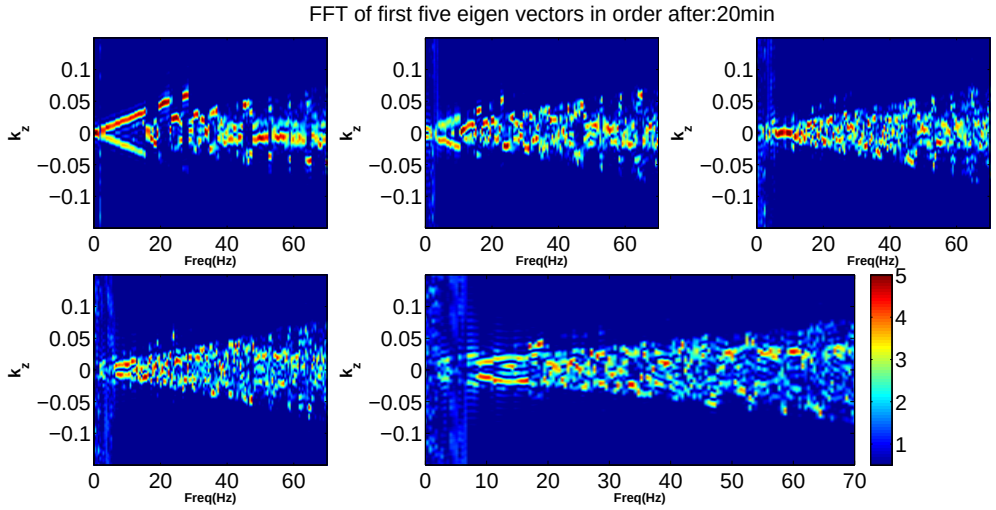

Figure 4.20: FFT of First five eigenvectors in the fifth data set

By observation, we can say that for this data set, at max d= 2, there are only two eigenvectors that can be used to replicate the strum.

6. For the sixth Data set, which starts on 192nd day and lasts for 35 h has few hours of constant strum in it. Their FFT of First five eigenvectors are as shown below:

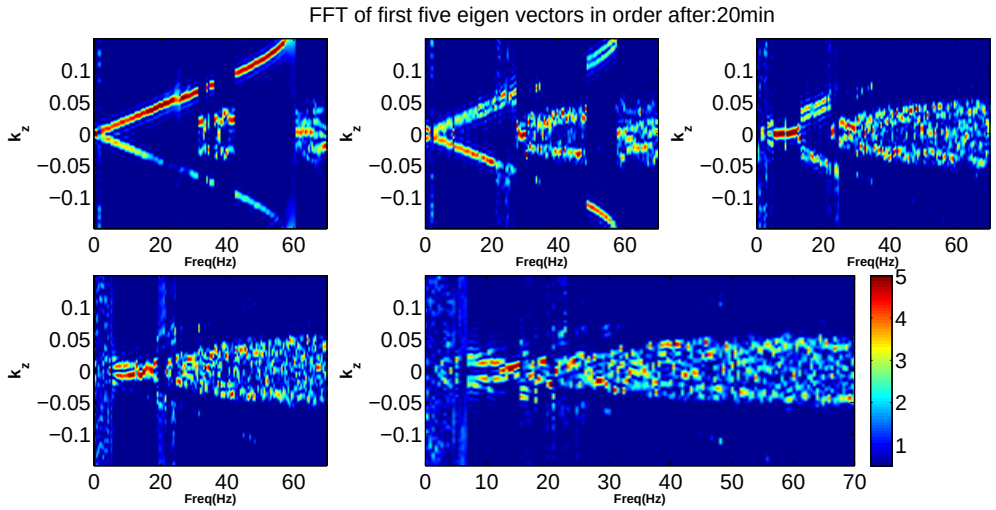

Figure 4.21: FFT of First five eigenvectors in the sixth data set

By observation, we can say that for this data set, at max d= 3, there are approximately three eigenvectors that can be used to replicate the strum.

7. For the seventh Data set, which starts on 198th day and lasts for 60 h has few hours of constant strum in it. Their FFT of First five eigenvectors are as shown below:

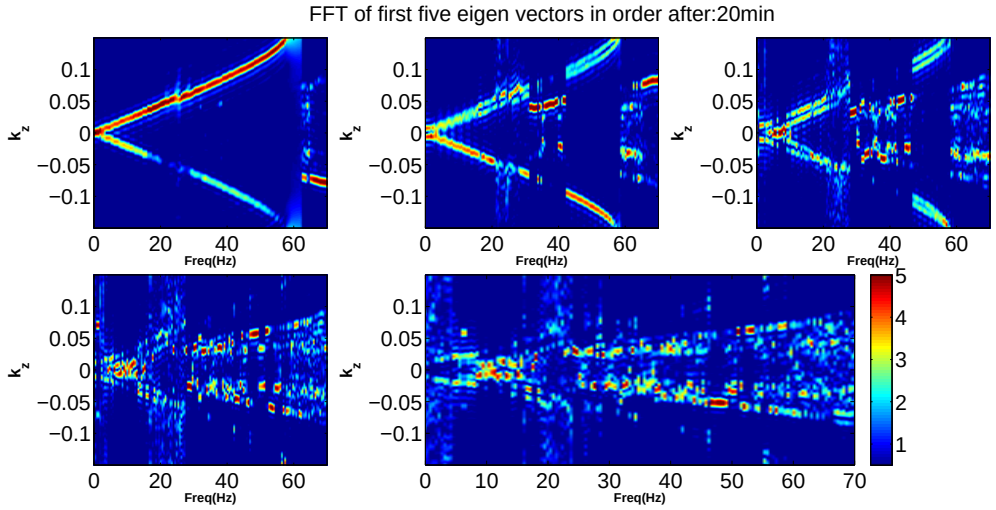

Figure 4.22: FFT of First five eigenvectors in the seventh data set

By observation, we can say that for this data set, at max d= 3, there are approximately three eigenvectors that can be used to replicate the strum. All the other eigenvectors do contain strum, but noise is more than domain than the strum.

Estimation of Subspace Rank using eigenvalues

The most commonly used methods are AIC and MDL criterion, the other one being the RMT based rank estimator. These models are used in context of estimating the smallest signal subspace model that accounts the data. The signal subspace refers to the smallest number of eigenvectors that explains the correlation between the hydrophone array elements.

Akaike Information Criterion AIC is an asymptotic approximation, first introduced by Akaike in 1973. The AIC has been derived from the KullbackLeibler information concept. Later, AIC has been improved by various authors; one such is by Wax and Kailath which has been considered here. The smaller AIC value, the greater generalizability of the model. The model with smallest AIC is the best, among a set of competing d values ranging from 0 to 3 depending on the data set used [2].
The Smallest value of the signal subspace i.e., number of eigenvalues that minimizes the AIC criterion is picked at particular frequency for that time period. The AIC criterion as suggested by wax and Kailath is shown below:

$$t_d = \frac{\prod_{i=d+1}^{N} \widehat{\gamma}_i^{\frac{1}{N-d}}}{\frac{1}{N-d}\sum_{i=d+1}^{N} \widehat{\gamma}_i} \tag{4.1}$$

where

$$\widehat{D}_{AIC} = \underset{d}{\operatorname{argmin}} \{(-2(N-d)L\log(t_d) + 2d(2N-d)\} \tag{4.2}$$

where

$$0 \leq d < N$$

.

Minimum Description Length Criterion First introduced by Rissanen in 1996, MDL has been derived from a Bayesian approach. Here we consider the improved method as suggested by Wax and Kailath [2]. The MDL criterion as suggested by wax and Kailath is shown below :

$$\widehat{D}_{MDL} = \underset{d}{\operatorname{argmin}} \left\{ -(N-d)L\log(t_d) + \frac{d(2N-d)}{2}\log(L) \right\} \tag{4.3}$$

The value of td is same as mentioned in the AIC criterion. By withdrawing from various roots, they have wound up in fundamentally the same structures, they are also referred to as maximum penalized likelihood methods, for which a compensation or penalization term is subtracted from the likelihood function of the parameters to be evaluated. Both criteria include the log likelihood of the observed data, which reduces to a statistical figure i.e., the ratio of the geometric mean to the arithmetic mean for the smallest N d eigenvalues of the SCM. These criteria is arrived from the assumption that the eigenvalues of the noise subspace i.e. the N-d values are roughly the same. When a series of values are approximately equal, their geometric mean and arithmetic mean are also equal.

RMT Based Rank Estimator The rank estimation algorithm specified in the past section is one of a few latest results from a subject differently known as infinite random matrix theory (IRMT) or stochastic Eigen-analysis. IRMT gives results on the distributions of eigenvalues and eigenvectors of random matrices which has flexible cutoff as the matrix becomes infinitely large, but the ratio of rows to columns converges to a fixed constant [2]. In array processing, these outcomes give asymptotic expressions for the SCM eigenvalues as the number of sensors and snapshots both become infinite, in such a way that the ratio of sensors to snapshots called as the aspect ratio c is fixed. These expressions for the eigenvalue distributions shape the premise for the rank estimator which was created by Nadakuditi and Edelman [2].
Nadakuditi and Edelman have developed these expressions by utilizing the results from IRMT. IRMT predicts the distribution of the sample covariance matrix eigenvalues in the noise-only case (D = 0). As indicated by theory the distribution depends on the ratio of sensors (N) to snapshots (L): c = N/L. The prediction is valid in the limit as N,L with c fixed. Utilizing the anticipated eigenvalue measurements in conjunction with the Akaike Information Criterion (AIC), Nadakuditi and Edelman (N/E) recommended the following estimator.

$$\widehat{D}_{N/E} = \underset{d}{\operatorname{argmin}} \left\{ \frac{{t_d}^2}{2c^2} + 2(d+1) \right\} \tag{4.4}$$

$$t_d = N\big[(N-d)\frac{\sum_{i=d+1}^{N} \widehat{\gamma}_i^2}{\sum_{i=d+1}^{N} \widehat{\gamma}_i}^2 - (1+c)\big] \tag{4.5}$$

Estimating Rank using Eigenvectors: Strum detector technique

This method of strum detection is proposed by Wage and Buck [7]. Firstly, the maximum values of wave number Kz for each temporal frequency (say 1050 Hz) for all the files and for eigenvectors are identified whose eigenvalues are dominant.
The peak Kz values are found out in same method as mentioned above procedure for selection of wave number Kz associated with the strum. The peak $|kz|$ (say eveckz) values are stored for all the time duration files for each temporal frequency. The next step in this rank estimation is the sketching of Histogram of the estimated peak /kz/ values, this is done as follows:
Firstly, the peak $|kz|$ (eveckz) values are loaded and zero crossings i.e $\pm 2\pi$/N*D (where N is number of array elements and d is equal to array spacing) are found. Now, the maximum values of histogram of eveckz for each frequency and specified bins (for histogram below bins considered are $-.002 : .0002 : .15$) are found. The bins are arranged according to the occurrence of maximum values of eveckz. The strum (main lobe) lies in between $\pm\pi$/N*D of the peak values of $|kz|$.

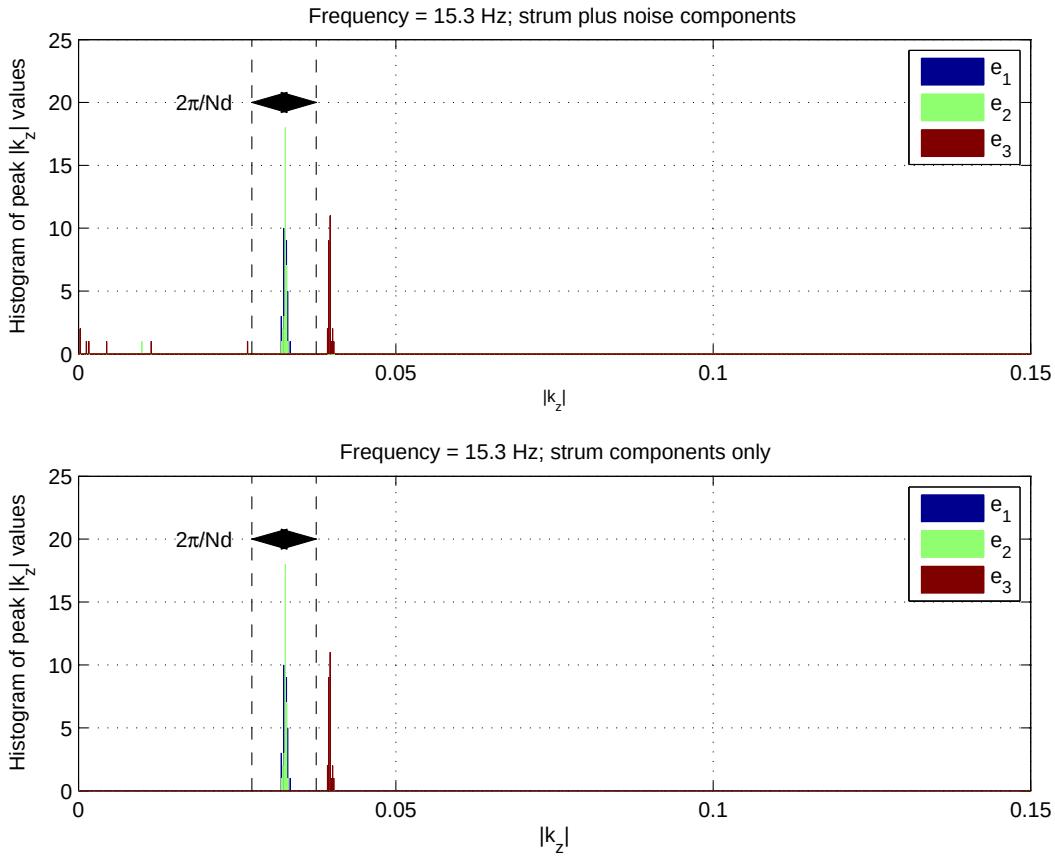

Figure 4.23: histograms indicating peak $|kz|$ values for the first three sample eigenvectors for the frequency 15.3 Hz

The First subplot in figure 4.23 is the Histogram of peak $|kz|$ values where it contains both strum and noise while the second histogram contains only the components associated with the strum where the noise components are eliminated. Most of the data clusters around $|kz| = 0.03$, the wave number associated with the strum component. The peak $|kz|$ value is used to determine whether the eigenvector represents strum. The eigenvectors with peak $|kz|$ values close enough (as defined by main lobe of the array) to the strum wave number are classified as strum.

4.8.3 Summary

The PhilSea10 dataset contains a year long data (discrete and continuous) which could be used for analyzing the strum and compare measured DMR notch depths with the new RMT model developed by wage and buck. In this work, through the experimental validation of DMR notch depth using Random matrix theory as proposed by wage and buck[7], the strum was analyzed for discrete set of receptions. The thesis is concentrated on continuous set of receptions in Phil Sea. The same set of calibration of measurements with recording systems during PhilSea09 is used for PhilSea10 (Both for Continuous and Discrete set of receptions) which was written by Prof.Kathleen Wage. The Frequency wave number

Spectra which was observed for all the data sets revealed that the data set beginning on 128^{th} day (55 Hrs long) contains less or no strum and therefore that particular data is not taken in to account for computations. The eigenvalue spectra which are observed over the data set for each frequency reveal that strum is quasi periodic in nature and the first two eigenvalues associated with the strum are 30 dB more than the other eigenvalues and these are approximately equal during strong events. While Observing the FFT of eigenvectors, It is observed that the first eigenvector is always associated with the strum having positive Kz values (Upward arrival) while the second eigenvector has negative Kz values (downward going) and other eigenvectors have traces of both. The constant strum is picked up from the set of continuous set of receptions by selecting a threshold of 0.9 (90 percent constant) of the measured squared norm value of the first eigenvector projected on to the subspace spanned by first three eigenvectors at reference time value (20 min). The Squared norm changes for each frequency, hence constant strum files are not the same for all frequencies. The constant strum picked up is used for further computation of results as explained in chapter 5. Considering the tradeoff between the number of Monte Carlo Trails and number of snapshots, a mid value of 20 min is chosen for further computations to balance the Monte Carlo trails and number of snapshots. Estimation of rank is important aspect as it classifies the DMR as single or multi interferers case. Using various rank estimation techniques, the rank of DMR is computed and validation using these rank estimation techniques is done and best rank estimation is being implemented (in chapter 5).

Chapter 5: Analysis for Validation of DMR Notch depth in PhilSea10

Chapter 5 presents the comparison of empirical results of DMR Beamformer notch depth vs. snapshots and notch depth vs. INR for the strum with respect to predicted values using the RMT model in the Philippines sea experiment 10. Firstly, a comparison of rank estimation technique is done on the data set to know which one works well. Then, an analysis for validation of RMT model for DMR notch depth has been presented in the case of discrete set of receptions. After which, an analysis for validation of RMT model for DMR ND is been implemented in continuous/longer receptions by dividing them in to smaller segments. In the validation failure cases, again a comparison of rank estimation techniques is done to check for a better rank estimation technique. Finally, the insights for a failure of validation of RMT model for DMR ND and its alternate ways of implementing them in PhilSea 10 are established.

5.1 Processing parameters

The processing parameters used for real data in this chapter are number of sensors, N=31, D = 2 in the discrete set of receptions, and D = 3 for continuous set. The rank of these receptions initially is selected by observing the overall FFT of eigenvectors spectrum in these receptions. The speed of sound in water is considered to be a constant at 1480 m/s even though the region is considered to be in SOFAR channel. The distance between two sensors is 20 m as the bottom half of the subarray 1 is considered. The sampling frequency is 976.5625 Hz. A 50 % overlap and hanning window is used for all the receptions which includes the continuous one too. Hanning window is chosen as it gives smaller main lobe width and suppresses the side lobe levels rapidly. The block length is chosen as 1 sec (0.968 ms) for discrete set of receptions and 2 sec (0.968*2) for continuous receptions. This is because in continuous /longer receptions the snapshots are more, so block length can be increased to have a better resolution. The number of temporal and spatial FFT points in longer receptions are chosen as 2048 while in discrete case it is 1024.
Frequencies between 10 Hz to 60 Hz are considered for the analysis i.e. the region where the strum signal spans between these frequencies. Different subsets of snapshots are considered for the analysis, L = 3 6 15 31 62 155 310... maximum available snapshots. The maximum snapshots that are available for the discrete set is 310 as they are 155 sec long where as for longer receptions it is 599, 1153, 1733 (see Table 4.4) depending on the split of receptions chosen. The maximum number of snapshots are chosen as the ground truth or the ensemble case for the analysis.

5.2 Comparison of Rank Estimation techniques

The rank is estimated for each temporal frequency and time duration file as the sum of the number of eigenvectors containing in strum (i.e in the main lobe of the array).
The rank estimation of DMR Beamformer plays a major role in the analysis. Lets consider the constant strum picked for each 20 min reception(split chosen) from the data starting on 143rd day and estimate the rank of DMR using N/E AIC, RMT and strum detector technique(picking peak 'Kz' values).

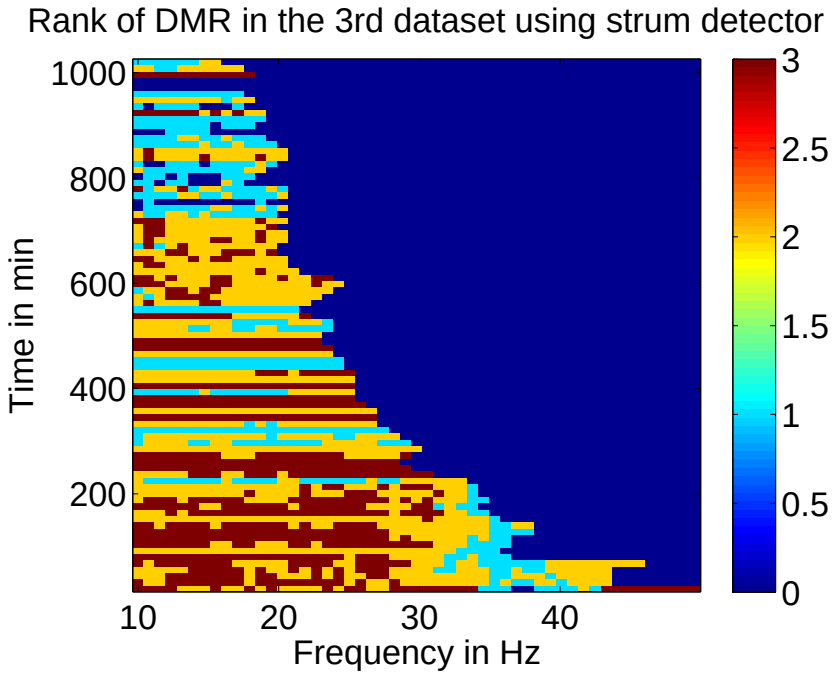

Figure 5.1: Rank Estimation using strum detector technique in the constant strum data starting 143rd day, where the red color indicates rank 3, similarly yellow rank 2, cerulean rank 1 and blue for rank 0

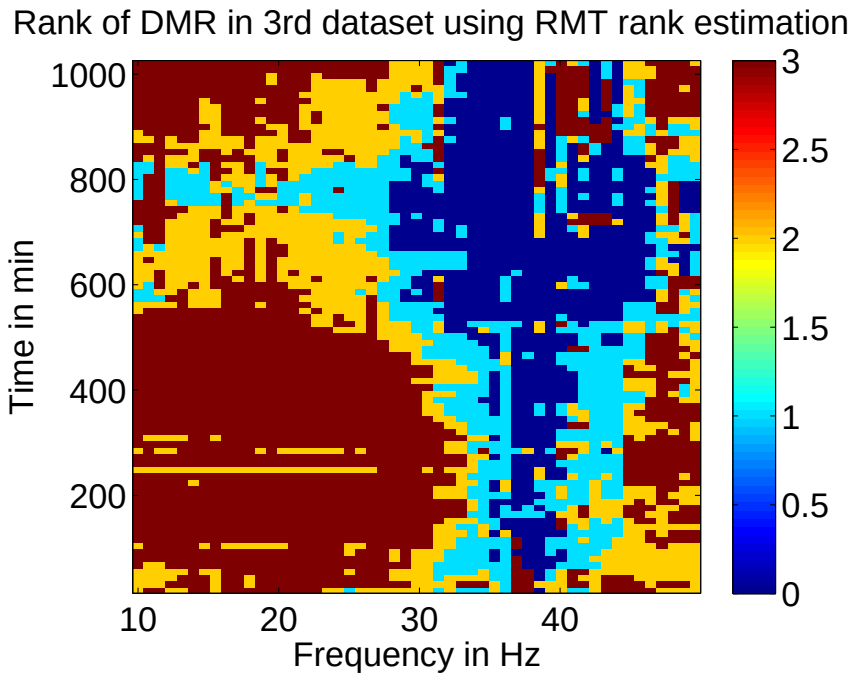

Figure 5.2: Rank Estimation using RMT technique in the constant strum data starting 143rd day, where the red color indicates rank 3, similarly yellow rank 2, cerulean rank 1 and blue for rank 0

Rank estimated by strum detector technique is as shown in figure 5.1 while using RMT technique is shown in figure 5.2. As it can be observed from the figures, that there is a significant difference in rank estimated by RMT and the strum detector techniques. While the rank estimated by N/E AIC and MDL is 3 for the highest available snapshot number. The rank estimated by N/E AIC and MDL vary for a fewer snapshot numbers but for higher snapshots number it is almost the same. Now, lets analyze the validation of DMR ND with its RMT predictions of ND vs. L using all the four rank estimation techniques.
Consider a 20 min constant strum reception at 27.2 Hz. From the figures 5.1 and 5.2, it can be observed that the RMT has more rank 3 estimations while the strum detector technique has a mix of of all the rank estimations from 3 to 0. Where as the N/E AIC and MDL has a rank estimation of 3.

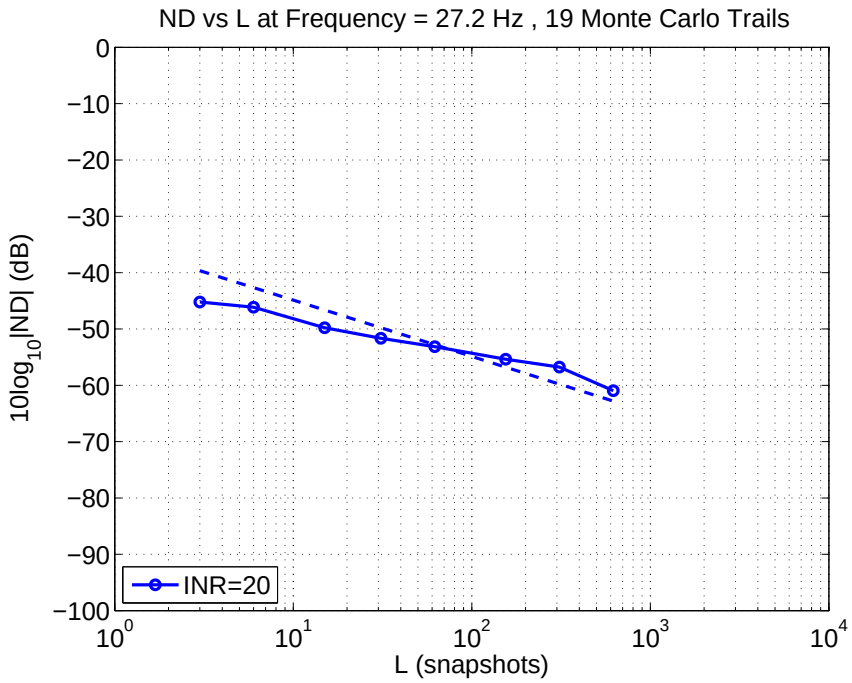

Figure 5.3: Comparison of predicted and estimated ND vs. L for a 20 min (constant strum) using strum detector rank estimation technique at 27.2 Hz frequency

Now, the same computation is followed using AIC,MDL and RMT rank estimation techniques [2] :

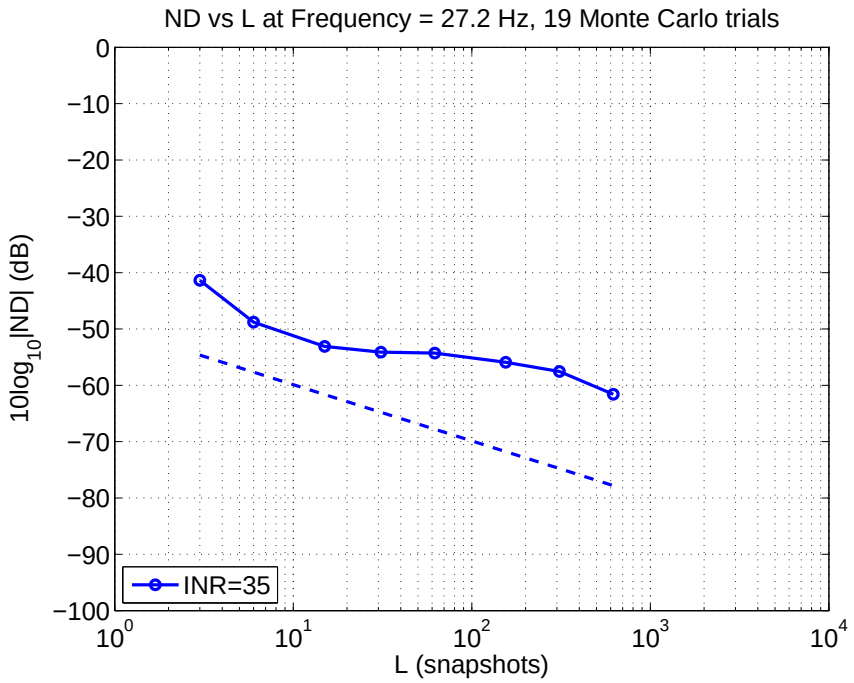

Figure 5.4: Comparison of predicted and estimated ND vs. L for a 20 min (constant strum) using AIC,MDL rank estimation techniques at 27.2 Hz frequency

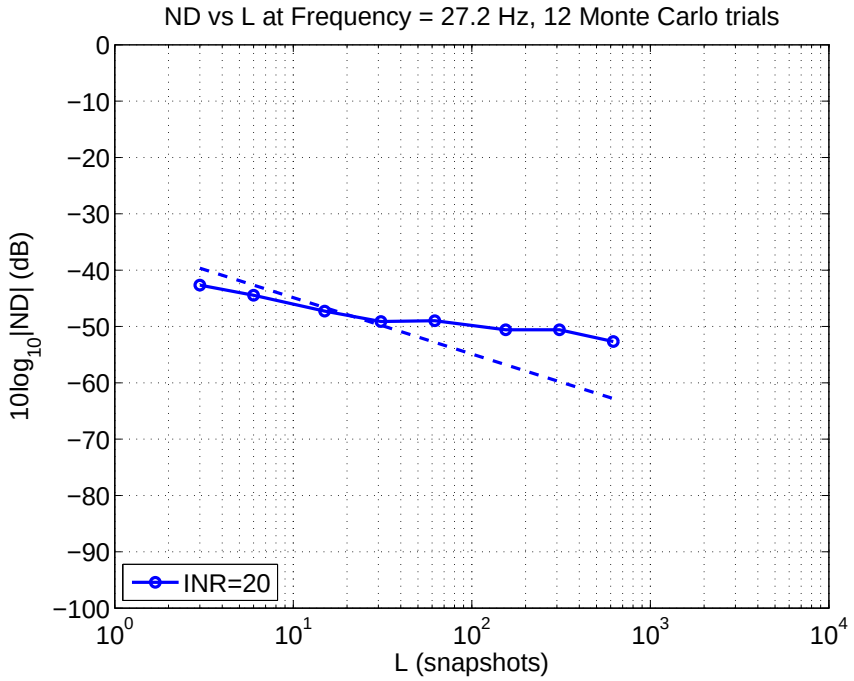

Figure 5.5: Comparison of predicted and estimated ND vs. L for a 20 min (constant strum) using RMT rank estimation techniques at 27.2 Hz frequency

As, it can observed in Figure 5.3 that the strum detector performs better than the rest

three. The N/E AIC and MDL rank estimation techniques have the same effect on the validation plot as the rank estimated by them in this case is same and fare poorly in validating the predictions that are as shown in figure 5.4. While observing Figure 5.5, the validation of measured ND vs.L using RMT rank estimation performs better when the snapshot number are less in this case and deviates from the predicted values as it approaches at higher snapshot number. The measured ND vs. L yields a mean slope of -6.46 dB/dec for figure 5.3 and -6.9 dB/dec for figures 5.4 and 5.5 at frequency 27.2 Hz.

Overall, the strum detector technique fares better than the RMT, N/E AIC and MDL techniques. There are few exceptional cases where the strum detector technique fails. This is discussed in section 5.7. In most cases, the strum detector technique predicts well than the rest three. Hence the further analysis is done using the strum detector technique.

5.3 Experimental validation of DMR Notch depth in discrete set of receptions

The DMR Notch depth analysis in discrete set of receptions of PhilSea10 has been shown in the below block diagram figure 5.6 [7].

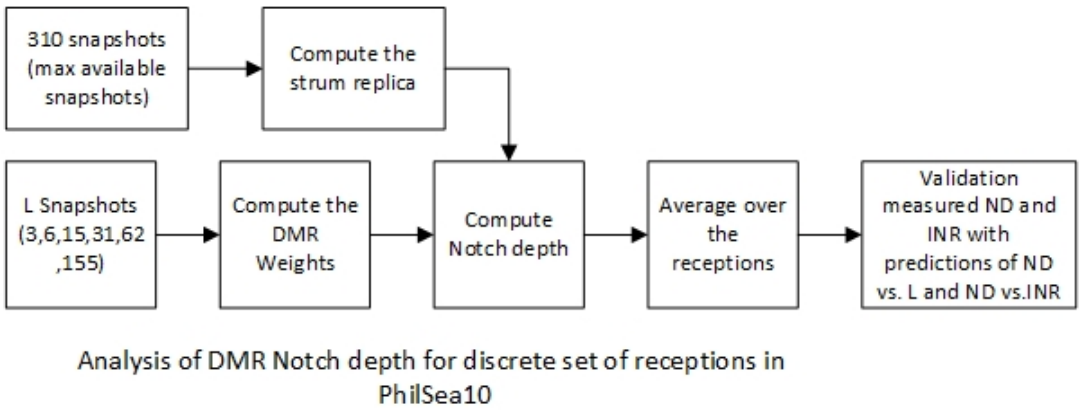

Figure 5.6: Block diagram illustrating the process for analysis of DMR ND for discrete set of receptions in PhilSea10.

As per the previous report, a maximum number of 310 snap shots with a < 60 Hz frequency of each strum component is identified and with a 50 % overlap and a block length of 1 sec is used in the discrete set of receptions. The maximum rank considered for the discrete set of receptions is 2. This is done by observing the spectrum of FFT of eigenvectors where the up going signal was observed to be eigenvector 1 and the down going signal was observed to be eigenvector 2. All these snapshots are subjected for the estimation of background noise level and INR of the strum. Following the identification of strum components, the weight factor of DMR (Details of this quantity estimation can be found in chapter 2) is found using different subsets with a snapshot range, L of 3 to 155. Considering the 310 snapshots as ensemble case, the Notch depth for each DMR vector is

estimated by equating the replica vector, Vi to the eigenvector, e1 (Details of computation can be found in Chapter 2). Selection of 31 of the DVLAs 150 elements is based on the fact that the minimum ratio of sensors to snapshots, c is 0.1 [7].

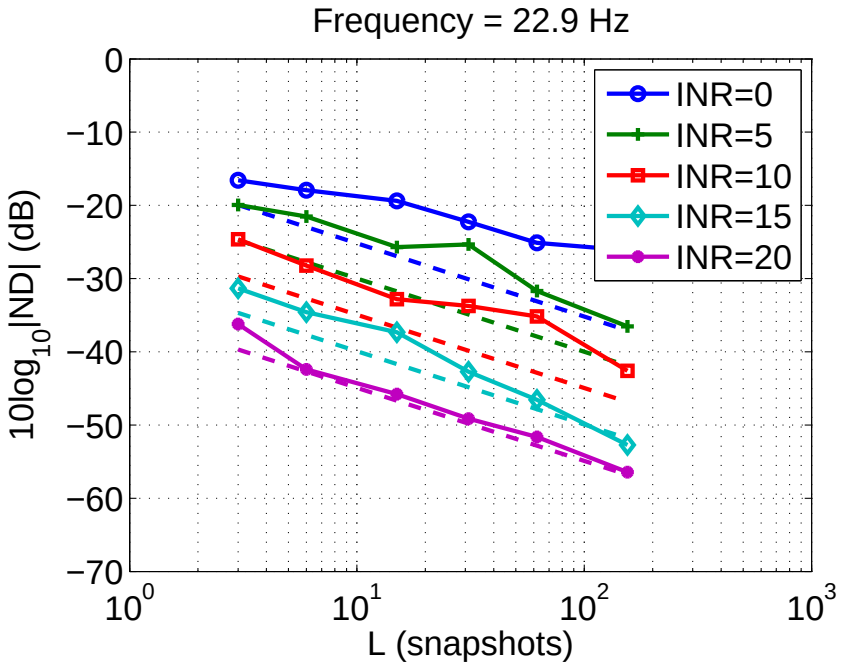

Figure 5.7: Comparison of predicted and estimated ND vs. L for the discrete data set. Solid lines show the results for 22.9 Hz, and dashed lines indicate the model predictions.

The measured mean ND measurements which are computed and validated with random matrix theory model predictions by processing 2901 receptions (across all the tomographic receptions T1 to T6 are processed). These plots (figures 5.7 ,5.8 and 5.9) were obtained by sorting the data into 5 dB INR bins and computing the mean for each bin. The figure shows results for the 22.9 Hz band; other frequencies exhibit more or less similar behavior. With the exception of the results for 0 dB INR, there is good agreement between the RMT model and the measurements. Even though there are number of factors for the discrepancy for the 0 dB INR it is mainly due to low signal levels. The most notable feature of the PhilSea10 ND results is the slope of the curves. The RMT model predicts that the slope of the ND versus snapshots curve in this figure 5.7 is -10 dB of ND per decade of snapshots.

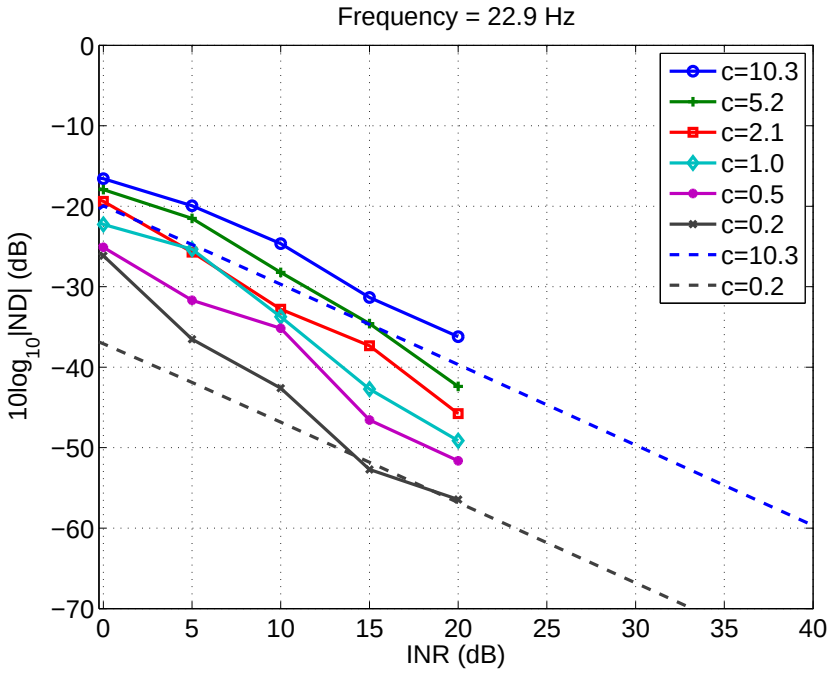

Figure 5.8: Comparison of predicted and estimated ND vs. INR for the discrete data set. Solid lines show the results for 22.9 Hz, and dashed lines indicate the model predictions.

Similarly, the RMT model predicts that the slope of the ND versus INR curve in Fig. 5.8 plot should be -1 dB. Averaging the PhilSea10 results over all frequency bins between 10 Hz and 60 Hz yields a mean slope computed at this 22.9 Hz frequency is -9.42 dB/dec for ND vs. snapshots and a mean slope of -1.11 for ND versus INR. This is remarkable agreement considering that the real data does not meet all of the model assumptions. For instance, the strum contains two components whereas the RMT model assumes a single interferer. Also, the analysis requires that $c = 0.1$ need to be used as a proxy for the unavailable ensemble statistics.

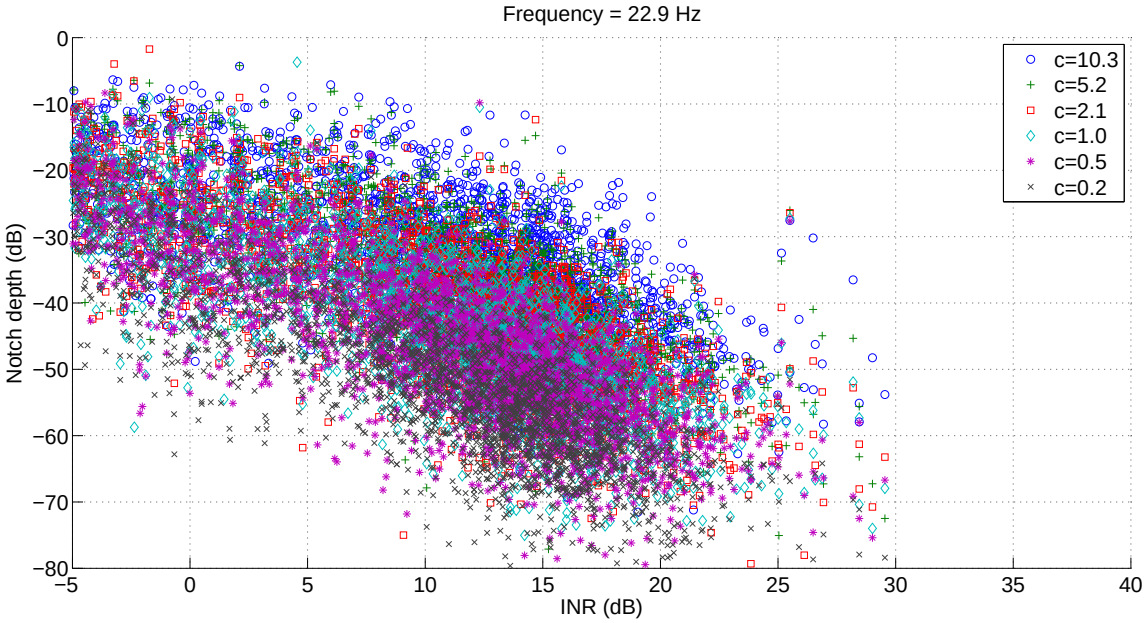

Figure 5.9: Scatter plot of ND vs.INR illustrating all the 2901 receptions in the discrete data set.

Figure 5.9 shows the scatter plot of the notch depth and INR measurements of all the 2901 receptions. This shows the deviation of low strum INR values from the RMT predicted model. For lower INRs, there is a deviation from the predictions as observed in this scatter plot as a result mutiple interefers (see 3.4 section).

5.4 Analysis of DMR Notch depth in continuous set receptions

The parameters which are used throughout the computation of continuous receptions for a 2 sec block length, hanning window overlap by 50%. The dominant subspace rank considered throughout the continuous receptions is 3 which were observed by analyzing the spatial spectrum of FFT of eigenvectors. In which it was observed that the eigenvector 1 is the up going signal, eigenvector 2 the down going one while the eigenvector 3 has strong traces of both up and down going signals.
The difference between the discrete and continuous set of receptions in analysis point of view is that the maximum number of snapshots can be significantly increased in continuous receptions where as the in discrete set we cannot. Moreover, the receptions available in the PhilSea10, for discrete are 2901 but for continuous there are not that many (depends on the split of receptions considered see table 4.4).
When we combine all the datasets it sums up to 240 Hrs(55*2+60+12*2+10 from the table 4.3) The notch depth computed for a total of 240 receptions (each reception lasting an hour) belonging to different data sets does not validate the random matrix theory model

predictions. So, splitting the data set in to smaller segments for further analysis is required to get more number of receptions.

5.5 Splitting the Continuous receptions in to smaller segments

To get more set of receptions for the analysis, the only option is to split in to smaller set of receptions even though the length of the snapshots is significantly reduced. In this analysis, the continuous receptions are split in to 10, 20, 30 min segments which corresponds to maximum snapshots available as 599, 1153, 1753 respectively (as the ensemble case) with 50 % overlap, 2 sec block length.
By observing the K-omega spectra of all the data sets, belonging to start days 143rd and 198th have relatively high strum content than the other datasets. Where as the data sets starting on 135, 190 and 192 have strum lasting up to 20 Hz only. The 192nd day dataset which is 36 Hr long has a medium strum content. These are observed by having a look at spatial spectra across all the time receptions. Hence, these data sets in the Phil Sea can be used for the DMR notch depth analysis. In this thesis, data set belonging 143rd is used for the computation of DMR notch depth.

5.5.1 Validation of RMT model of ND vs. INR in Continuous receptions

Consider the data set starting from 143rd day which has 164 receptions (55 Hr data). Below is a block diagram for the analysis for DMR notch depth vs. INR for continous receptions in PhilSea10.

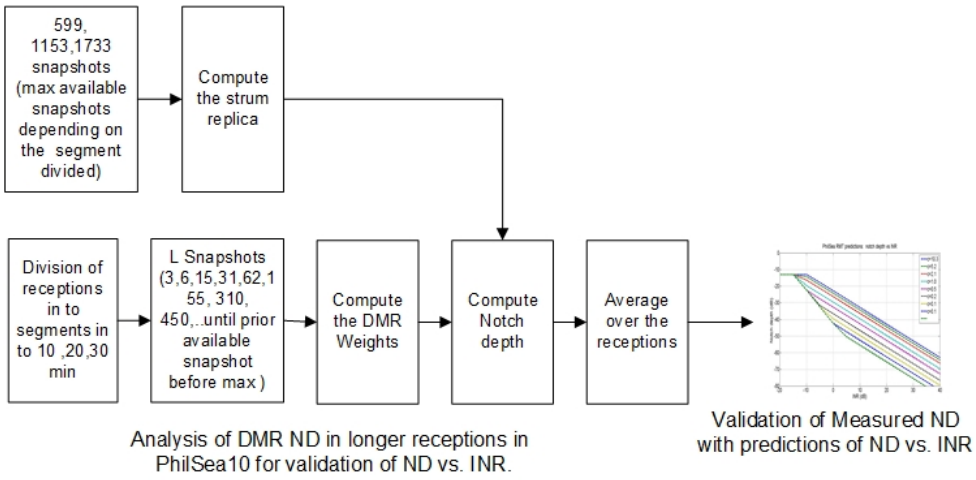

Figure 5.10: Block diagram illustrating the process for analysis of DMR ND for Continuous set of receptions in PhilSea10 for validation of ND vs. INR

The analysis of validation for ND vs. INR is done in a similar fashion as in discrete case (figure 5.6) after dividing the receptions in to smaller segments. After the division of segments (20 min in this case, the subset of snapshots are dealt the estimation of background noise level and INR of the strum. After identifying the components of strum, the weight factor of DMR (Details of this quantity estimation can be found in section 2.2) is found using different subsets with a snapshot range, L of 3 to 1153. Considering the 1153 snapshots as ensemble case, the Notch depth for each DMR vector is estimated by equating the replica vector, Vi to the eigenvector, e1 (Details of computation can be found in Chapter 2). After the notch depth is measured it is averaged over all the receptions (164 in this case) and validated to its RMT prediction of ND vs. INR.
Lets now, validate the measured ND with respect to RMT predictions of ND vs. INR in the data set as described in figure 5.11.
The figure 5.11 indicates the ND vs. INR plot of the measured DMR Notch depth in solid lines and its predicted values according to the random matrix theory model are represented in the dashed lines.

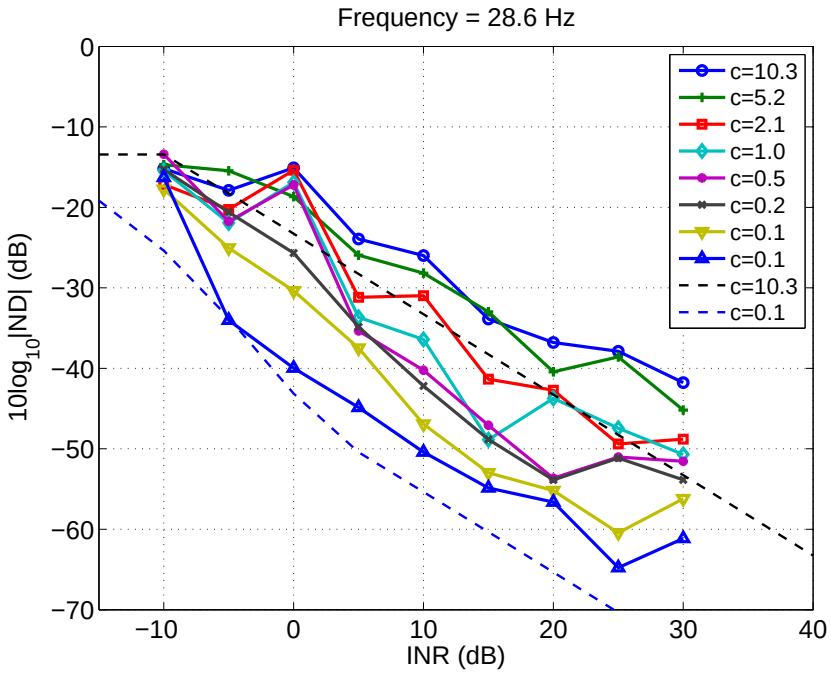

Figure 5.11: Comparison of predicted and estimated ND vs. INR for the continuous data set starting on 143rd day. Solid lines show the results for 28.6 Hz, and dashed lines indicate the model predictions.

The ND vs. INR analysis work well when a data set is divided in to a smaller segments say in this case, 20 min reception length. The computed results by RMT model for ND vs. INR plot lie within the predicted results except for couple of high aspect ratio values, c which is due fewer number of snapshots which are near the threshold of RMT model and the mean of the ND do not accurately obey the RMT predictions (see chapter 3.4) .
The ND Vs. INR for INR values < 0 dB have fewer number of receptions as shown in figure 5.12 in the form of histogram representing the number of receptions containing the INR values.

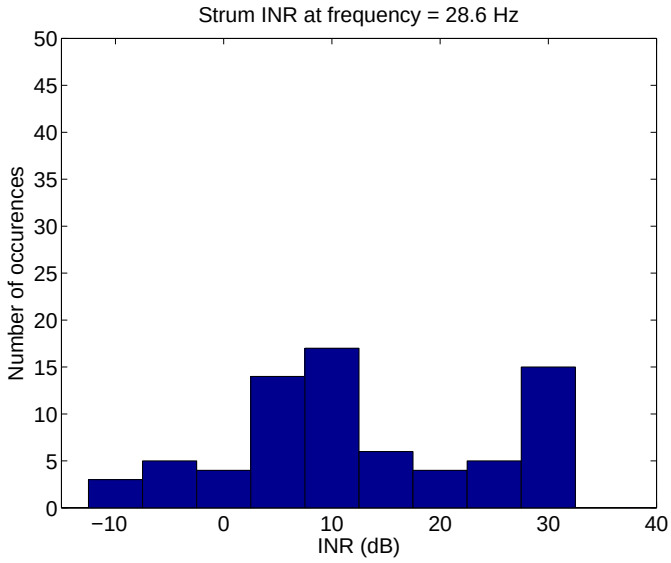

Figure 5.12: Histogram illustrating number of occurences at each INR bin for 28.6 Hz

As, this was done in a single data set, the maximum Kz values (wave number) increases in a uniform manner w.r.t. frequency. With respect to the ND Vs. L analysis, barely dividing the receptions in to smaller segment do not yield accurate validation results as the mean of ND computed of these the receptions has a deviation because the strum is not constant throughout the dataset. Hence, there is a necessity of picking constant strum from the continuous set of receptions where each set of constant strum reception can be treated as Monte Carlo trials.

5.6 Selection of Constant Strum receptions for ND vs. L validation

The constant strum receptions are selected (the details of which were described in chapter 4) by picking the squared norm >0.9 of the first eigenvector projected on to the subspace spanned by the eigenvectors 1,2 and 3 with respect to reference value. Here, the reference value is the first reception which can be 10, 20 or 30 min depending on the division segment chosen for the continuous receptions. The constant strum is picked so as to group INRs which have same value that is required for the computation of ND vs. L validation plots. The below block diagram in figure 5.13 shows the analysis of validation of RMT model predictions of ND vs. L with DMR notch depth for continuous receptions in PhilSea10.

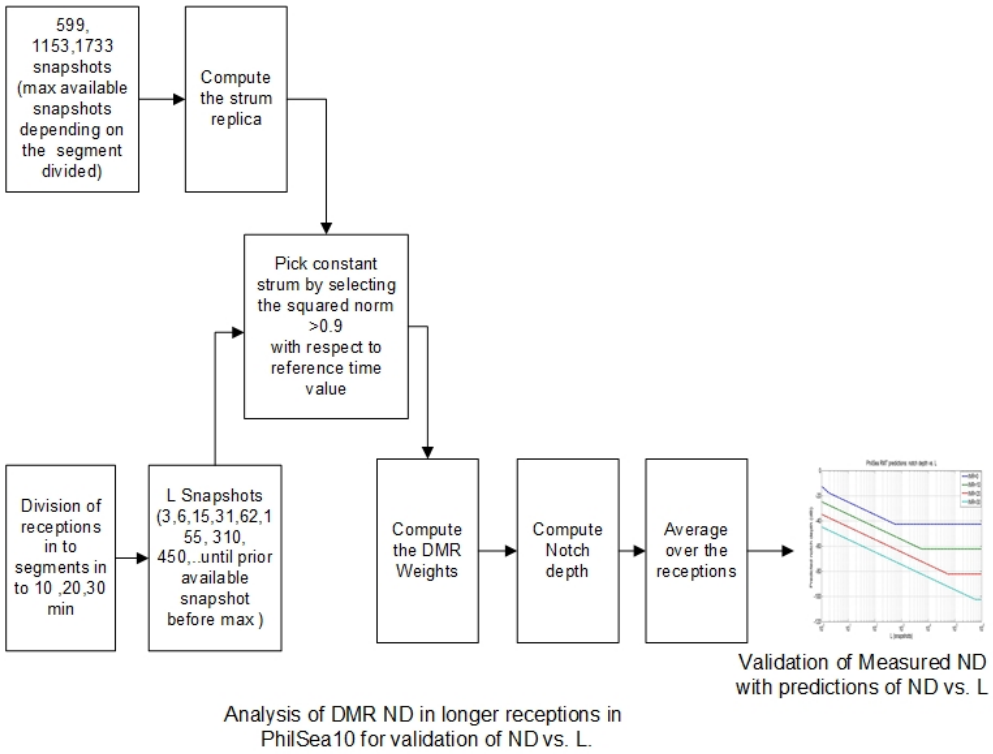

Figure 5.13: Block diagram illustrating the process for analysis of DMR ND for Continuous set of receptions in PhilSea10 for validation of ND vs. L

The analysis is done in the same way as in the case of validation of ND vs.INR but the only notable difference is that after dividing the longer receptions in to smaller ones, the constant strum is picked for computation of weight vectors, ND and the strum replica. Briefly, only files which have relatively constant strum with respect to the initial time (20 min as reference) are selected instead of all the receptions (164 in this case) for the analysis.

5.6.1 Division of continuous receptions in to 10 min receptions

Dividing the continuous receptions in to 10 min segments yields more accurate results due to increase in the Monte Carlo trials for the constant strum receptions though it may comprise the number of snapshots chosen. The maximum number of snapshots available for a 10 min reception with a 2 sec block length is 599.
Below is the Notch depth Vs. Snapshots plot for the 10 min receptions having 61 and 42 constant strum receptions for frequencies of 17.6 and 23.8 Hz in the data set starting on 143^{rd} day. Note that strum is not constant throughout the data (time) as well as frequency. Hence, different constant receptions are resulted for each frequency .The subset of snapshots considered here are [3 6 15 31 62 155 310 450 599] where 599 is treated as an ensemble case.
Measured ND agrees well with the RMT predictions:

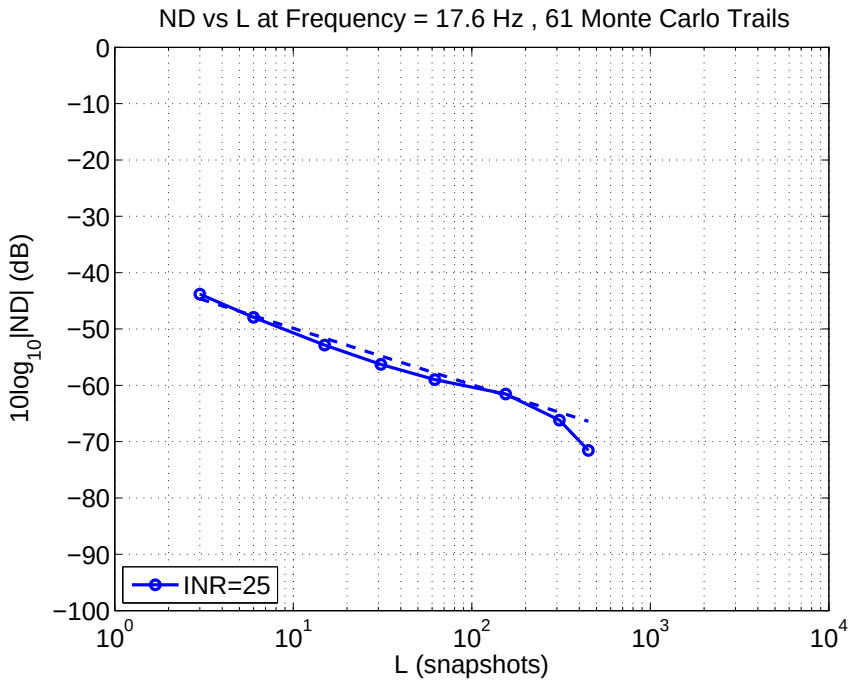

Figure 5.14: Comparison of predicted and estimated ND vs. L for a 10 min constant strum. Solid lines show the results for 17.5 Hz and dashed lines indicate RMT predictions.

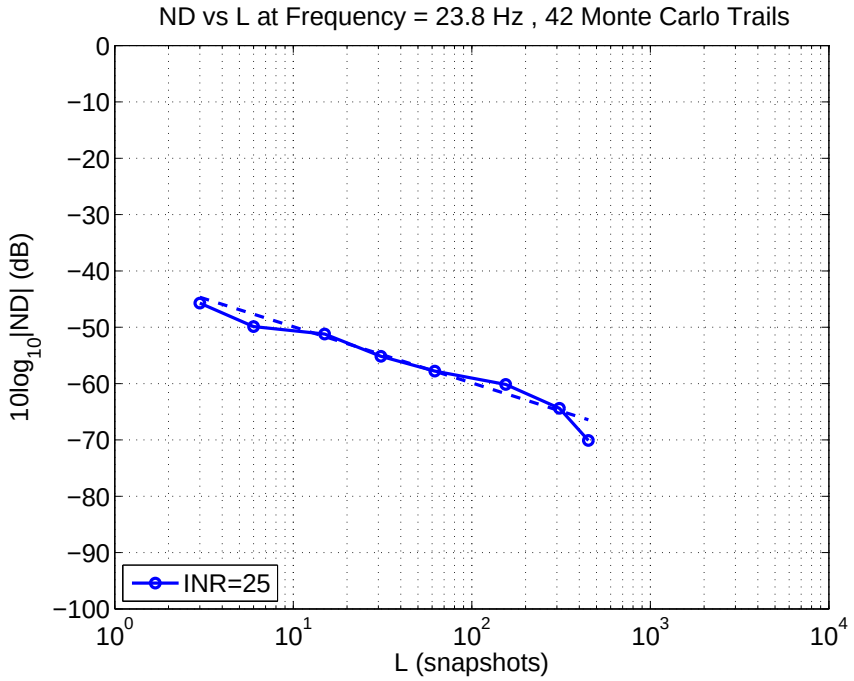

Figure 5.15: Comparison of predicted and estimated ND vs. L for a 10 min constant strum. Solid lines show the results for 23.8 Hz and dashed lines indicate RMT predictions.

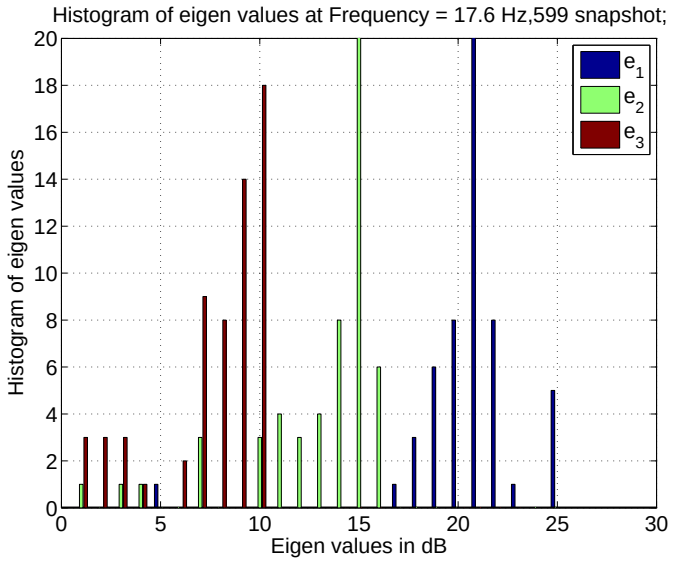

Figure 5.16: Histogram illustrating eigenvalues in dB for constant strum receptions (10 min) at 17.5 Hz

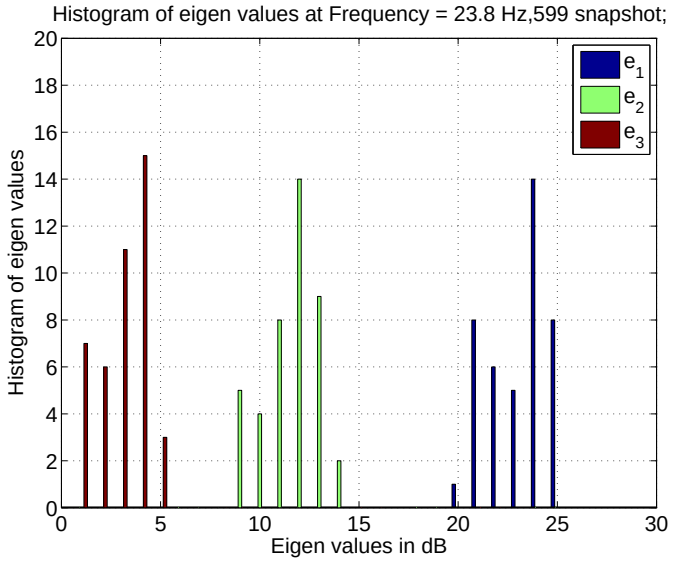

Figure 5.17: Histogram illustrating eigenvalues in dB for constant strum receptions (10 min) at 23.8 Hz

Observation :
The Measured Notch depth agrees with the RMT predictions when the first eigenvalue is well separated from the others.
The measured ND at frequencies 17.5 Hz and 23.8 Hz yields a mean slope of -11.47 dB/dec in figure 5.14 and -9.89 dB /dec in figure 5.15 in regards to RMT prediction slope of ND vs. L of -10 dB per decade.

A case for the measured ND not obeying with the RMT predictions:

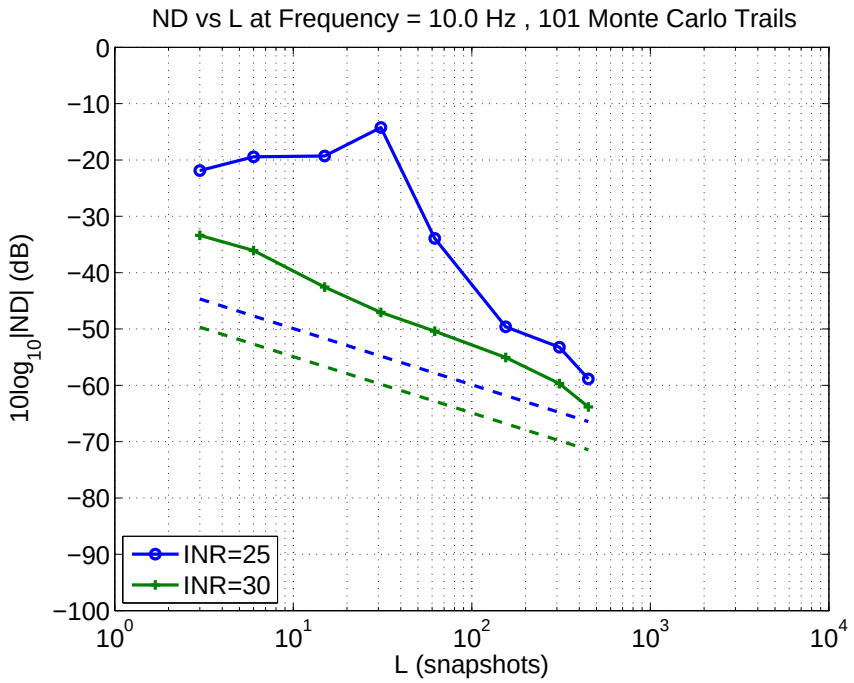

Figure 5.18: Comparison of predicted and estimated ND vs.L for 10 min constant strum. Solid lines show the results for 10 Hz and dashed lines indicate RMT predictions.

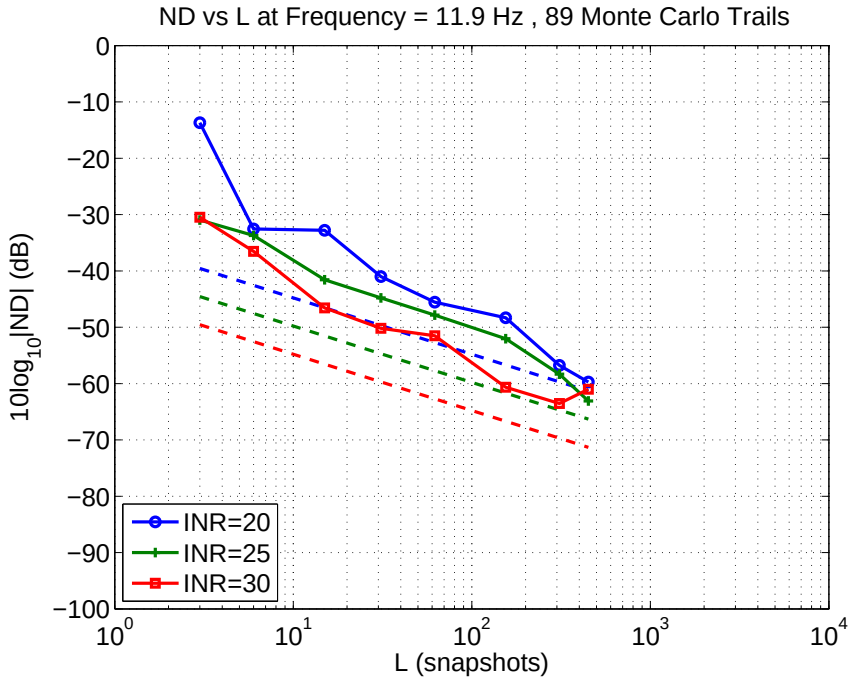

Figure 5.19: Comparison of predicted and estimated ND vs. L for a 10 min reception (constant strum). Solid lines show the results for 11.9 Hz and dashed lines indicate RMT predictions.

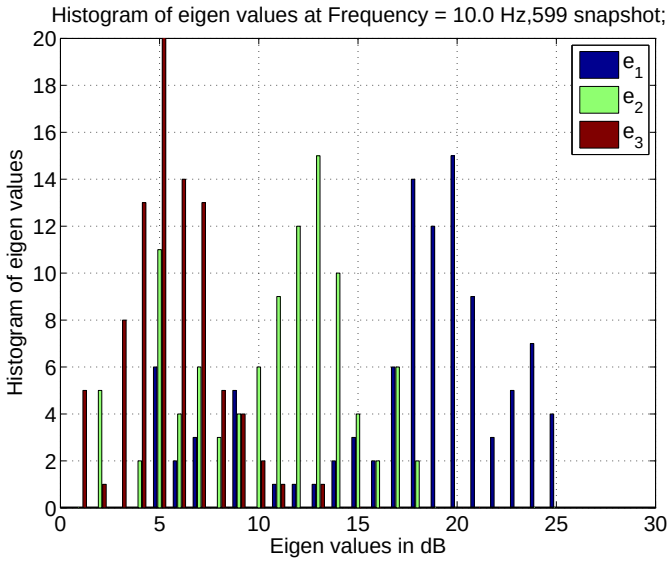

Figure 5.20: Histogram illustrating eigenvalues in dB for constant strum receptions (10 min) at 10 Hz

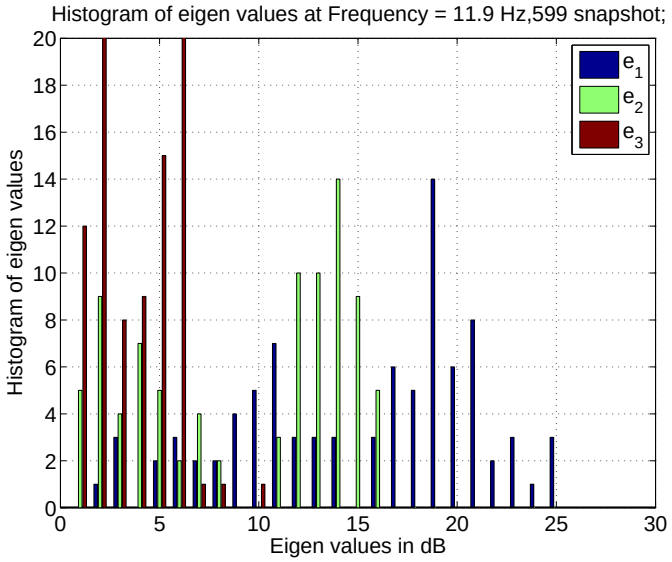

Figure 5.21: Histogram illustrating eigenvalues in dB for constant strum receptions (10 min) at 11.9 Hz

Observation:
It is observed that the RMT predictions are not obeyed when the dominant eigenvalues overlap with each other and also when the first eigenvalue is close by with the other two. The measured ND at frequencies 10 Hz and 11.9 Hz yields a mean slope of -19.64 dB/dec in figure 5.18 and -14.1 dB /dec in figure 5.19 in regards to RMT prediction slope of ND vs. L of -10 dB per decade.

5.6.2 Division of continuous receptions in to 20 min Receptions

When the Continuous receptions are split in to 20 min receptions, an increase in maximum number of snapshot availability to 1153 and reduction in number of constant strum receptions is observed.
The parameters are the same as described for 10 min receptions except the fact that the snapshot subsets considered are 3, 6, 15, 31, 62, 155, 310, 620, 1153 where 1153 is treated as an ensemble case.
Cases of Good prediction:

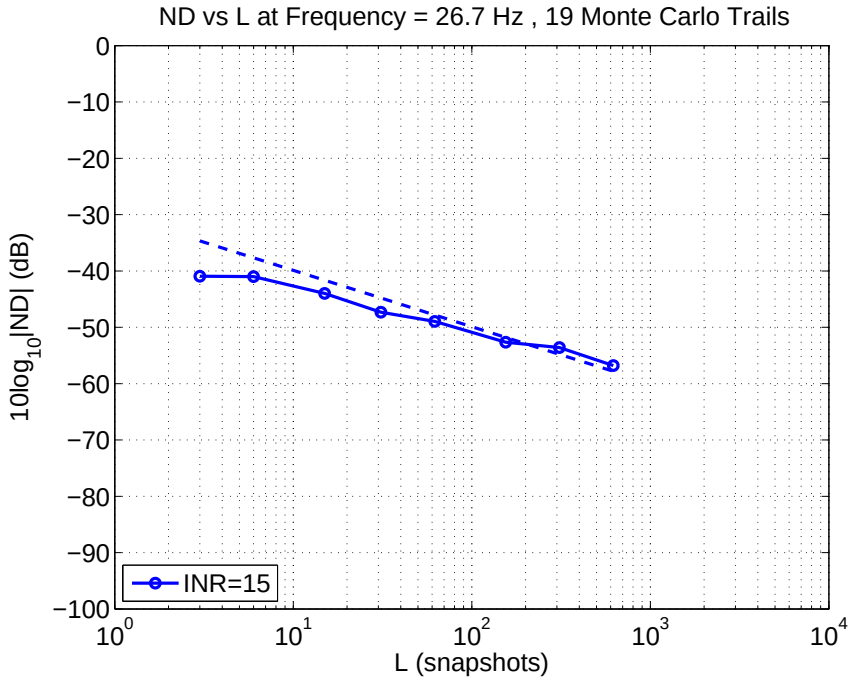

Figure 5.22: Comparison of predicted and estimated ND vs. L for a 20 min constant strum. Solid lines show the results for 26.7 Hz and dashed lines indicate RMT predictions.

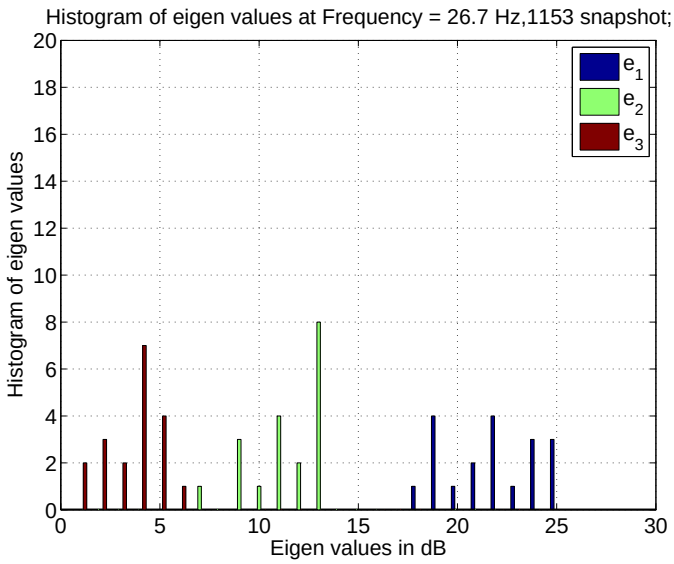

Figure 5.23: Histogram illustrating eigenvalues in dB for constant strum receptions (20 min) at 26.7 Hz

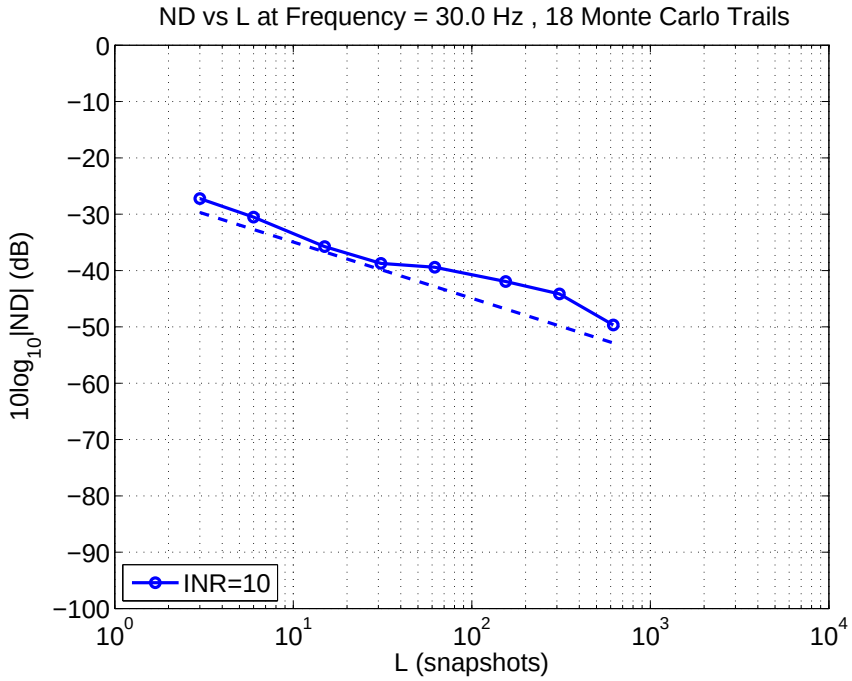

Figure 5.24: Comparison of predicted and estimated ND vs. L for a 20 min reception (constant strum). Solid lines show the results for 30 Hz and dashed lines indicate RMT predictions.

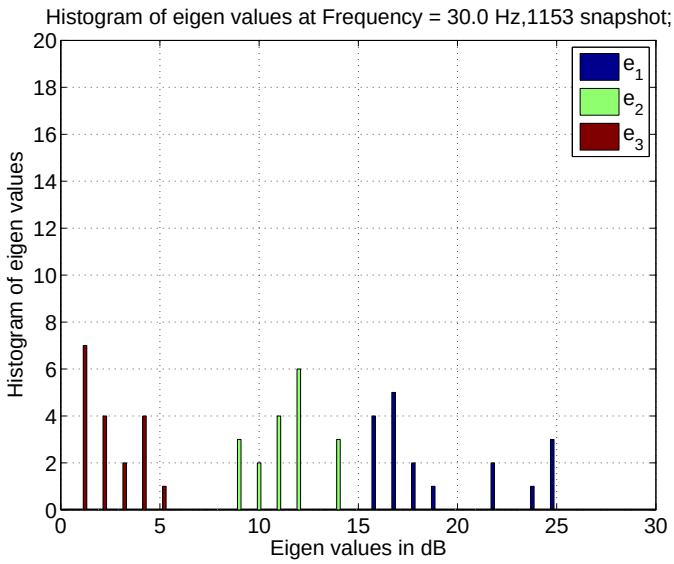

Figure 5.25: Histogram illustrating eigenvalues in dB for constant strum receptions (10 min) at 30 Hz

Observation:
Again, the Measured Notch depth agrees with the RMT predictions when the first eigenvalue is well separated from the others. The measured ND at frequencies 26.7 Hz and 30 Hz has a mean slope of -7.1745 dB/dec in figure 5.23 and -10.95 dB /dec in figure 5.24 in regards to RMT prediction slope of ND vs. L of -10 dB per decade.

Cases of bad prediction:

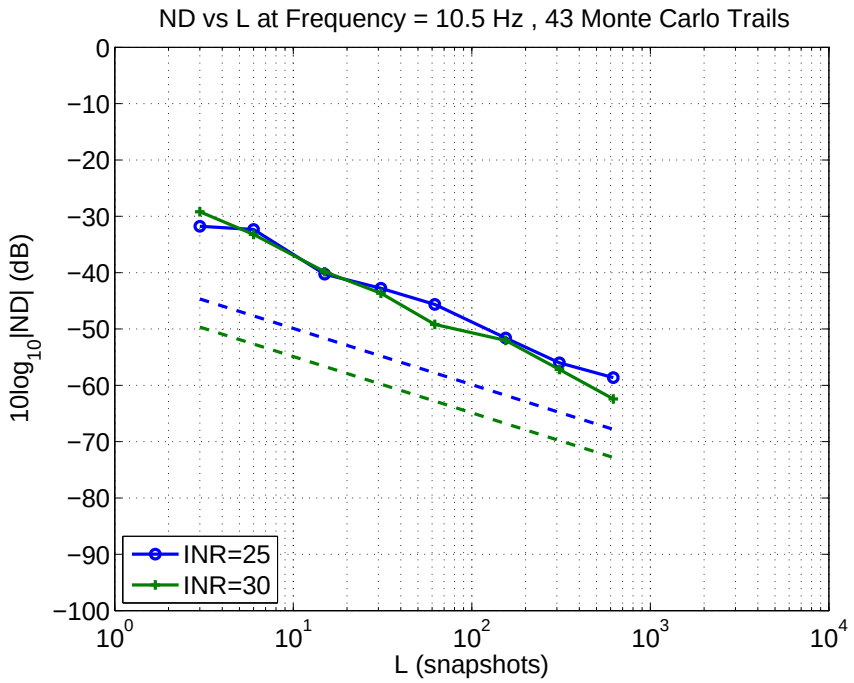

Figure 5.26: Comparison of predicted and estimated ND vs. L for a 20 min reception (constant strum). Solid lines show the results for 10.5 Hz and dashed lines indicate RMT predictions.

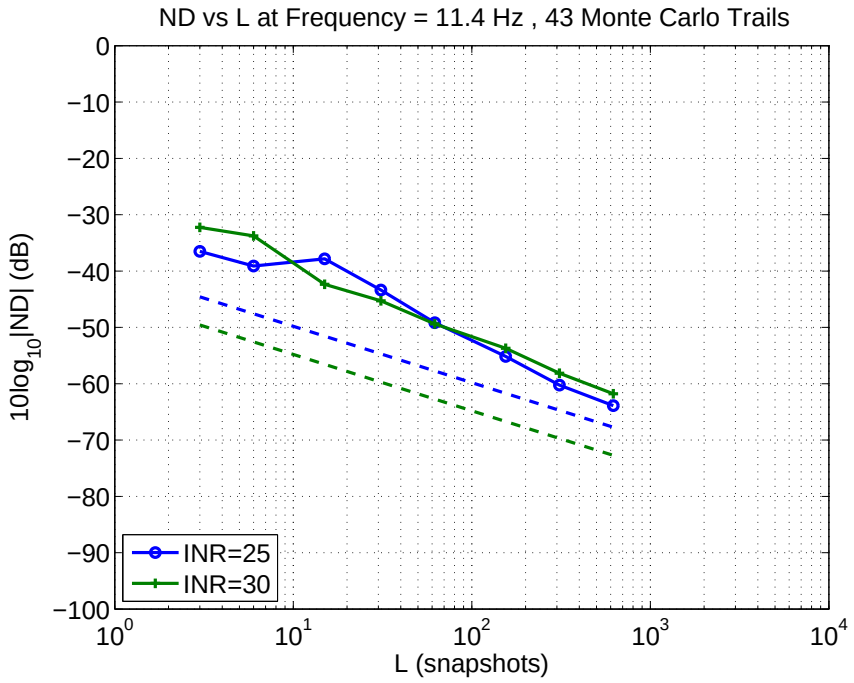

Figure 5.27: Comparison of predicted and estimated ND vs. L for 20 min constant strum. Solid lines show the results for 11.4 Hz and dashed lines indicate RMT predictions.

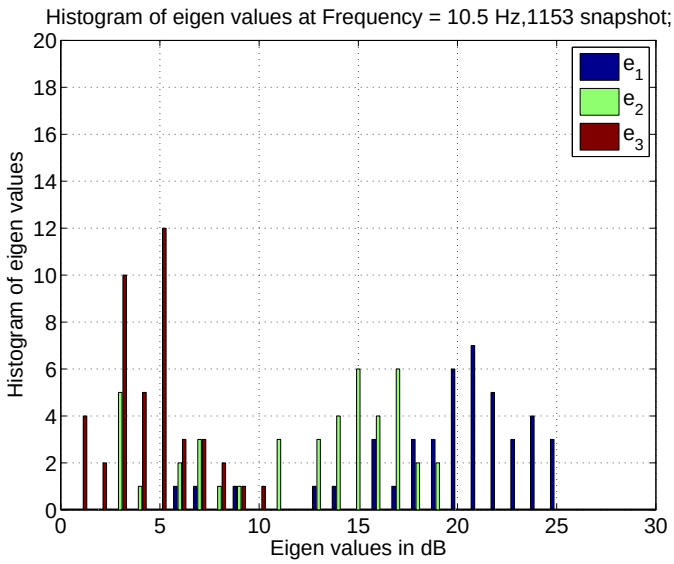

Figure 5.28: Histogram illustrating eigenvalues in dB for constant strum receptions (20 min) at 10.5 Hz

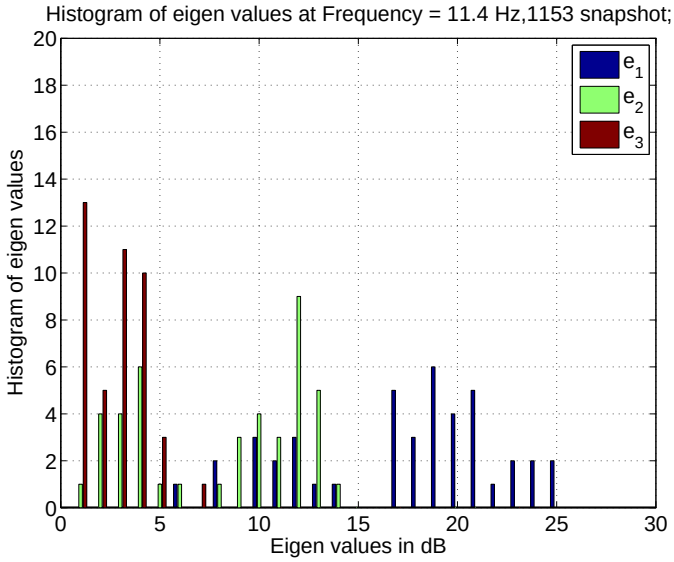

Figure 5.29: Histogram illustrating eigenvalues in dB for constant strum receptions (20 min) at 11.4 Hz

Observation:
Yet again, It is observed that the RMT predictions do not obey when the dominant eigenvalues overlap with each other and also the when the first eigenvalue is close to other two. The measured ND at frequencies 10.5 Hz and 11.4 Hz yields a mean slope of -12.24 dB/dec in figure 5.26 and -12.59 dB /dec in figure 5.27 in regards to RMT prediction slope of ND vs. L of -10 dB per decade.

5.6.3 Division of continuous receptions in to 30 min receptions

When the Continuous receptions are divided in to 30 min receptions, an increase in maximum number of snapshot availability to 1733 and a significant reduction in number of constant strum receptions are observed (Monte Carlo trials).The parameters are the same as described for 10 min receptions except the fact that the snapshot subsets considered are 3 6 15 31 62 155 310 620 1240 1500 1733 where 1733 is treated as an ensemble case.
Cases for good predictions:

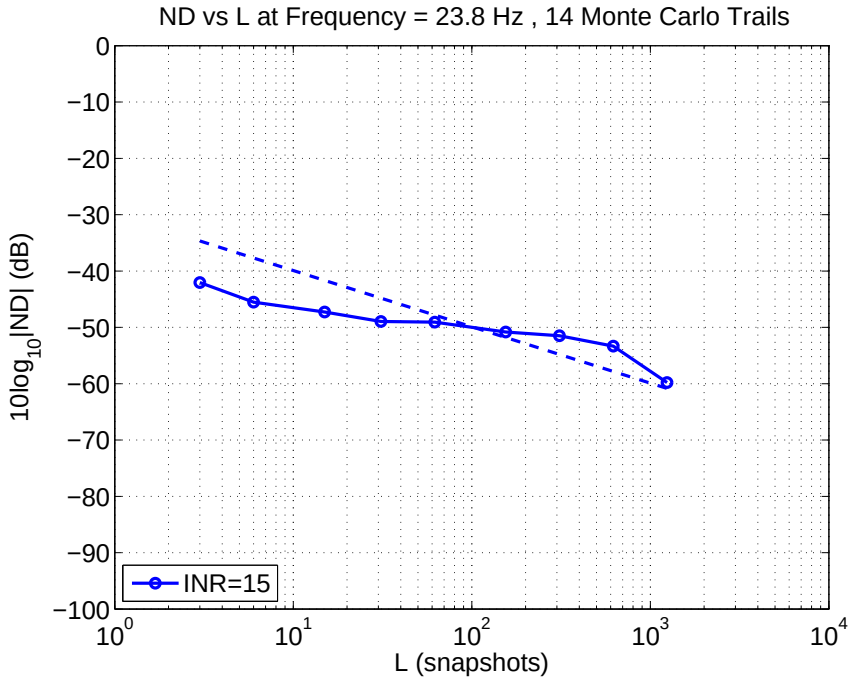

Figure 5.30: Comparison of predicted and estimated ND vs. L for a 30 min reception (constant strum). Solid lines show the results for 23.8 Hz and dashed lines indicate RMT predictions.

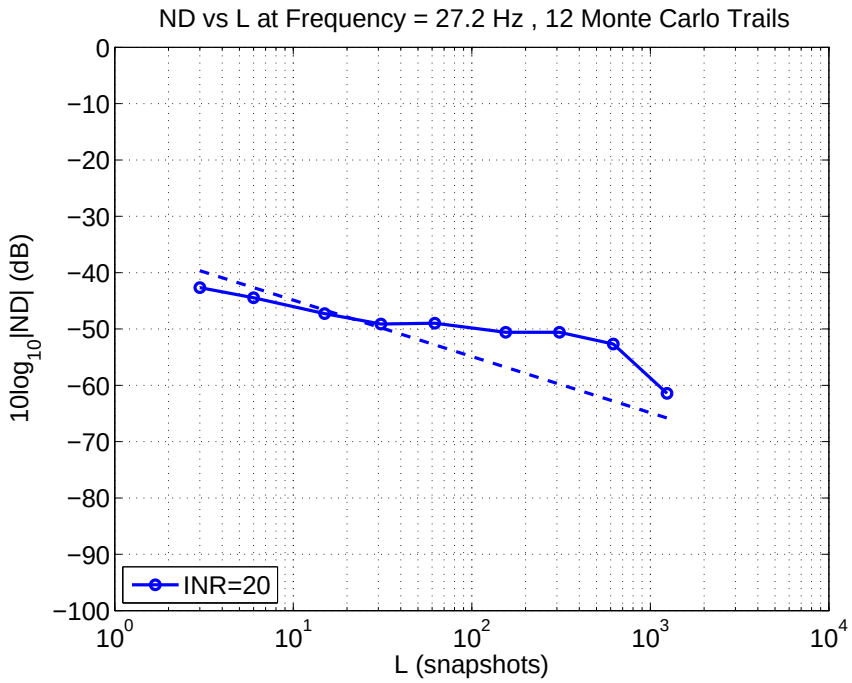

Figure 5.31: Comparison of predicted and estimated ND vs. L for a 30 min reception (constant strum). Solid lines show the results for 27.2 Hz and dashed lines indicate RMT predictions.

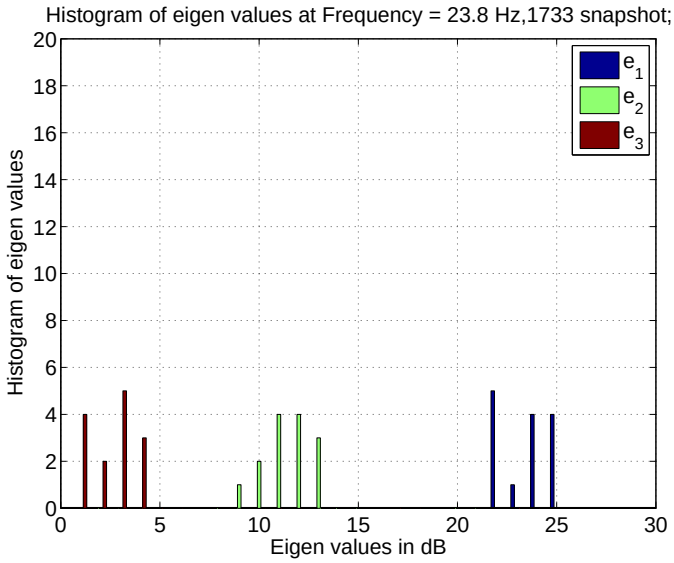

Figure 5.32: Histogram illustrating eigenvalues in dB for constant strum receptions (30 min) at 23.8 Hz

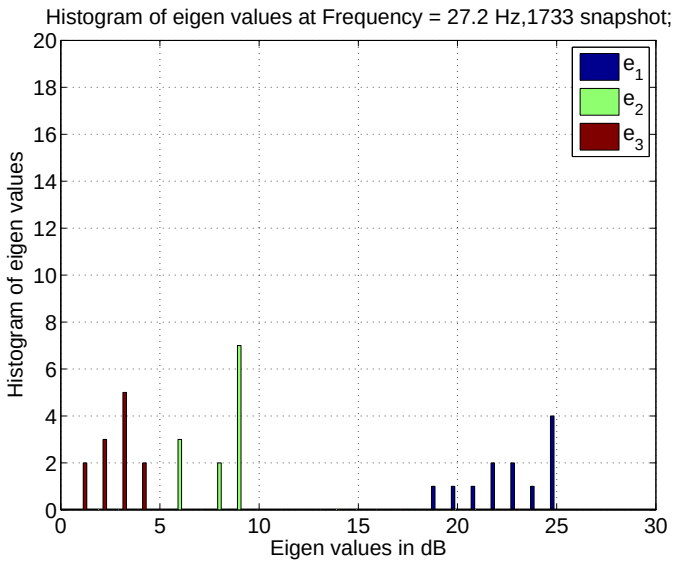

Figure 5.33: Histogram illustrating eigenvalues in dB for constant strum receptions (30 min) at 27.2 Hz

Observation :
Once more, the Measured Notch depth agrees with the RMT predictions when the first eigenvalue is well separated from the others. The measured ND at frequencies 23.8 Hz and 27.2 Hz yields a mean slope of -4.2567 dB/dec in figure 5.30 and -3.95 dB /dec in figure 5.31 in regards to RMT prediction slope of ND vs. L of -10 dB per decade.

Examples for worst Case:

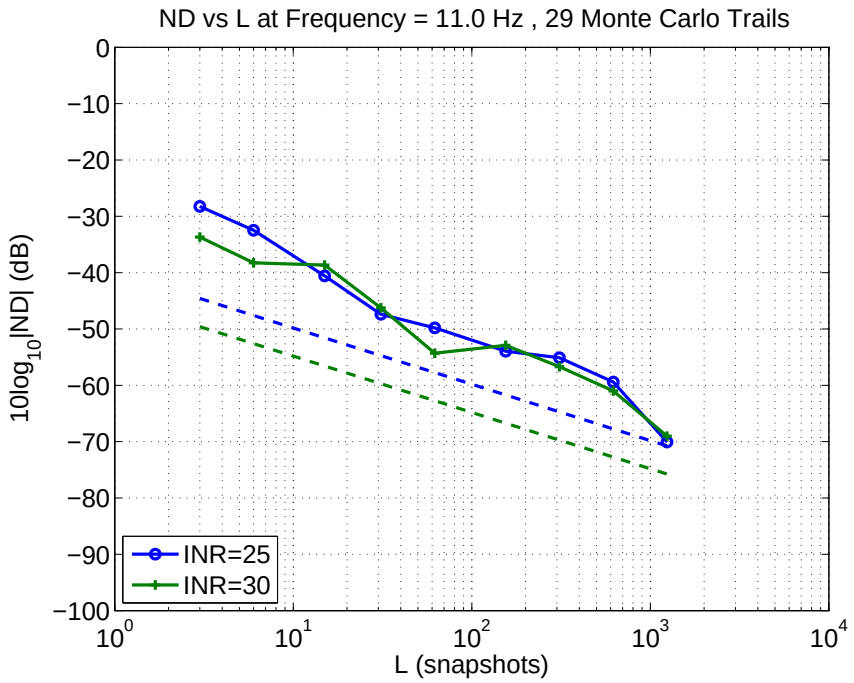

Figure 5.34: Comparison of predicted and estimated ND vs. L for a 30 min reception (constant strum). Solid lines show the results for 11 Hz and dashed lines indicate RMT predictions.

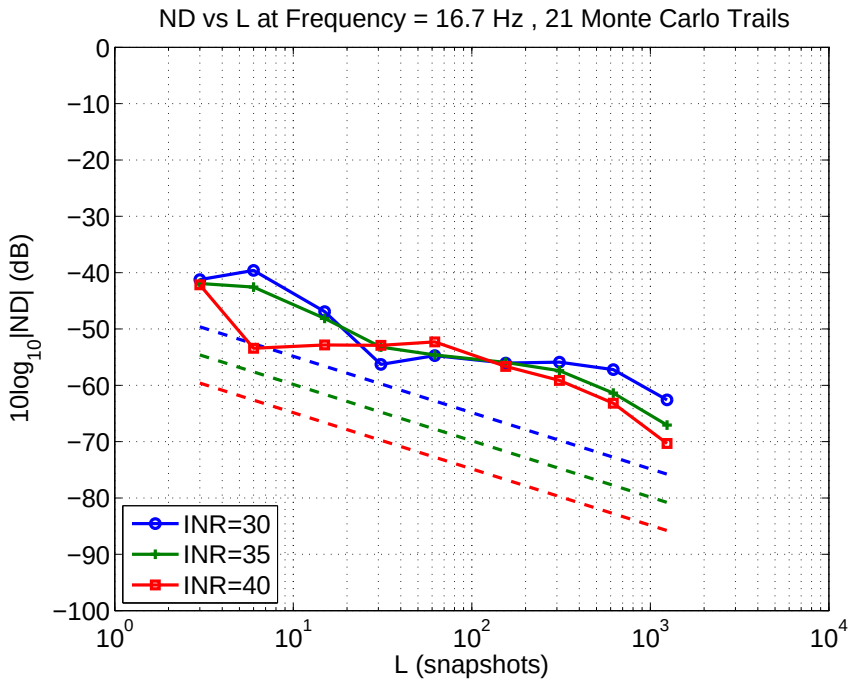

Figure 5.35: Comparison of predicted and estimated ND vs. L for a 30 min reception (constant strum). Solid lines show the results for 16.7 Hz and dashed lines indicate RMT predictions.

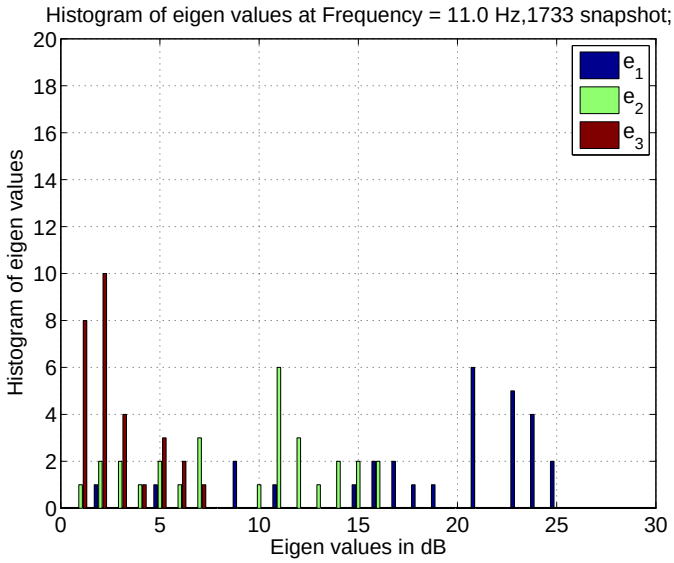

Figure 5.36: Histogram illustrating eigenvalues in dB for constant strum receptions (30 min) at 11 Hz

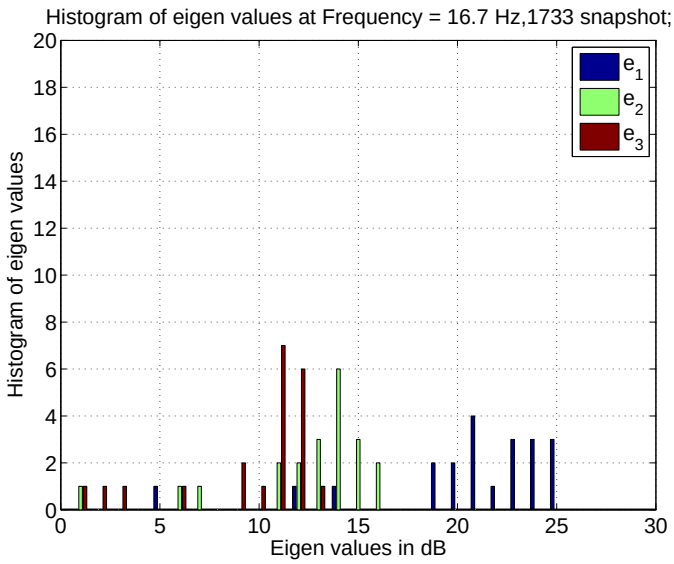

Figure 5.37: Histogram illustrating eigenvalues in dB for constant strum receptions (30 min) at 16.7 Hz

Observation :
Where the RMT predictions do not obey when the dominant eigenvalues overlap with each other and also the when the first eigenvalue is close by with the other two. The measured ND at frequencies 101 Hz and 16.7 Hz yields a mean slope of -13.33 dB/dec in figure 5.34 and -7.6 dB /dec in figure 5.35 in regards to RMT prediction slope of ND vs. L of -10 dB per decade.

5.7 Comparing Rank Estimation techniques in a worst case:

In this section, we compare rank estimation techniques like AIC, MDL and RMT with 'Strum detector technique' (picking peak 'Kz' values) technique in a worst case senario where the eigenvalues overlap with each other.
This is done in a similar way as described in section 5.2. For this study, lets consider a 20 min constant strum reception where the strum detector technique fails, say at frequency 10 Hz. Now, lets validate the measured ND with its RMT predictions of ND vs. L.

Below is a ND vs.L plot for 20 min constant reception using eveckz (picking the maximum wave number values associated with the strum) rank estimation technique. Lets consider for a worst case scenario :

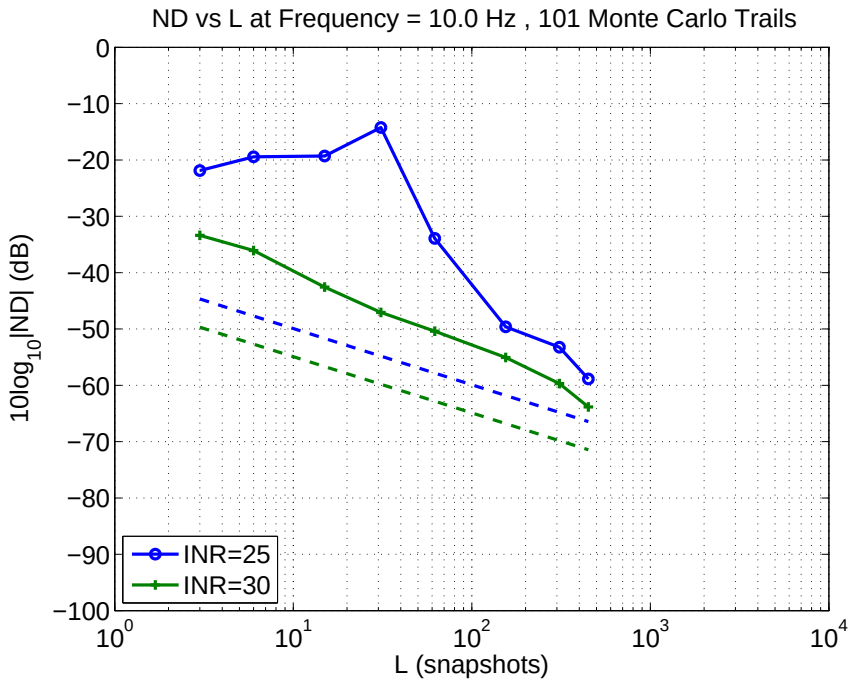

Figure 5.38: Comparison of predicted and estimated ND vs. L for a 20 min (constant strum) using strum detector rank estimation technique for a 10 Hz frequency

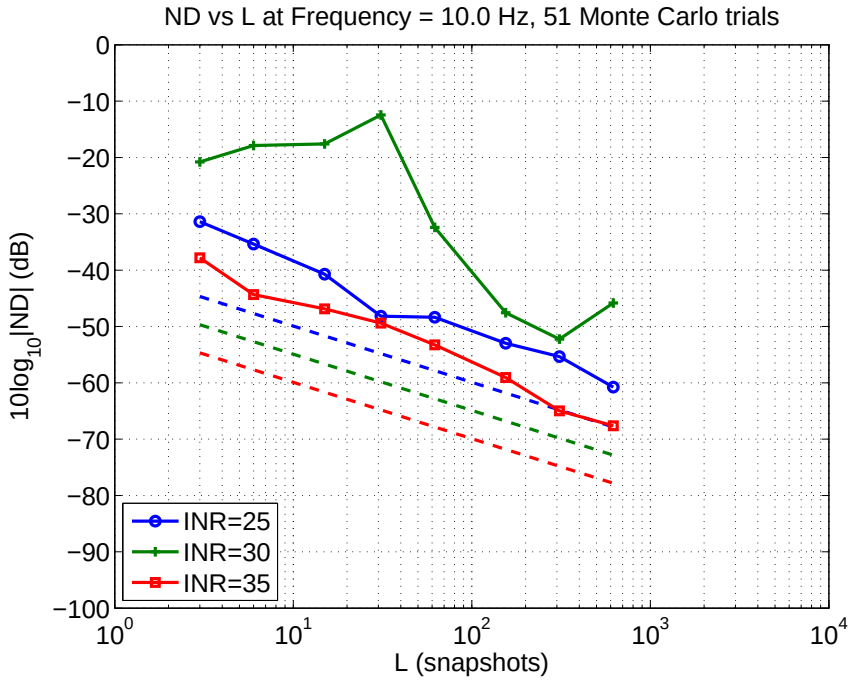

Figure 5.39: Comparison of predicted and estimated ND vs. L for a 20 min (constant strum) using AIC,MDL rank estimation techniques for a 10 Hz frequency

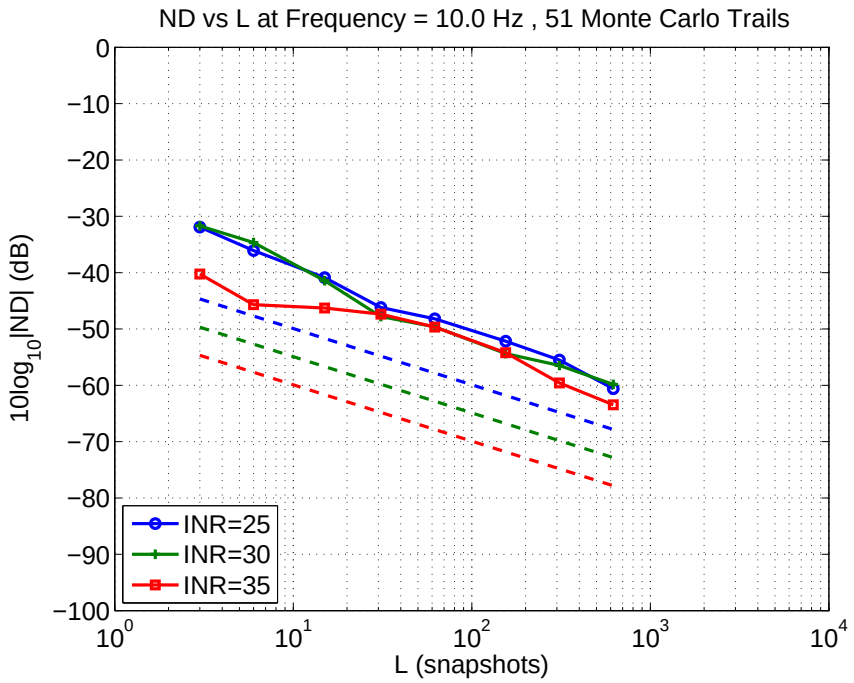

Figure 5.40: Comparison of predicted and estimated ND vs. L for a 20 min (constant strum) using RMT rank estimation techniques for a 10 Hz frequency

Observation:
It is observed that RMT rank estimation developed by Nadakuditi and Edelman fares better (as observed in Fig 5.40) in worst case scenarios when compared to strum detector technique (Figure 5.38) this proves eigenvalues play major role whenever there is a mismatch between measured ND values and RMT predictions. In this analysis, MDL and AIC rank estimation cannot be used as it does not yield better results.
The mean slopes of measured ND vs. L plots are -12.32, -12.186 and -11.86 dB for Figures 5.38, 5.39 and 5.40 respectively at frequency 10 Hz.

5.8 Alternate way of validating the DMR Notch depth

Instead of picking the constant strum, selecting files based on rank (single interferer mostly) of strum also works. The strum is an example of multiple interferer case, i.e. a three interferer case. The random matrix theory model was developed for a single interferer not for multiple interferers. Hence analyzing single interferer receptions (Rank 1 strum files) validates the random matrix theory model predictions. Hence single interferer files are picked (rank 1 files) and averaged across the dataset to analyze the measured notch depth results with respect to its RMT model predictions.

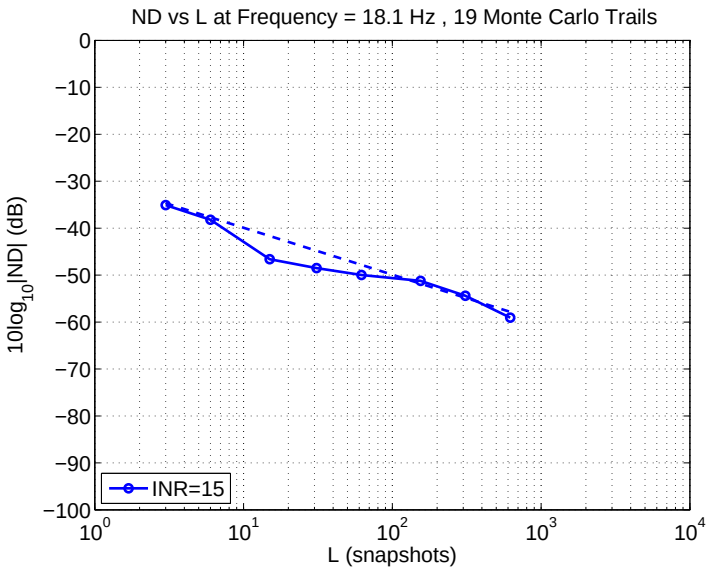

Figure 5.41: Comparison of predicted and estimated ND vs. L for a 20 min reception using only single interferer cases. Solid lines show the results for 11.9 Hz, and dashed lines indicate the model predictions.

It was also observed that picking only rank 3 receptions from the data set do not match the validation theory of RMT model.

5.9 Reasons for validation failure of DMR notch depth

The Random matrix theory model computed solely relies on the sample eigenvector (which is described in the chapter 2). But whenever, the most dominant eignvalue interlaces with other eigenvalues, there is a mismatch between the RMT model predicted values and measured ND values.
This was explained in a recent paper by Bloemendal et al [22] which has provided relevant results for the failure of validation in few cases. This paper provides numerous results on the sample eigenvectors , eigenvalue locations, including predictions of cone concentration for multiple interferers (spikes). This paper suggests that notch depth analysis should be redefined to measure the DMR ABF notch components in that subspace.
The other reasons are strum is a case of multiple interferer but the validation of RMT model for DMR ND was developed by taking account of a single interferer. The analysis also depends on the interferer location i.e., not necessarily orthogonal as described in chapter 3.

5.10 Summary

The validation of ND in discrete set of receptions is possible due to availability of high number of receptions (2901) for 310 snapshots as an ensemble case.

In the continuous receptions, splitting them in to segments is done to get more receptions. After splitting them, the ND vs. INR plots are analyzed for its validation with respect to RMT predictions.
For ND vs. L analysis, the constant strum receptions is picked. Whenever, there is overlap between eigenvalue 1 with other eigenvalues there is a mismatch between predicted and measured ND values. When eigenvalue 1 is well separated from other eigenvalues, a good agreement between predicted and measured ND values is observed. As constant strum gives very few values of INR, the ND vs. INR validation due to insufficient number of receptions. For a bad prediction, eigenvalue based rank estimation like RMT fares better than the eigenvector based rank estimation technique.
The 10 min receptions predict well than the 30 min receptions due to availability more number of Monte Carlo trials. The Random matrix theory model predictions work well for single interferer receptions.

Chapter 6: Conclusion

This chapter deals with the conclusion of the overall thesis and the extension of this study.

6.1 Concluding Comments

This thesis began with emphasis on understanding of DMR beamformer using the notch depth as the metric. The accuracy of RMT model for DMR notch depth which was developed by Wage and Buck has been tested on the simulated data initially and later on with the experimental data set (PhilSea10).
It is proved by KS test (5% significance), the DMR notch depth for any interferer case follows beta prime distribution. Moreover, the performance of DMR beamformer notch depth has been analyzed for single and multiple interferers using the simulated data. The effect of interferer's location on INR, RMT model of ND vs. L and its measurements, DMR ND and its distribution have been tested. It proves out that "D + 1" snapshots which were generally required for performance of DMR beamformer aren't sufficient for validating the RMT model of the DMR beamformer notch depth for multiple interferer cases. The other criteria is that whenever the interferer locations where close to each other (not orthogonal), the measured ND was deviating from the predictions.
The strum in the PhilSea10 Experiment is used as test signal to validate the RMT model of DMR notch depth; this is because the cable fairing in the PhilSea10 hasn't been implemented which gives us a full strum signal in it. Previously, Wage and others have implemented the Experimental validation of RMT model of DMR notch depth in PhilSea10 [7] by using the tomography receptions which were 155 seconds. This analysis was done for 958 receptions, which was a case of having high number of receptions (Monte Carlo trials) and less number of snapshots (310 as the ground truth). But the results of these measured ND did not follow the model exactly.
This thesis improves these results using the longer receptions. The longer receptions, 55 hrs chosen in this thesis, gave us the flexibility of choosing our own snapshot number at the cost of number of receptions (Monte Carlo trials). The eigenvalues of the strum fade in and out while the array revolves on the surface with one end fixed at the bottom (anchor) and this may be linked to tidal variations.
The longer receptions are divided in to 10, 20, 30 min for analysis. The 10 min files give better result than the 20 min and the 20 min files provide effective results than 30 min files as these files have relatively high number of Monte Carlo trials (receptions that were processed) even though the 30 min reception files have more availability of snapshots(1733).
The selection of constant strum relative to the initial time reception is taken to group the files which have same INR for improving the results of the ND vs. L model predictions. It is was observed that in 95 percent of the cases, whenever the histogram of most the dominant eigenvalue does not overlap with other eigenvalues, the measured notch depth agrees well with the RMT model predictions. In the other all cases, whenever the histogram of most

dominant eigenvalue overlaps with other eigenvalues, the measured ND does not meet the RMT predictions. This is because of the fact that the RMT model of the DMR beamformer has been derived using the accuracy of sample eigenvectors without taking in to account of their behavior with the sample eigenvalues.
A comparison of rank estimation techniques using Wax / Kaliath AIC, MDL , N/E RMT and strum detector (picking the eigenvectors associated peak $|Kz|$ values associated with the strum) is implemented. Generally, it was observed that the strum detector technique performs exceptionally well than the others. It was found that in 95 % of cases, the measured ND matches RMT predictions of ND vs. L whenever the most dominant eigenvalue does not overlap with other eigenvalues. But, in the worst cases where the most dominant eigenvalue overlap with others, the N/E RMT fares slightly better than the strum detector technique. This is because, the N/E RMT technique is derived based on eigenvalue distributions unlike the strum detector technique which considers only sample eigenvectors.
Finally, the PhilSea10 continuous receptions are useful for the validation of the RMT model predictions though they where few cases were violation of model predictions has occurred due to the following assumptions: The Strum is a multiple interferer case, but the RMT model was derived for a single interferer.
The strum components are not necessarily orthogonal. The Eigenvalues of the strum are approximately equal during the strong events.

6.2 Future Scope:

As an extension of this study, a further analysis is required for the failure of validation in few cases were relevant results where provided in a recent paper by Bloemendal et al [22]. This paper provides numerous results on the sample eigenvectors, eigenvalue locations, including predictions of cone concentration for multiple interferers (spikes). The following are few of them :
The sample eigenvectors of interferers that are close in power do not necessarily have a one-to-one relationship with the interferer replicas, even if the replicas are orthogonal.
The sample eigenvectors of the noise may be biased towards an interferer with power close to the noise.
For multiple close interferers, the cone is really a subspace spanning those interferers.
This paper suggests that notch depth analysis should be redefined to measure the DMR ABF notch components in that subspace. Rank can be estimated using a better eigenvalue based rank estimation technique for the cases where there are violations, may be by using Improved Whitening transform of DMR beamformer and other algorithms. Finally, using other metrics such as SINR loss of DMR beamformer [23] can be verified using the PhilSea10 receptions.

Bibliography

Bibliography

[1] J.Capon, "High-resolution frequency-wavenumber spectrum analysis," *Proc. IEEE*, vol. 57, pp. 1408–1418, August 1969.

[2] K. E. Wage and J. R. Buck, "Performance analysis of dominant mode rejection beamforming," *Proceedings of 20th International Congress on Acoustics*, August 2010.

[3] D. A. Abraham and N. L. Owsley, "Beamforming with dominant mode rejection," *Proc. IEEE OCEANS Conf.*, p. 470475, 1990.

[4] J. R. Buck and K. E. Wage, "A random matrix theory model for the dominant mode rejection beamformer notch depth," *Proc. IEEE Statistical Signal Process. Workshop*, pp. 824–827, August 2012.

[5] K. E. Wage and J. R. Buck, "Snapshot performance of the dominant mode rejection beamformer," *IEEE J. Oceanic Engineering*, vol. 39(2), pp. 212–225, April 2014.

[6] C. D. Richmond, "MVDR adaptive sidelobes: Extending ruzes formula and providing an exact calculation of the probability of sidelobe suppression."

[7] K. E. Wage, J. R. Buck, M. A. Dzieciuch, and P. F. Worcester, "Experimental validation of a random matrix theory model for dominant mode rejection beamformer notch depth," *Proc. IEEE Statistical Signal Process. Workshop*, pp. 820–823, August 2012.

[8] K. E. Wage and J. R. Buck, "SINR loss of the dominant mode rejection beamformer," *International Conference on Acoustics, Speech, and Signal Processing*, April 2015.

[9] R. J. Urick, *Principles of underwater sound.* McGraw-Hill Ryerson, 1983.

[10] V. E. Premus, S. M. Kogon, and J. Ward, "Beamspace adaptive beamforming for hydrodynamic towed array self-noise cancellation," *ASAP*, 2001.

[11] H.Cox, "Robust adaptive beamforming," *IEEE Trans. On Acoustics, Speech and Signal Processing*, pp. 1365–1376, october 1987.

[12] H. F. Yung P. Lee and W. W. Lee, "Subarray beam-space adaptive beamforming for a dynamic long towed-array," *ASAP*, 2004.

[13] H. L. V. Trees., *Optimum array processing.* New York, NY, USA: Wiley-Interscience, 2002.

[14] R. R. Nadakuditi and A. Edelmanl, "Sample eigenvalue based detection of high-dimensional signals in white noise using relatively few samples," *IEEE Trans. Signal Processing*, pp. 2625–2638, July 2008.

[15] D. Paul, "Asymptotics of sample eigenstructure for a large dimensional spiked covariance model."

[16] P. F. Worcester, M. A. Dzieciuch, J. A. Mercer, R. K. Andrew, B. D. Dushaw, A. B.Baggeroer, K. D. Heaney, G. L. DSpain, J. A. Colosi, R. A. Stephen, a. B. M. H. John N. Kemp, L. J. V. Uffelen, and K. E. Wage, "The north pacific acoustic laboratory deep-water acoustic propagation experiments in the philippine sea," *Journal of Acoustic society of America*, vol. 134(4), pp. 3360–3375, 2013.

[17] K. E. Wage, M. Farrokhrooz, M. A. Dzieciuch, and P. Worcester, "Analysis of the vertical structure of deep ocean noise using measurementsfrom the spicex and philsea experiments," *Proceedings of Meetings on Acoustics*, vol. 19, June 2013.

[18] Peter F Worcester, "NPAL 2010 : 2011 Philippine Sea Experiment PhilSea10 Mooring Recovery and Near-Seafloor DVLA Deployment Cruise Plan."

[19] Peter F. Worcester, "NPAL Philippine Sea Experiment: PhilSea10 SIO Experiment Plan."

[20] K. E. Wage, *Calibration of measurements made with NPAL recording systems during the SPICE and PhilSea experiments.* George Mason University, Fairfax, VA: Technical report, 2012.

[21] S. Kogan, "Robust adaptive beamforming for passive sonar using eigenvector/beam association and excision," *Proc. IEEE Sensor Array Multichannel Signal Process. Workshop*, pp. 33–37, August 2002.

[22] A. Bloemendal, A. Knowles, and H. Yau, "On the principal components of sample covariance matrices," *Probablity theory realtaed fields*, pp. 459–552, February 2016.

[23] J. A. Diaz-Santos and K. E. Wage, "An improved whitening transformation for snapshot deficient scenarios," *IEEE MTS*, pp. 1 – 6, August 2015.